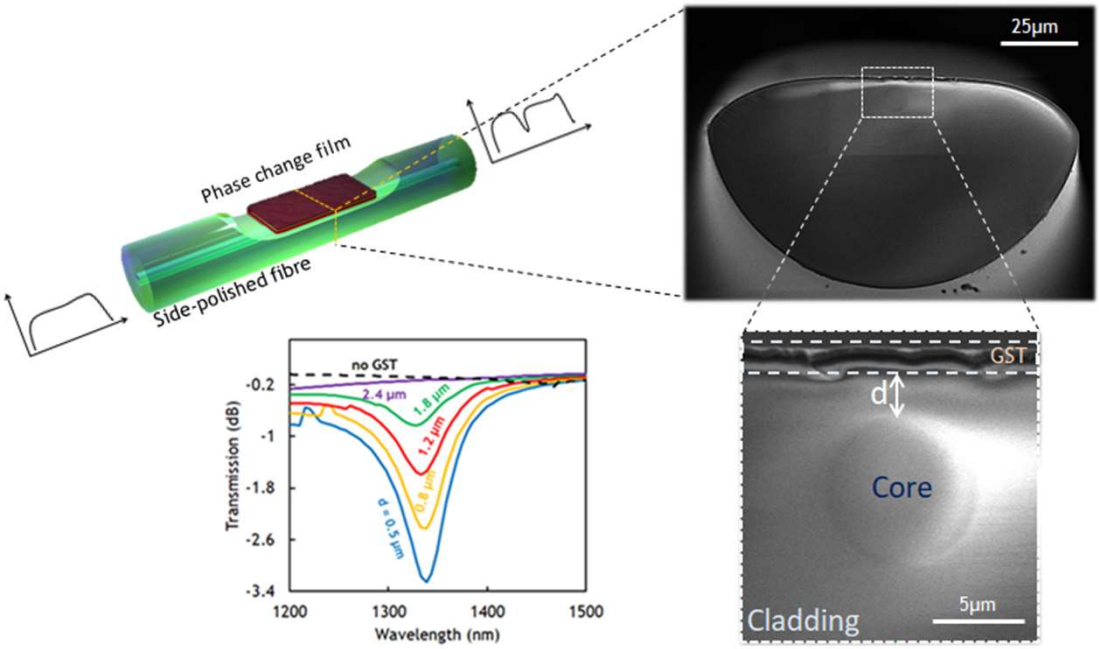


Fibre-integrated phase-change devices

Tiago Jorge Mendes Martins
PhD in Physics
Physics and Astronomy Department
2020

Supervisor
Orlando José Reis Frazão, Invited Assistant Professor, FCUP

Co-supervisor
Manuel Joaquim Bastos Marques, Auxiliar Professor, FCUP

Faculdade de Ciências da Universidade do Porto

Fibre-integrated phase-change devices

Tiago Jorge Mendes Martins

Thesis submitted to Faculdade de Ciências da Universidade do Porto in partial fulfillment of the requirements for the degree of Ph.D. in Physics

This thesis was conducted under the supervision of

Dr. Orlando José Reis Frazão

Invited Assistant Professor of Departamento de Física e Astronomia da Faculdade de Ciências da Universidade do Porto

Dr. Manuel Joaquim Bastos Marques

Auxiliar Professor of Departamento de Física e Astronomia da Faculdade de Ciências da Universidade do Porto

I am the eggman, they are the eggman,

I am the walrus, goo goo g´joob

John Winston Lennon

Acknowledgements

I would like to thank Orlando Frazão for his continuous support throughout this PhD project and for his valuable contributions, which helped improve the quality of this work. He played a major role in providing the inspiration for the main topic of this thesis and in making my visit to the ORC possible.

A word of appreciation goes to Prof. Manuel Marques for his constant willingness to clarify any doubts and for his keen eye for detail.

I could not but express my gratitude to Prof. Behrad Gholipour and Prof. Kevin MacDonald. Theirs was a truly vital contribution to this project, providing much need guidance in what was for me a new topic of scientific research.

I extend my gratitude to those who contributed directly to the output of this thesis, namely Prof. Nikolay Zheludev, Dr. Davide Piccinotti and Dr. Bruce Ou.

Special thanks is due to all the people in the Nanophotonics and Metamaterials group for welcoming me in their midst, making me feel like part of the team and helping me whenever I needed, either through technical/scientific advice or through their encouragement.

I would also like to thank INESC-TEC and the people in the Centre for Applied Photonics for all the support throughout the project.

I also acknowledge the MAP-fis doctoral programme and FCT for the financial support provided under the grant PD/BD/135008/2017.

Abstract

The central purpose of this project revolves around the integration of phase-change media into optical fibre networks: the aim is to combine the capacity of chalcogenide materials, namely Germanium Sulphide Tellurium (GST), to alternate between amorphous and crystalline states in a controlled and non-volatile fashion, with the well-established potential of fibre optic systems, giving rise to all-optical switching devices capable of controlling light intensity and phase. Such features could be of interest in the context of fibre-integrated memories, processing units and communication systems.

Two device architectures are proposed, both designed to provide switching functionality in optical fibre structures. One of the studies focuses on the combination of a thick GST film with a side-polished fibre, while the other investigates the performance of a nano-patterned GST film deposited on the end facet of an optical fibre tip. In both scenarios, resonant behaviour is induced, and its spectral profile can be dynamically tuned via switching the GST layer phase. The nature of these resonances is probed in order to better understand the underlying phenomena. Spectral adjustment of the resonances is also achieved by playing around with the geometry of these structures, supporting a wavelength coverage that spans the entire near-infrared range, of critical importance in telecommunications. In addition, the performance of polarisation-insensitive configurations based on GST discs is assessed, paving the way for future designs embedded in optical fibres which could render the switching operation more versatile. Patterning the active chalcogenide layer at the nanoscale, as successfully attempted in the fibre tip device and the polarisation-insensitive GST disc arrays, allows leveraging the potential of metamaterial properties, creating an enhanced performance in the context of phase-change fibre-integrated switching devices.

Resumo

O objectivo principal deste projecto centra-se na integração de materiais calcogénios em dispositivos de fibra óptica: o propósito é combinar a capacidade destes materiais, nomeadamente Germânio Antimónio Telúrio (GST), para alternar entre os estados amorfo e cristalino de uma forma controlada e não-volátil, com o potencial já estabelecido dos sistemas em fibra óptica, dando origem a dispositivos de *switching* capazes de controlar a intensidade e fase da luz guiada nestas estruturas. As características referidas têm relevância particular no contexto de memórias integradas em fibra óptica, unidades de processamento e sistemas de comunicação.

Duas arquitecturas são propostas, ambas desenvolvidas com o intuito de permitir o recurso a processos de *switching* em guias de fibra óptica. Um dos estudos foca-se na combinação de um filme de GST com uma fibra polida, enquanto o outro investiga o funcionamento de um filme de GST estruturado após deposição numa ponta de fibra. Em ambos os cenários, comportamento ressonante é induzido e o perfil espectral associado pode ser alterado dinamicamente com recurso à modificação da fase estrutural do filme de GST. A natureza destas ressonâncias é avaliada com o objectivo de melhor compreender os fenómenos por detrás da sua geração em configurações como as descritas anteriormente. A modificação do perfil espectral também pode ser alcançada através do ajuste da geometria das estruturas investigadas, permitindo uma cobertura de comprimentos de onda que se estende ao longo de toda a gama do infravermelho próximo, de importância crítica em telecomunicações. Para além disto, é feita a análise da performance de configurações tolerantes relativamente a estados de polarização distintos, baseadas em discos de GST. Assim será possível a criação de futuras estruturas em fibra óptica capazes de operações de *switching* mais versáteis. Estruturar a camada de material calcogénio permite utilizar o potencial das propriedades encontradas em metamateriais, conduzindo a um desempenho melhorado no âmbito de dispositivos de *switching* embebidos em fibras ópticas.

Contents

List of Figures x

List of Tables xvii

Nomenclature xviii

1. Introduction 1

1.1. Metamaterials 2

1.2. Dynamic control over the optical response of a metamaterial 6

1.3. Waveguide-integrated metamaterials and functional films 9

1.4. Objectives and structure of the thesis 12

Journal articles 13

Communications in international conferences 13

2. Tools and techniques 15

2.1. Focused ion beam milling 16

2.2. Sputtering 19

2.3. Thermal evaporation 21

2.4. Reactive ion etching 22

2.5. Polishing techniques 23

2.6. SEM 25

2.7. Thickness characterisation 26

2.8. Spectral characterisation 27

3. Chalcogenides 30

4. Fibre tip-integrated phase-change metasurfaces 37

4.1. Introduction 38

4.2. Simulations 39

4.2.1. Spectral tuning via adjustment of the geometrical parameters 40

4.2.2. Assessing spectral modifications arising from changes in the optical properties of the GST layer 44

4.3. Experimental results 54

4.3.1. GST blocks on flat glass substrates 54
4.3.2. Fibre-integrated metasurfaces based on arrays of GST blocks 58
4.4. Conclusion 65
5. Side-polished-fibre-integrated phase-change devices 66
5.1. Introduction 67
5.2. Simulations 68
5.3. Experiments 74
5.4. Patterned GST layer on a side-polished fibre 79
5.5. Conclusion 82
6. Phase change Huygens´ metasurfaces based on GST nanodiscs 83
6.1. Introduction 84
6.2. Simulations 86
6.3. Experiments 94
6.4. Conclusion 99
7. High Q-factor double-period gratings 100
7.1. Introduction 101
7.2. Simulations 102
7.3. Conclusion 110
9. Final Remarks 111
10. Appendices 115
11. References 122

List of Figures

Figure 1 - Reconfigurable metamaterials: (a) thermally-induced reconfiguration[85]; (b) light modulation via controllable (through delay line) short pulse interaction near the metamaterial[39]; (c) and (d) tuning of the metamaterial optical response via structural phase transitions in a chalcogenide layer[34,35]. 9

Figure 2 – (a) Structured fibre tip for amplification of the evanescent field of free electrons[90]; (b) gold metasurface on $LiNbO_3$ waveguides to control mode propagation[94]; (c) graphene-coated side-polished fibre for polarisation-dependent light modulation[96]; (d) GST-coated Si_3N_4 waveguide for non-volatile, multi-level integrated memory[104]; (e) graphene-coated microfibre[101]. 11

Figure 3 – (a) Schematic diagram featuring the main components of an FIB system[107]; (b) picture of an FIB workstation similar to the one used in this work[109] 17

Figure 4 – FIB-milled devices: (a) bow-tie-shaped aperture for imaging with enhanced resolution[112]; (b) bow-tie-shaped antenna for enhanced interaction with a single quantum dot[114]; (c) Fabry-Pérot cavity in optical fibre micro-tips for sensing[118]; (d) super-oscillatory lens for subwavelength imaging[122]. 18

Figure 5 – (a) Schematic diagram of a typical RF sputtering system; (b) photograph of the utilised model of sputtering machine[125]. 19

Figure 6 – (a) Craic microspectrophotometer[138]; (b) OSA[139]. 28

Figure 7 – Schematic diagram of the experimental setup for measurement of the reflection characteristics of fibre-integrated devices. 29

Figure 8 – Real part of the refractive index (n) and extinction coefficient (k) spectra for three different PCMS (GeTe, $Ge_2Sb_2Te_5$ and $GeSb_2Te_4$) and two ordinary covalent semiconducting materials, $AgInTe_2$ and InSb, in the amorphous (a, b) and crystalline (c, d) phases. Grey lines in c and d show results in the amorphous state for swifter comparison with those in the crystalline phase (adapted from [134]). 32

Figure 9 – (a) Crystalline structure of GST; (b) changes in optical properties (n and κ) as Ge content varies. (adapted from [2]). 34

Figure 10 – (a) Super-oscillatory lens etched into a GST film using a femtosecond laser[152]; (b) corresponding hotspot; (c) schematic diagram of a GST film integrated into a waveguide[104]. .. 36

Figure 11– (a) Dispersion curves for the refractive index (n) and the extinction coefficient (κ) of GST in the amorphous (blue) and crystalline (red) phases; (b) 2D schematic diagram showing the COMSOL-modelled geometry, materials and configuration of the interaction between light and metamaterial structure; periodic input and output ports are considered, along with periodic boundary conditions; (c) 3D schematic representation of the periodic GST block array; 40

Figure 12 – Simulated (a) transmission, reflection and (b) transmission, absorption spectra for three different periods (900, 950, 1000 nm); (c)-(e) corresponding field maps displaying the norm of the electric field at resonance; w = 80 nm, t = 190 nm..... 41
Figure 13 - Field maps displaying (a) the norm, (b) z-component and (c) x-component of the electric field; (d) profile showing the norm of the magnetic field; All field maps are taken at resonance; P = 900 nm, w = 80 nm, t = 190 nm..... 42
Figure 14 - Simulated (a) transmission, reflection and (b) transmission, absorption spectra for four different gap widths (70, 80, 90, 100 nm); (c)-(f) corresponding field maps displaying the norm of the electric field at resonance; P = 900 nm, t = 190 nm. Arrows show how the resonances shift as a result of widening the gaps. 43
Figure 15 - Simulated (a) transmission, reflection and (b) transmission, absorption spectra for four different film thicknesses (190, 200, 210, 220 nm); (c)-(f) corresponding field maps displaying the norm of the electric field at resonance; P = 900 nm, w = 80 nm. Arrows show how the resonances shift as a result of simulating thinner GST films. 44
Figure 16 – Simulated (a) transmission, reflection spectra for five different values of the refractive index n (3.5, 3.6, 3.8, 3.9, 4.0) in the case of a non-dispersive dielectric material with extinction coefficient κ = 0.01; red line shows transmission for dispersive amorphous GST for comparison with a non-dispersive dielectric material (κ = 0.01) with n = 3.5; (b) resonant wavelength and Q-factor as a function of RI; (c)-(g) corresponding field maps displaying the norm of the electric field at resonance; arrow shows how the resonances shift as a result of increasing n; P = 900 nm, w = 80 nm, t = 190 nm. 45
Figure 17 – Simulated (a) transmission, reflection and (b) transmission, absorption spectra for five different values of the extinction coefficient κ (0.01, 0.1, 0.2, 0.3, 0.4) in the case of a non-dispersive dielectric material with refractive index n = 4.0; red line shows transmission for a non-dispersive dielectric material with κ = 0.4 and n = 4.0 (akin to a relatively well crystallised GST film); (c)-(g) corresponding field maps displaying the norm of the electric field at resonance; arrows show how the resonance evolves as a result of increasing n; P = 900 nm; w = 80 nm, t = 190 nm. 46
Figure 18 - Dispersion spectra of the refractive index n and extinction coefficient κ for the amorphous phase and different degrees of crystallisation (10%, 20% and 30%). 47
Figure 19 - Simulated (a) transmission, reflection and (b) transmission, absorption spectra for the amorphous phase and different degrees of crystallisation (10%, 20% and 30%); red curve shows transmission for a non-dispersive dielectric material with n = 4.2 and κ = 0.4; P = 900 nm, w = 80 nm, t = 190 nm. 48
Figure 20 – (a) Simulated phase and group delay dispersion (GDD) for three different periods (900, 950, 1000 nm); (b) corresponding transmission curves; w = 80 nm, t = 190 nm. 50

Figure 21 – Simulated phase and group delay dispersion (GDD) for both amorphous (black) and crystalline (red) states; P = 900 nm, w = 80 nm, t = 190 nm..... 51
Figure 22 - Simulated phase and group delay dispersion (GDD) for the amorphous state and different degrees of crystallisation (10%, 20%, 30%); P = 900 nm, w = 80 nm, t = 190 nm. 51
Figure 23 - Graphical comparison between (a) phase and (b) group delay dispersion (GDD) derived using Kramers-Kronig or COMSOL for both structural states; P = 900 nm, w = 80 nm, t = 190 nm. 54
Figure 24 - (a) SEM picture of an array with period 1000 nm; (b) optical microscope picture of all the arrays (transmission) after crystallisation using a CW laser: dark areas (low transmission) correspond to crystallised areas whereas brighter areas (higher transmission) correspond to amorphous GST. 55
Figure 25 - CRAIC-measured (a) transmission, reflection and (b) absorption spectra for different array periods: 900, 1000 and 1100 nm; w = 80 nm, t = 200 nm..... 56
Figure 26 - Craic-measured transmission and reflection spectra for the amorphous and crystalline phases. Arrows show how the fringes shift as a result of crystallisation; P = 1000 nm, w = 80 nm, t = 200 nm. 57
Figure 27 - (a) Craic-measured transmission and reflection spectra for the amorphous and crystalline phases; arrows show how the fringes shift as a result of crystallisation; (b) corresponding transmission and reflection ratios; P = 900 nm, w = 80 nm, t = 200 nm..... 57
Figure 28 - (a) Craic-measured transmission and reflection spectra for the amorphous and crystalline phases; arrows show how the fringes shift as a result of crystallisation; (b) corresponding transmission and reflection ratios; P = 1100 nm, *w* = 80 nm, t = 200 nm..... 58
Figure 29 - (a) Schematic diagram of the proposed optical switch based on a GST phase change film deposited on an optical fibre tip; (b) SEM picture of the device; inset: close-up showing the structured area around the core in detail. 59
Figure 30 – (a) Simulated and (b) experimentally measured transmission spectra for arrays of GST cubes with w = 80 nm, t = 190 nm and P taking three different values: 900, 950 and 1000 nm..... 60
Figure 31 – Experimentally measured (a) transmission, (b) reflection and (c) absorption spectra for arrays of GST cubes with w = 80 nm, t = 190 nm and P taking three different values: 900, 950 and 1000 nm. 61
Figure 32 – Schematic diagram showing the in-fibre crystallisation setup using CW laser radiation..... 62
Figure 33 – (a) Simulated and (b) experimentally measured transmission spectra in the amorphous and crystalline states; P = 900 nm, w = 80 nm, t = 190 nm..... 63
Figure 34 – Field maps displaying the norm of the electric and magnetic fields in the amorphous and crystalline phases. P = 900 nm, w = 80 nm, t = 190 nm. 63

Figure 35 – Simulated and experimentally measured transmission ratios between amorphous and crystalline phases. 64
Figure 36 - (a) Pictorial representation of the mode profile as it propagates along the GST-covered side-polished fibre; (b) 2D schematic drawing of the cross-section profile of our structure; l – GST film length; t – GST film thickness; d – core-to-plane distance..... 69
Figure 37 – Detail of the Lumerical MODE simulation environment, showing the three-section geometry of the modelled structure: I – unpolished input fibre; II – polished section; III – unpolished output fibre. Green and red dotted lines identify the input and output ports, respectively. 69
Figure 38 - (a) Simulated transmission spectra for different core-to-plane distances d (t = 500 nm, l = 160 μm); (b)-(e) corresponding simulated field profiles, taken at resonance (white lines indicate the GST layer). 70
Figure 39 - (a) Electric field map at resonance when d = 0.5 μm and t = 500 nm; zoomed-in pictures of the cladding area above the core when t = 500 nm and (b) d = 0.5 μm or (c) d = 2.4 μm; detail of the cladding area of interest (d) in the case of a bare side-polished fibre and when (e) t = 500 nm and d = 0.5 μm. 71
Figure 40 - (a) Modulation depth and (b) Q-factor as functions of the core-to-plane distance (t = 500 nm, l = 160 μm). 71
Figure 41 - (a) Simulated transmission spectra for different GST film thicknesses (d = 500 nm, l = 160 μm); insets: resonant wavelength as a function of t, field map when t = 620 nm; (b)-(e) corresponding simulated field profiles, taken at resonance (white lines indicate the GST layer). 73
Figure 42 - (a) Transmission modulation depth and (b) Q-factor as functions of GST film thickness; (d = 0.5 μm, l = 160 μm). 73
Figure 43 - SEM pictures of the side-polished surface (a) before and (b) after reactive ion etching; (c) SEM picture of a GST-coated side-polished fibre (GST deposited after the etching run). 75
Figure 44 – (a) 3D schematic diagram of the device; (b)-(e) SEM pictures of the device and its cross-section profile. Both tested devices are shown (core-to-plane distances are displayed). .. 76
Figure 45 – Measured transmission spectra of (a) the tested bare side-polished fibres and of a normal singlemode fibre, as well as of (b) the GST-coated side-polished fibres (normalised relative to the respective bare side-polished fibre transmission spectrum); t = 500 nm, l = 5 mm; Dark and light blue curves correspond to different core-to-plane distances. 77
Figure 46 – (a) Experimental and (b) simulated transmission spectra of a side-polished fibre coated with amorphous (black) and crystalline (red) GST (t = 500 nm, d = 0.5 μm) along with the measured contrast ratio between transmission in the amorphous and crystalline phases (dashed grey line); field maps at resonance for a side-polished fibre coated with (a) amorphous

and (b) crystalline GST (t = 500 nm; d = 0.5 μm; amorphous @ 1338 nm; crystalline @ 1708 nm). 78

Figure 47 - Change in the strength and spatial distribution of field between the two phase states of the GST layer, evaluated as the difference between panels (c) (d) in Figure 46. 79

Figure 48 – (a) SEM picture of a 240-μm-long grating etched on the 300-nm GST layer deposited on a side-polished fibre; (b) close-up of the transition region between three 30-μm stitched gratings (white dashed lines identify the fibre core; (c) cross-section profile of the structured GST film..... 80

Figure 49 – Transmission of a side-polished fibre covered with an unstructured GST film and after fabrication of a grating, of increasing length, milled through that same GST layer (normalised relative to the bare side-polished fibre; each curve is offset by 6 dB). 81

Figure 50 - (a) 3D schematic representation of the periodic GST disc array; (b) 2D schematic diagram showing the Lumerical-modelled geometry, materials and configuration of the interaction between light and metamaterial structure; (I) Periodic boundary conditions; (II) reflection monitor..... 86

Figure 51 - (a) Reflection spectrum of arrays of discs, made out of amorphous GST, with varying diameter D; (b)-(i) corresponding electric and magnetic field maps at resonance (MD); Inset: electric and magnetic field maps corresponding to the ED, for D = 800 nm; w = 200 nm, t = 220 nm. 87

Figure 52 - (a) Reflection spectra of arrays of discs made out of a non-dispersive dielectric material with varying RI and κ = 0.0 (each curve is offset by 200; blue and red dashed lines serve as visual aids to isolate the two dipole modes); overlapping (b) ED and (c) MD resonances; Inset: Q-factor as a function of RI; (d)-(o) corresponding electric and magnetic field maps at resonance, for both the electric (ED) and magnetic dipoles (MD) (dashed lines identify the GST disc); w = 200 nm, t = 220 nm..... 89

Figure 53 - (a) Reflection spectrum of arrays of discs with varying D, made out of a non-dispersive dielectric material with RI = 5.0 and κ = 0.0 (each curve is offset by 200; blue and red dashed lines serve as visual aids to isolate the two dipole modes); (b)-(o) corresponding electric and magnetic field maps at resonance, for both the electric (ED) and magnetic dipoles (MD) (white dashed lines identify the GST disc); dotted arrows identify the ED mode; w = 200 nm, t = 220 nm..... 90

Figure 54 - Reflection spectra of arrays of nanodiscs made out of a non-dispersive dielectric material with varying κ and (a) D = 800 nm, w = 200 nm, t = 220 nm, RI = 3.5 as well as (b) D = 550 nm, w = 200 nm, t = 220 nm, RI = 5.0; (c), (d) corresponding electric and magnetic field spatial profiles for both ED and MD for varying extinction coefficient. 92

Figure 55 - (a) Reflection spectra of arrays of nanodiscs, made out of a non-dispersive dielectric material with RI = 3.5 and κ = 0.0, with varying t (from 200 nm to 230 nm); (b)-(e) corresponding electric field spatial profiles for both ED and MD; D = 800 nm, w = 200 nm.... 93
Figure 56 - (a) Reflection spectra of arrays of nanodiscs, made out of a non-dispersive dielectric material with RI = 3.5 and κ = 0.0, with varying w (from 190 nm to 220 nm); (b)-(e) corresponding electric field spatial profiles for both ED and MD; D = 800 nm, t = 220 nm. 93
Figure 57 – (a) Reflection and (b) transmission spectra of arrays of GST nanodiscs with D = 550 nm, 670 nm, 800 nm, 950 nm, for two orthogonal polarisation states; SEM picture of an array of nanodiscs with D = 950 nm; w = 200 nm, t = 220 nm. 95
Figure 58 - Optical microscope pictures of an array of GST discs with D = 950 nm, w = 200 nm, t = 220 nm, in the (a) amorphous and (b) crystalline states. 96
Figure 59 - (a) Reflection and (b) transmission spectra of arrays of GST nanodiscs with D = 550 nm, 670 nm, 800 nm, 950 nm, for two structural phases; Arrows illustrate how the resonances shift upon crystallisation; w = 200 nm, t = 220 nm. 96
Figure 60 - (a) Simulated and (b) experimentally measured reflection spectra of an array of GST nanodiscs with D = 550 nm, w = 200 nm, t = 220 nm, for two structural phases; (c)-(f) filed maps showing both electric and magnetic field norm in the amorphous and crystalline phases, at resonance (MD). 97
Figure 61 - (a) Reflection and (b) transmission modulation spectra of arrays of GST nanodiscs with D = 550 nm, 670 nm, 800 nm, 950 nm; w = 200 nm, t = 220 nm..... 98
Figure 62 - 2D schematic diagram showing the COMSOL-modelled geometry, materials and configuration of the interaction between light and metamaterial structure; periodic input and output ports are considered, along with periodic boundary conditions..... 102
Figure 63 - Transmission spectra for different α; dashed black line shows transmission in a symmetric grating structure; arrows illustrate how the fringes shift when α increases; t = 300 nm, w = 140 nm. 103
Figure 64 - Ez field maps for α = 0.21; dashed circular lines and arrows identify the current density flow; t = 300 nm, w = 140 nm. 104
Figure 65 - (a) Reflection and (b) absorption spectra for different α; dashed black lines show reflection and absorption in a symmetric grating structure; arrows illustrate how the fringes shift when α increases; t = 300 nm, w = 140 nm..... 104
Figure 66 - Transmission spectra for different α when (a) t = 270 nm and (b) = 250 nm; dashed black lines show transmission in a symmetric grating structure; arrows illustrate how the fringes shift when α increases; w = 140 nm. 105
Figure 67 - Q-factor as a function of the asymmetry α for GST films with different thickness (250 nm, 270 nm, 300 nm); inset: transmission in the case of α = 0.21, t = 300 nm, w =140 nm. 107

Figure 68 - Transmission spectra as the gap width *w* changes; dashed black line shows transmission in a symmetric grating structure; α = 0.15, t = 250 nm. 107
Figure 69 – (a) Phase and (b) transmission spectra as α changes; black dashed lines show phase and transmission in a symmetric grating structure; blue dashed line shows phase in air; arrows illustrate how the fringes shift when α increases; t = 300 nm, w = 140 nm. 108
Figure 70 - Dispersion profiles (orange) for the (a) low-Q and (b) high-Q resonances; transmission (black) is also displayed; α = 0.21, t = 300 nm, w = 140 nm. 109

List of Tables

Table 1 – Technologically appealing properties of PCMs (adapted from [2]). 35
Table 2 - Spectral location of both low- and high-Q resonances for different GST film thickness; α = 0.21, w = 140 nm. 105

Nomenclature

RI – Refractive Index

ε – Electric Permittivity

μ – Magnetic Susceptibility

ENZ – Epsilon Near Zero

EIT – Electromagnetically-induced transparency

SRR – Split Ring Resonator

CNT – Carbon Nanotube

GST – Germanium Antimony Telluride

FIB – Focused Ion Beam

PVD – Physical Vapour Deposition

RIE – Reactive Ion Etching

SEM – Scanning Electron Microscopy

OSA – Optical Spectrum Analyser

PCM – Phase-change Material

GLS – Gallium Lanthanum Sulphide

n – Refrative Index

κ – Extinction Coefficient

DSC – Differential Scanning Calorimetry

GDD – Group Delay Dispersion

GVD – Group Velocity Dispersion

SMF – Singlemode Fiber

IR – infrared

T_g – Glass Transition Temperature

T_c – Crystallisation Temperature

T_m – Melting Temperature

DC – Direct Current

CW – Continuous Wave

1. Introduction

1.1. Metamaterials

Metamaterials constitute an attempt to go beyond the electromagnetic properties found in conventional materials, such as those readily available in nature[1]. The same way these conventional materials have basic constituents such as atoms, so do metamaterials possess fundamental building blocks, usually designated metamolecules. By changing the configuration of these building blocks, it is possible to rearrange the core architecture of the metamaterial and control its physical properties. If this reconfiguration is based on moving from one well-defined structural state to another, phase-change switching is achieved[2]. The upside of this approach is linked to the fact that structural phase transitions can be induced by optical pulses, allowing light-by-light control to be implemented, eliminating the need to realise mechanically-activated reconfiguration, which is significantly slower[3].

Metamaterial reconfigurability has been the focus of a great deal of research efforts over the past decades, following the initial research frenzy revolving around the investigation of novel optical properties, such as negative refractive index[4-9], extraordinary metamaterial-assisted chirality and polarisation control[10-15], near-perfect absorption[16-23] and classically induced transparency[24-27]. A comprehensive set of metamaterial geometries and constitutive materials, as well as a number of strategies to modulate the metamaterial optical response, have been explored in order to grab a hold of the aforementioned optical properties and extend their band of operation from the microwave to the visible range. In the specific case of switching, one of the major goals is to achieve fast responses. The most promising method relies on optical modulation using light pulses. This can be implemented through photoexcitation of carriers[10,28-32], via light-induced structural phase transitions in materials embedded into the overall metamaterial structure[33-36] or simply by controlling the interaction between two counter-propagating pulses at the position where the metamaterial is located[37-42]. The speed of the metamaterial response will depend on the characteristic time scale of these processes.

From the extraordinary physical properties associated with metamaterials, the first to be considered was negative refraction, initially studied by Veselago[4] in the 60s. The approach was completely theoretical and developed without the prospect of immediate experimental implementation. Several interesting conclusions arise from a simple conjecture based on considering simultaneously negative electric permittivity ε and magnetic susceptibility μ. In this

instance, Snell´s law of refraction needs to be rewritten, yielding a relation between incidence θ_1 and refraction θ_2 angles that depends on the handedness of the involved media, as in

$$\frac{sin\theta_1}{sin\theta_2} = \frac{p_2}{p_1}\sqrt{\frac{\varepsilon_2\mu_2}{\varepsilon_1\mu_1}}, \quad (1)$$

where p is the handedness of the medium (either equal to 1 or -1, depending on whether a left- or right-handed medium is under consideration) and the subscripts 1 and 2 identify the two media. It becomes apparent that when the media have different p, incidence and refraction angles have opposite signs. This highlights the possible use of left-handed media to focus light, even beyond the diffraction limit[7]. Besides this exciting result, reversed Doppler and Vavilov-Cerenkov effects along with light pressure being replaced with light attraction are reported[4].

Pendry started from Veselago´s ideas in order to propose a perfect lens crafted from a system with negative refractive index (RI)[7]. Besides the focusing capabilities of such system, it is also shown that it amplifies evanescent waves, meaning "both propagating and evanescent waves contribute to the resolution of the image"[7].

The enticing prospects linked to the physics of metamaterials, of which Veselago´s and Pendry´s contributions are some of the earlier major exponents, propelled a number of experimental attempts aimed at realising these novel properties[8,9,43], most of them based on tailoring ε and μ through the employment of periodically arranged structures, generating strong resonant behaviour in the microwave range. The tunability of metamaterial resonances, anchored in the resonant wavelength dependence on the size of the metamolecule, allows covering other relevant frequency bands. More sophisticated fabrication tools, making the creation of nanometre-scale structures possible, enables operation in the near-infrared and visible parts of the spectrum.

From the variety of novel and extraordinary optical responses found in metamaterials, chirality[10-15], perfect absorption[16-23], classically induced transparency[24-27] and epsilon-near-zero[44-54] (ENZ) behaviour are worth highlighting.

Since Pendry exploited chirality as a means to arrive at negative refraction[15], efforts have been guided towards the development of polarisers based on metamaterial devices. Rosette-like 4-fold unit cells constituted one of the earliest proposed designs[13,14]. The final light polarisation state can be seen as the result of the interaction between the magnetic and electric fields of the incoming electromagnetic wave and the magnetic and electric responses of the metamaterial. In fact, the most dramatic changes in the polarisation state are introduced at frequencies around the resonances exhibited by the metamaterial. These devices display negative refraction and unusual rotary powers, several orders of magnitude higher than those of traditional optically active crystals[10,11,14]. Photoinduced handedness switching has also been described[10].

The absorption A of a metamaterial can be obtained knowing the reflection R and the transmission T of a given material as in $A(\omega) = 1 - [R(\omega) + T(\omega)]$. It becomes clear that a structure with transmission and reflection resonances will also exhibit a resonant behaviour in absorption. The controllable spectral position of these features helps design good absorbers for a wide range of frequency values, from microwave[16,17,23] to visible[19,21], going through the infra-red[18,20,22].

Electromagnetically-induced transparency (EIT), achievable in metamaterials via purely classical phenomena[24-27], was first studied in quantum systems[55]. One of the strategies to implement a classical analogue to this process relied on a few layers of a fishnet metamaterial[25]. A single layer of the fishnet pattern yields a single resonance in the microwave range. When a second layer is included, a transmission window pops up in the middle of this resonance, in what constitutes spectral behaviour very similar to atomic EIT. This is achieved owing to the fact that consecutive fishnet patterns are π-shifted, resulting in out-of-phase induced currents. Basically, one of the layers acts as a bright mode (highly radiative with low Q-factor) and the other one as a dark mode (sub-radiant with high Q-factor). Interaction between these modes leads to quenched absorption and the appearance of a transmission window. A very interesting picture describing this classical analogue of quantum EIT has been provided[26]. Two split-ring resonators (SRR), a single and a double-gap resonator, the bright and dark modes, respectively, are considered. The configuration is modelled by a system of coupled masses on strings driven by an external force (the incident electromagnetic field). The oscillation of these masses is dampened to simulate the actual losses of the two modes. To remain coherent with the actual metamaterial system, one of the masses is more strongly dampened (bright mode). The equivalent electric circuit actually exhibits a spectral response for the delivered power that resembles an EIT-like spectrum. It has been routinely shown that these systems allow very high group refractive indices to be attained, bearing as a consequence significant reductions of light speed as it travels through these media[24,26,27].

Structures with near-zero parameters, which include media with near-zero relative permittivity and/or relative permeability and thus near-zero refractive index, exhibit a number of unique features, such as the decoupling of spatial and temporal field variations[53]. This last statement, with ample scientific and technological implications, reduced to its core, essentially means light propagating along a medium with near-zero refractive index will have its wavelength "stretched" (recall $\lambda_{medium} = \lambda_0/n$, where λ_{medium} is the wavelength in a particular medium, λ_0 the vaccum wavelength and n the refractive index of that medium) while its frequency remains the same. Under these circumstances, the electromagnetic field phase distribution will be nearly constant. The early output in this field, dating back thirteen years, focused on the possible "squeezing" of light through subwavelength channels[44,46]. Tailoring the radiation phase pattern, by forcing its conformity to the near-zero medium outline, has also been

theoretically investigated[45]. Experimental application of these principles followed suit[47-52,54]. Besides demonstrating light "squeezing" through very small channels, research in this area also revealed these systems can boost optical nonlinearities[49]. Again, the response of these metamaterials stretches from the microwave range[47] down to the near-infrared[51,52] and visible[50] bands.

Hyperbolic metamaterials have also drawn some attention[56,57]. Realisation of these metastructures can be achieved by restricting free-electron motion in one direction. From an experimental perspective, this can be easily attained by fabricating stacked layers of thin films (electronic motion confined to the in-plane directions). These structures are typically characterised by a tensorial permittivity, exhibiting distinct values for in-plane and out-of-plane directions. The hyperbolic regime is obtained when either the in-plane or the out-of-plane permittivity is negative. Cerenkov emission at very low electron energies in a hyperbolic medium is one of the possible experimental outcomes[56].

Metamaterials incorporating topological insulators have also featured among the most promising systems explored for light modulation[58,59]. These materials behave as an insulator in its bulk form but retain conducting states in its surface[60]. These are symmetry-protected surface conducting states[61].

Tuning the spectral profile and maximum amplitude of near-field optical forces between a metamaterial structure and a dielectric or metallic surface placed within close proximity from each other is possible by adjusting the metamaterial geometry, but also by adapting the distance between slabs or the optical parameters of the unstructured dielectric or metallic surfaces, such as the refractive index[62-65]. The near-field optical force generated in this context will depend on the optical response of the metamaterial, namely its ability to trap light, i.e. its absorption. Resonant absorption behaviour will inevitably lead to spectrally-selective performance. The near-field nature of the interaction is demonstrated by noting the optical force amplitude goes down exponentially with an increase of the distance between interacting slabs[62]. Replacing plasmonic materials with dielectric ones leads to enhancement of optical near-field forces, owing to reduced Joule losses[64,65].

Choosing materials with specific properties can help improve the performance of metamaterials, from superconductors[66-69] to carbon allotropes[70-76], without forgetting liquid crystals[77].

The use of superconducting materials means that, operating below the superconducting transition temperature T_C, Joule losses can be effectively suppressed owing to the strong increase in conductivity, resulting in high resonance Q-factors.

Carbon allotropes show encouraging optical properties that can be even more exciting when put together with metamaterial structures. Work with carbon nanotubes[70] and graphene[71-76] has been carried out. Carbon nanotubes (CNTs) are seen as coming close to the concept of a 1D system, as they present very small diameter-to-length ratios. When the metamaterial is functionalised with CNTs, the absorption spectral line clearly rises and both transmission and reflection decrease. The Q-factor of the metamaterial resonance suffers due to damping introduced by the CNTs. Transmission modulation when employing a CNT-functionalised metamaterial is proven more efficient than in the case in which CNTs stand alone.

Graphene plasmonics is a very enticing topic in scientific research, owing to the particular characteristics of plasmonic behaviour in this medium: very well confined, yielding high light enhancement factors, and with a lifetime much longer than that of plasmons in metals and semiconductors[78]. Several attempts at combining graphene layers with resonator arrays have been successfully accomplished[71-76]. Deposition of a graphene layer on top of the metamaterial ensemble entails quite appreciable transmission variations. This modulation can be controlled through electrical gating[72,73,75,76].

1.2. Dynamic control over the optical response of a metamaterial

The exploration of novel physical properties in metamaterials has proven to be a very fruitful area of research. More recently, the investigation of strategies to dynamically control these properties has gained relevance. One possible reconfiguration mechanism relies on geometrically rearranging the metamolecule, making good use of the knowledge that metamaterial resonances exhibit sensitivity to changes in the geometric parameters of the unit cell.

Actuators can be used to displace a movable part of the unit cell[79-81]. The idea is well illustrated in the specific case of a SRR[80]. As the movable part slides away, the initially closed square splits and the gap widens until the mobile side of the resonator actually touches back-to-back on a neighbouring unit cell. The induced currents can have significantly different behaviours depending on the unit cell configuration, meaning the optical response of the metamaterial can be modified using this method.

Structural tunability has been shown possible through the application of mechanical stress[82,83]. Besides the obvious impact on the unit cell size, stretching or compressing the device can actually help tune the gap width between the arms of the split ring resonator and possibly achieve field confinement and enhanced resonant behaviour[83].

Mechanical reconfiguration can be accomplished through controlled temperature variations[84,85]. The idea is to come up with metamaterials combining layers of materials with different thermal expansion coefficient, causing devices designed this way to experience pronounced bending. One example illustrating the efforts to implement this strategy consists in designing an array of SRRs in which each resonator is connected to the main frame supporting the metamaterial through cantilevers[84]. These cantilevers bend as temperature increases, changing the unit cell orientation relative to the propagation direction of the incoming electromagnetic field (Figure 1a). As a consequence, resonances can be spectrally shifted and strengthened/weakened.

Applied external fields, more precisely the Lorentz force associated to the external magnetic field and to induced currents flowing through the metadevice, can also drive the reconfiguration of the unit cell geometry[86,87].

Recent metamaterial-based devices are usually quite thin (thickness below the radiation wavelength) as they are typically fashioned from stacked thin films. The interaction between two propagating beams as they meet at the location where the metamaterial is can be controlled by adjusting the phase delay between them[37-42].

The metamaterial can be located at a node or an antinode of the interference pattern resulting from interaction between two counter-propagating beams[37]. The first case corresponds to allowed transmission for both beams, while the latter corresponds to suppressed transmission. Alternation between these two states can be achieved by introducing a delay line in the propagation path of one of the beams, shifting from node to antinode at the position where the metamaterial is. The switching ratio is established between the transmission levels of both states. It is shown that the modulation depth in this particular case is considerably enhanced when moving from an unstructured gold film to a patterned one, making good use of its resonant absorption profile. The extent to which light polarisation[40] and refraction[41] can be controlled also depends on the phase difference between propagating beams.

Switching based on interaction between two short light pulses near the metamaterial slab can be pursued[39] (Figure 1b). In the proposed configuration, the metamaterial is placed in the middle of the propagation path of both beams. When the time delay between the counter-propagating pulses is long, then they interact with the metamaterial independently and the modulation contrast is quite small (both experience normal levels of absorption, as obtained when only one pulse interacts with the metamaterial). However, when the time delay is short, the pulses can be made to overlap at the location where the metamaterial is. Under this condition coherently enhanced absorption (low transmission) is registered. The modulation ratio

between these two states (short and long time delay) is maximised for wavelengths near the metamaterial resonance (high absorption).

Specific unit cell designs yield characteristic and peculiar resonant responses. In the case of an SRR, the gap region resembles a capacitor and the resonance spectral position ends up being a function of the associated capacitance and inductance[31]. This means the resonant feature can be shifted by altering the capacitance in the gap region, which can be attained by inducing variations of the conductivity σ of the structure[10,28-32]. A broader application of this concept, whereby the capacitance of a multitude of unit cell designs can be adjusted by modulating σ of the constitutive material, ensures the suitability of this particular reconfiguration mechanism in a variety of different contexts. Excitation of charge carriers in semiconductor layers is a means of controlling σ, performed either through the application of a gate bias voltage[28] or through photoexciation of carriers by shining ultrashort pulses onto the metamaterial[10,29-32].

Physical properties of materials are sensitive to variations of external parameters such as temperature. This happens dramatically near the phase-transition temperature: taken over that temperature threshold, the system enters a new regime in which it exhibits a fundamentally different behaviour. The example of superconductivity serves to illustrate the point: below the critical temperature the resistance drops to values very close to zero, much smaller than those obtained just above this transition temperature[88]. Phase transitions provide good prospects in switching strategies, given the presence of two well-defined and distinct states[33-36].

Vanadium oxide (VO_2) experiences a light-induced phase transition between insulator and metal regimes characterised by substantially different conductivities[33]. Near this phase transition the permittivity is divergent and the properties of this dielectric layer, located just under an array of metallic SRRs, can be altered by varying its temperature, allowing modulation of the optical response of the whole structure.

Chalcogenide glasses, such as gallium lanthanum sulphide[36] (GLS) and germanium antimony telluride[34] (GST), have also been used in metamaterial switches. The photo-induced transition between amorphous and crystalline states of these two chalcogenide materials, combined with arrays of metallic SRRs, is explored for light modulation as these two phases present distinct physical properties (Figure 1c). The success of this combination involving phase-change materials and patterned metallic layers exhibiting strong resonances rests on the fact that such resonances are quite sensitive to changes in the surrounding dielectric environment, allowing modulation of the properties of the chalcogenide film to produce remarkable variations in the optical response of the overall device.

All-dielectric switches have been pursued as a path to reduce Ohmic losses associated with plasmonic structures[35,89]. The first device of this kind, based on a chalcogenide material,

relies on a GST nanograting with subwavelength pitch[35] (Figure 1d). The light-induced amorphous to crystalline conversion clears the way for attaining a substantially different optical response, characterised by red-shifted resonances and broadened spectral lines. These changes are attributed to increased real and imaginary parts of the RI of GST as it transitions from the amorphous to the crystalline states.

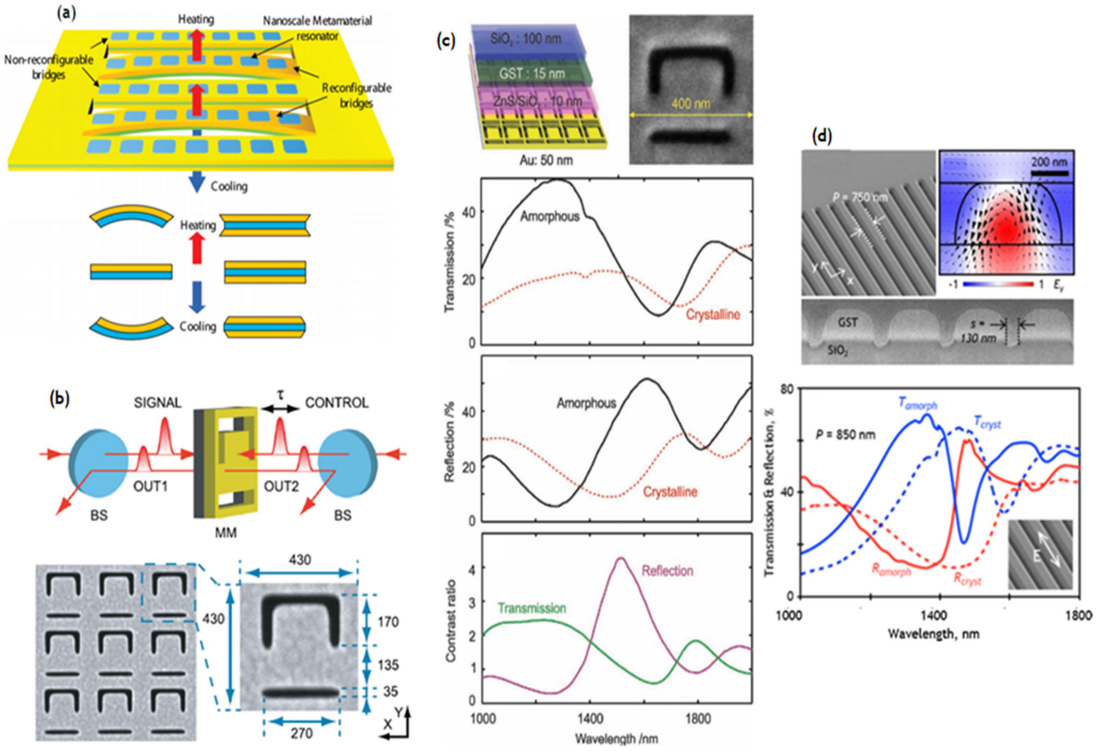


Figure 1 - Reconfigurable metamaterials: (a) thermally-induced reconfiguration[85]; (b) light modulation via controllable (through delay line) short pulse interaction near the metamaterial[39]; (c) and (d) tuning of the metamaterial optical response via structural phase transitions in a chalcogenide layer[34,35].

1.3. Waveguide-integrated metamaterials and functional films

Bringing together nanostructured thin film surfaces and optical fibres has already been successfully attempted[90-93]. FIB-milled nanogratings on metallised fibre tips allow enhanced interaction between these structures and the evanescent field of an electron-beam via added momentum, proportional to the inverse of the nanograting pitch, making it easier for radiation associated to this evanescent field to couple to modes guided along the fibre[90]. An all-dielectric sub-wavelength grating is fabricated on a fibre tip covered with an Si layer[91]. The alternating depth of the etched grating lines gives rise to a Fano mode with enhanced Q-factor. A switching metadevice, combining a structured gold film harbouring plasmonic resonances and singlemode

optical fibre tip, is capable of performing light modulation based on controllable (through tunable phase difference between propagating pump and probe beams) coherent absorption[92]. Wave-front manipulation relying on fibre tip-integrated metadevices has also been reported[93].

Merging metasurfaces with planar waveguides has also played a relevant role in the process of realising the exciting properties offered by metamaterials in a more applicable technological context[94,95]. Controlling propagation and coupling of waveguide modes is shown possible using phase-gradient metasurfaces based on gold gratings with varying width, fabricated on $LiNbO_3$ waveguides[94]. The phase-matching conditions for second-harmonic generation are met via the employment of gradient metasurfaces[95].

Besides fibre tips, the other prime contender to help boost metamaterial integration in optical-fibre networks is side-polished fibres. Fabrication of these specific optical fibre platforms is considerably more complex than the simple experimental procedure by which a normal fibre is cleaved in order to obtain a fibre tip. Nevertheless, some of its advantages make the added complexity worthwhile: reduced losses after interaction with potentially high-absorbing materials, given only evanescent interaction takes place; long interaction lengths which can improve the modulation depth; large planar area for thin film growth and patterning. So far, light modulators based on side-polished fibres have resulted from fibre integration of unpatterned thin films[96-98], which means light-modulating solutions developed from metamaterials merged with these waveguides are still an elusive alternative. The side-polished modulators proposed up to this point have relied on combining these platforms with thin films, which owing to their specific geometry, effectively bidimensional, allow polarisation-dependent intensity modulation: graphene- or MoS_2-coated side-polished fibres exhibit remarkable different levels of absorption depending on light polarisation relative to the plane containing the thin film.

Other relevant alternatives in the realm of fibre-integrated modulators have rested on fibre tapers[99-101], which end up achieving the main goal procured when employing side-polished fibres, which is bringing light guided along the core out to the external limit of the waveguide and enhance its interaction with the light-modulating medium deposited on this outer boundary. The main downside of this method is linked to the fact that tapers do not provide a planar area which raises experimental difficulties when it comes to film deposition and patterning.

Chalcogenide film integration in waveguiding systems has also proved to be an interesting solution for light modulation[102-106]. Integrated all-optical non-volatile memories, with possible multi-level operation, have been brought to the fore[102-104,106].

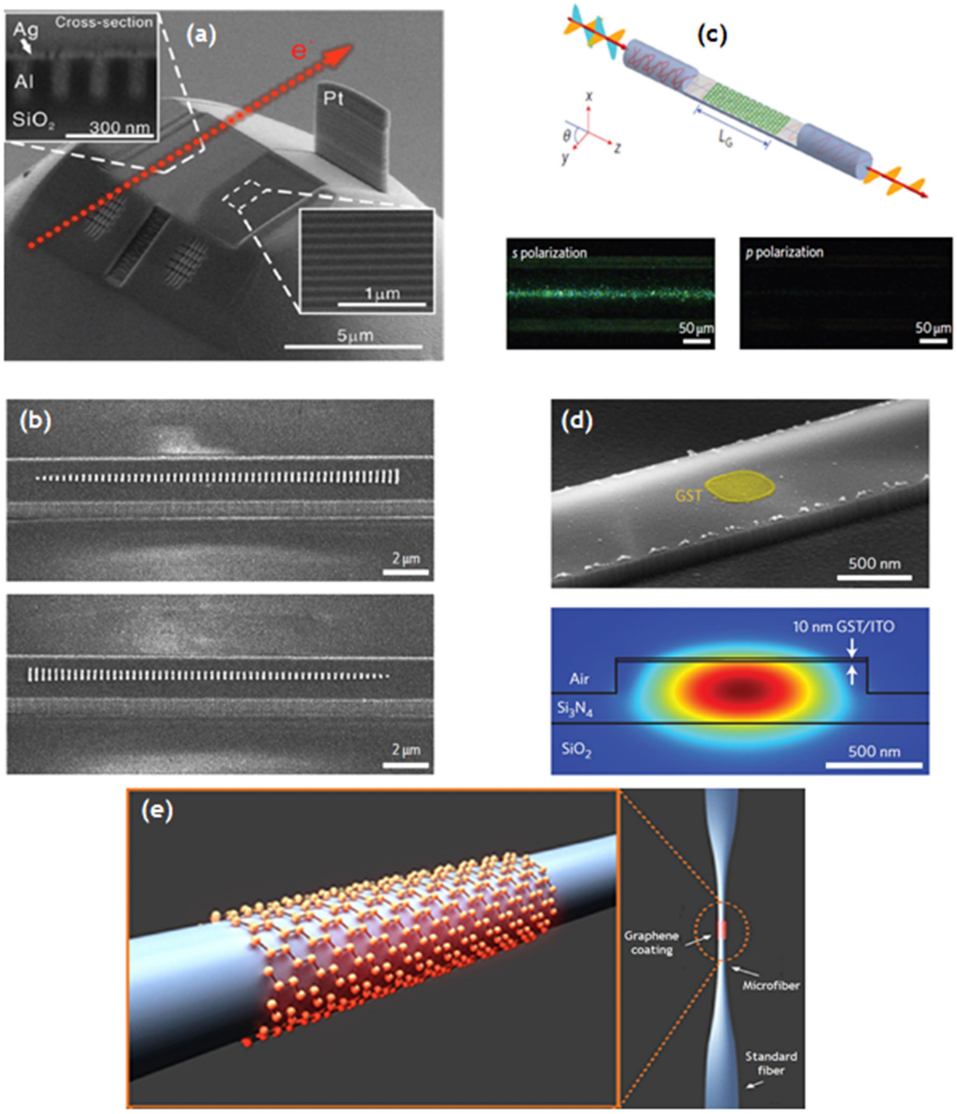


Figure 2 – (a) Structured fibre tip for amplification of the evanescent field of free electrons[90]; (b) gold metasurface on $LiNbO_3$ waveguides to control mode propagation[94]; (c) graphene-coated side-polished fibre for polarisation-dependent light modulation[96]; (d) GST-coated Si_3N_4 waveguide for non-volatile, multi-level integrated memory[104]; (e) graphene-coated microfibre[101].

1.4. Objectives and structure of the thesis

In order to realise the goal of bringing together chalcogenide material functionality and optical fibre platforms, two device configurations are proposed, one based on combining a thick GST film with a side-polished fibre and the other relying on a periodically structured film of the same phase-change material deposited on the flat facet of a cleaved fibre tip. In both designs, the chalcogenide film is placed within close proximity to the region of the waveguide where light is guided through, either promoting interaction of an evanescent nature, as is the case of the side-polished-based architecture, or leading to a scenario characterised by stronger light-matter interplay, as is the case of the fibre-tip device in which the GST layer intercepts light propagation through the fibre core. Under both these circumstances, induced structural phase changes of the chalcogenide material, inevitably linked to pronounced variations of its optical parameters, are expected to pave the way for considerable light modulation ratios, with potential applications in non-volatile memory devices, with the added advantage of possible integration with widespread and extensively used waveguiding structures.

This thesis is organised in eight chapters, being their contents as summarised in the following.

Chapter 1 provides an overview of some of the most significant scientific contributions in the field of metamaterials, nanophotonics and waveguide integration of functional thin films and structured media.

Chapter 2 catalogues and briefly describes tools and techniques employed throughout the experimental work developed in the context of this thesis.

Chapter 3 delves into the vibrant universe of chalcogenide materials, highlighting their most relevant properties and technologically relevant features, which place them as prime candidates for a vast spectrum of applications, from memory devices to light modulators in telecommunications networks.

Chapters 4 and **5** present numerical simulations and experimental results concerning the performance of light-modulation schemes combining a structured GST film with a cleaved fibre tip and a thick GST layer deposited on a side-polished fibre. The optical response of these configurations is studied for different values of the geometrical parameters and structural phases characterising both devices.

Chapter 6 aims at assessing the possibility of extending the principles of device operation established in **Chapter 4** to other metasurface designs. Huygen´s surfaces based on periodically arranged arrays of GST nanodiscs are considered.

Chapter 7 analysis in a purely numerical way the adequacy of designing asymmetric GST gratings as a means to enhance the Q-factor associated with light-matter interactions in this type of structures.

Chapter 8 summarises the main conclusions derived from the work carried out during this PhD project. A succinct overview of the possible next steps towards expanding the range of fibre-integrated phase-change devices and their technological appeal is included.

Journal articles

November 2019 – *Fiber-integrated phase-change reconfigurable optical attenuator,* **T. Martins,** B. Gholipour, D. Piccinotti, K. F. MacDonald, A. C. Peacock, O. Frazão, N. I. Zheludev – APL Photon., vol. 4, no. 11, 111301.

Being prepared – *Fibre-tip-integrated phase-change metasurfaces with switchable dispersion,* **T. Martins**, B. Gholipour, J.-Y. Ou, K. F. MacDonald, O. Frazão, N.I. Zheludev.

Communications in international conferences

April 2019 – *Phase-change photonic metamaterials,* K. F. MacDonald, D. Piccinotti, A. Karvounis, **T. Martins**, B. Gholipour, N. Zheludev, SPIE Defense + Commercial Sensing, Baltimore, United States.

April 2019 – *Chalcogenide phase-change photonic metamaterials*, B. Gholipour, D. Piccinotti, A. Karvounis, **T. Martins,** K. F. MacDonald, N. Zheludev, MRS Spring Meeting 2019, Phoenix, Arizona, United States.

June 2019 – *Fibre-integrated phase-change devices,* **T. Martins,** B. Gholipour, D. Piccinotti, K. F. MacDonald, A. C. Peacock, O. Frazão, N. I. Zheludev, IV International Conference on Applications of Optics and Photonics (AOP), Lisbon, Portugal.

August 2019 – *Chalcogenide reconfigurable metamaterials,* B. Gholipour, D. Piccinotti, **T. Martins**, A. Karvounis, K. F. MacDonald, N. Zheludev, SPIE Optics & Photonics 2019, San Jose, CA, United States.

2. Tools and techniques

2.1. Focused ion beam milling

Focused ion beam (FIB) milling is a versatile technique which, over the past years, has claimed a prominent role in a number of research areas, from materials science to nanophotonics, mostly owing to the high-resolution machining it can perform, an attribute combined with a remarkable flexibility when it comes to the etched geometries and the substrates into which the structures are carved[107,108]. The maximum resolution achievable using an FIB, around 10 nm, has revolutionised the field of metamaterial science, allowing metadevice operation to be transferred from the microwave region of the spectrum down to the infrared band, a wavelength range of pivotal importance in modern telecommunications.

Milling in an FIB system relies on the interaction between the sample being structured and the ion beam scanning over it. The etching mechanism is based on momentum transfer between the ions and the atoms in the sample. When the energy transferred through this process is high enough, atomic bonds within the sample are broken and particles are ejected with given kinetic energy. As a result of this interaction, other particles besides atoms are produced, namely secondary electrons which can be used to extract information regarding the surface of the sample.

In most FIB systems, a Ga ion source is used, given its advantages over other potential candidates, namely low melting temperature (30° C), low volatility and low vapour pressure, allowing for a stable ion source and beam. The main downside of employing a Ga ion source is the unavoidable Ga implantation that comes with fabrication under these conditions. As a result, the original stoichiometry of the sample is changed, requiring adjustments to post-processing. In the particular case of this work, Ga implantation inevitably changes the way GST responds to thermal annealing, affecting the crystallisation process. The optical response of the sample after FIB structuring will also reflect the presence of Ga. One way to circumvent this pernicious effect is using different ion sources, of the same material of the sample. These sources might not provide the same stability but, on the plus side, will not compromise the stoichiometry of the sample. When dealing with widespread materials such as Si in waveguide nanopatterning, this solution can prove to be not only effective in preserving the original composition of the sample but also less of a financially extravagant alternative.

In the FIB system used to fabricate the samples characterised in this project (FEI Helios NanoLab 600), electron and ion beams are generated in separate columns. Prior to adjusting the tilting angle of the stage on which the sample is mounted, the electron beam used to image the sample impinges perpendicularly on its surface, while the ion beam strikes at an angle of 52°. In

order to make sure the etched pattern corresponds to the design prepared in advance, tilting the stage at a 52° angle, thus guaranteeing the ion beam hits the sample at a 90° angle, is crucial.

Before reaching the sample, the ion beam passes through a collection of lenses and apertures to define the beam, its diameter and current and finally focus it on the specimen. Additional elements such as deflection plates to allow scanning the beam over the sample are also included in any conventional FIB system. The resolution of the machining procedure depends on the beam shape and diameter. Chromatic aberration and sputtering are among the principal limiting factors setting a maximum achievable resolution in FIB milling.

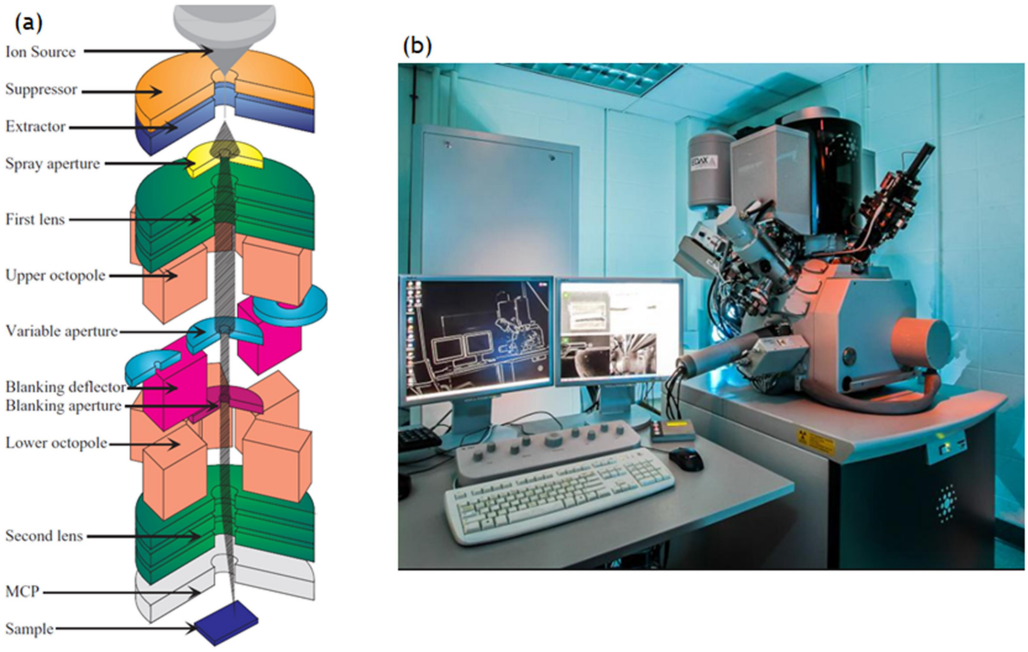


Figure 3 – (a) Schematic diagram featuring the main components of an FIB system[107]; (b) picture of an FIB workstation similar to the one used in this work[109].

The sputtering efficiency depends on a number of variables, mostly concerning the characteristics of the sample: crystallography, atomic mass and surface geometry. However, even when dealing with samples made out of the same material, sputtering yield can vary significantly. This is predominantly due to slight but impactful variations in, for instance, the grounding procedure carried out to make sure charge accumulation on dielectric samples, such as the GST films prepared for our devices, is mitigated. Connecting the sample to the metallic sample holder using carbon tape is usually the routine procedure to ensure charge dissipation from the specimen surface.

In addition to being used to perform machining and sample characterisation, FIB systems can assist material deposition, by decomposing gaseous precursors injected into the chamber and allowing the desired material to be deposited[107]. Such particularity can be explored to

promote the adhesion of a metallic layer onto the sample in order to protect it in later stages of milling. Cross-sectioning is one specific instance in which this aspect can be taken advantage of: a platinum layer is deposited on top of the sample area on which the cross-section is to be carved, guaranteeing the subsequently imaged features are reasonably preserved.

The sheer diversity of structures made possible by FIB machining is in itself an astonishing feat: nanometre apertures used to efficiently confine light at subwavelength scale in order to push beyond the resolution limits currently imposed on imaging techniques[110-113] or to enhance interaction between conventional waveguides and the near-fields of small light-emitting objects[114]; structured optical fibre tips for sensing applications[115-118]; phase-plates for beam shape conversion[119,120]; optical tweezers[121] and metamaterials of varied configurations[90,122].

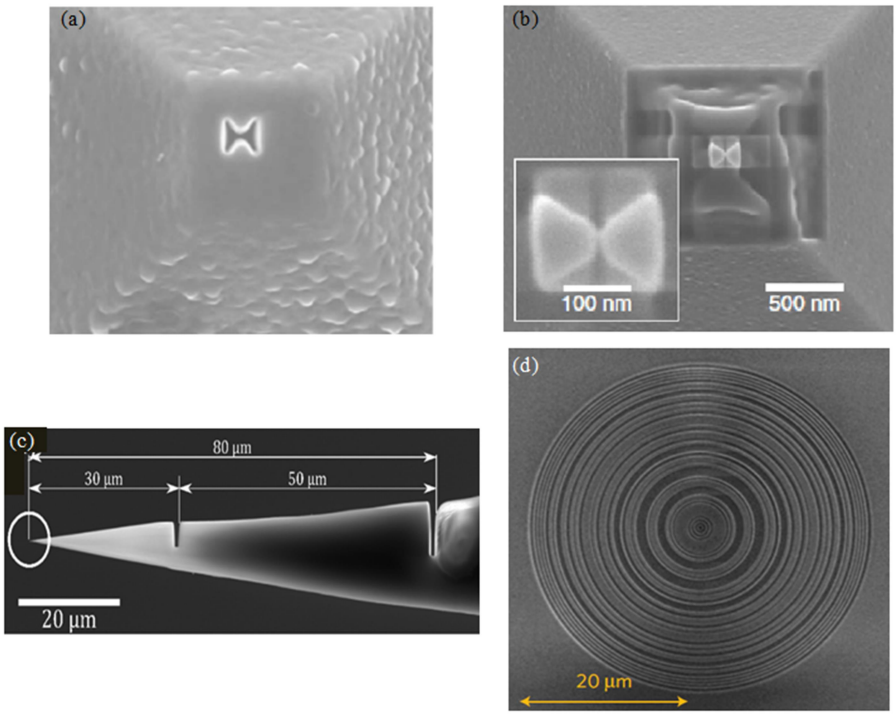


Figure 4 – FIB-milled devices: (a) bow-tie-shaped aperture for imaging with enhanced resolution[112]; (b) bow-tie-shaped antenna for enhanced interaction with a single quantum dot[114]; (c) Fabry-Pérot cavity in optical fibre micro-tips for sensing[118]; (d) super-oscillatory lens for subwavelength imaging[122].

2.2. Sputtering

Sputtering is a physical vapour deposition (PVD) process[123,124] used extensively in this work to deposit GST films on silica-based substrates, either flat glass substrates or optical fibres. A Kurt J. Lesker Nano 38 system was used throughout. The designation used to identify this process clearly highlights the physical mechanism underpinning deposition: the target, made out of the material to be deposited, is bombarded by ions and, through transfer of momentum, atoms from the target are ejected and sputtered onto the substrate surface, where atomically grown layers start stacking on top of each other. Ions are generated when the working gas, argon in this instance, is fed into the deposition chamber and is subsequently ionised by an electrical discharge, usually around 400 V. The rate at which Ar is injected into the chamber depends on whether the discharge is to be initiated or just maintained: igniting the plasma requires a higher injection ratio, around 70 cc/min, while around 37 cc/min should suffice to sustain it. Typically, the target is negatively charged, acting as an anode and attracting the positively charged Ar ions. Varying the applied voltage between target and substrate (acting as a cathode) allows controlling the kinetic energy with which ions reach the target. The sputtered atoms then travel through the low pressure atmosphere of the chamber, approximately 10^{-4} mbar, until they reach the substrate and start adhering and growing, atomic layer by atomic layer, up to the desired thickness. The rarefied atmosphere results in scarcer collisions between sputtered atoms and ions in the plasma, favouring a more direct path between target and substrate with obvious benefits regarding sputtering yield.

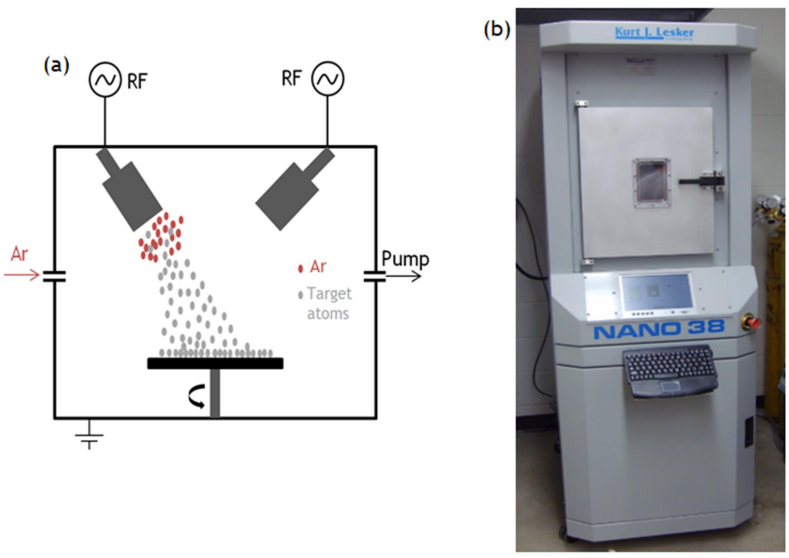


Figure 5 – (a) Schematic diagram of a typical RF sputtering system; (b) photograph of the utilised model of sputtering machine[125].

Understanding ion-surface interaction is important when employing sputtering as a film growth technique. Distinct phenomena can take place when an accelerated ion impinges on the target surface: ions may be reflected, scattered, sputter surface atoms or penetrate through the top layers and get implanted inside the target; surface heating and chemical reactions can also occur as a result of this interaction. Studying ejection probability, with its understandable close link to sputtering yield, as a function of the kinetic energy of the ionic species striking upon the target, is of definite interest in the context of this technique. Ions with low kinetic energy (accelerated using lower voltage) tend to adhere to the target by condensation and chemisorption, and few atoms are sputtered. As higher kinetic energies are considered, the ejection probability tends to increase, up to very high kinetic energies (ordinarily above 10^4 eV) for which it starts declining again as a result of ion implantation.

Sputtering yield, defined as the number of sputtered atoms divided by the number of incident ions depends on other variables besides kinetic energy: atomic elements in the target, crystallographic effects, and angle of incidence of ions upon hitting the target.

Radio frequency (RF) and magnetron sputtering are widely used. RF sputtering differs from DC sputtering in its featuring an alternating electrical potential preventing charge build-up on the surface of dielectric target materials. Magnetron sputtering adds a degree of freedom to the sputtering system by introducing a magnetic field, which could be used to control the trajectory and velocity of ions in the plasma. Since GST, a dielectric material, is the target material for deposition in this project, RF sputtering has necessarily to be considered over DC sputtering.

Reactive sputtering is an appealing solution for the deposition of oxides or nitrides: depending on the compound envisaged for thin film growth, either oxygen or nitrogen are injected into the chamber and undergo ionisation as a result of the multiple high-energy collisions taking place in the plasma; the then produced negatively charged ions are attracted to the substrate (acting as a cathode) and react with the deposited materials, forming the desired compound.

The main advantages of sputtering in relation to other deposition techniques such as thermal evaporation can be summarised as:

1. High kinetic energies, which can be controlled by changing the applied voltage, allow more efficient removal of target material, with consequent implications on the sputtering yield and film growth rate;

2. Given the physical process underlying particle ejection from the target, high temperatures are avoided and deposition on a variety of substrates potentially sensitive to such temperatures (e.g. polymers) is possible;
3. The versatility introduced by variations of this technique (RF, magnetron and reactive) also places it a few notches above evaporation;
4. Since atoms are sputtered through momentum transfer, the stoichiometry of the target is preserved and the composition of the deposited film reproduces that of the initial compound;
5. Tuning of the film properties can be achieved by varying some of the deposition parameters such as applied voltage (as noted previously, intimately connected with kinetic energy of the ionic species arriving at the target), pressure inside the chamber or type of working gas.

2.3. Thermal evaporation

Thermal evaporation is another PVD process used to grow thin films[124]. In the context of this project, thermal evaporation was seldom used, but resorted to in order to deposit metallic layers on fibre tips intended to act as mirrors and serve referencing purposes when measuring the reflection spectra of our fibre-optic devices. An Edwards Auto 360 system was used.

As is the case of sputtering, thermal evaporation begins with the formation of an atomic gas. The resulting atomic particles travel in a low-pressure environment towards the substrate and start adhering on its surface and grow atomistically up to the desired thickness. However, the physical process which triggers the formation of the atomic gas differs substantially between these two techniques. As mentioned in the previous section, momentum transfer is the mechanism generating ejected atoms in sputtering systems, while, when it comes to thermal evaporation, these particles are produced by transferring thermal energy to the target: when this energy is high enough, evaporation takes place; higher energies can lead to complete sublimation of the target material. Usually, a controlled and organised growth is privileged, meaning this latter scenario tends to be avoided.

The means by which evaporation is set in motion is quite straightforward: electrical current passes through a resistive element where the material to be deposit is held and, through Joule heating, thermal energy is transferred into this material, causing it to evaporate. The gas fills the deposition chamber and adheres to all exposed surfaces, including the intended substrate.

Deposition of materials with high evaporation temperatures can pose a significant challenge. Development of suitable Joule heating sources, mostly made out of tungsten, has helped dealing with this problem. Nevertheless, when the evaporation temperature of the target material approaches that of the heating source, contamination can occur, compromising film purity.

Deposition of composite materials is made more complex by the fact target material is heated in order to generate an atomic gas: materials with different vapour pressures will start evaporating at different temperatures and at different rates, making preservation of the original stoichiometry harder.

Evaporation by heating the target material also means the temperature of the deposition chamber will rise throughout the process, a fact which invalidates the possibility of depositing on materials more sensitive to high temperatures.

In the framework of the experiments carried out in this project, deciding on whether to use thermal evaporation or sputtering relies on assessing the suitability of each technique for depositing the materials under investigation. Given the complex stoichiometry of GST, sputtering is chosen over thermal evaporation. Depositing metals such as Ag, used to coat fibre tips for referencing purposes, could be carried out efficiently with thermal evaporation, owing to its higher growth rate, to the fact Ag is a simple substance with an evaporation temperature well below that of tungsten.

2.4. Reactive ion etching

Reactive ion etching (RIE) has been comprehensively used in semiconductor research and industry as a powerful tool used to etch through silicon and define integrated circuits[126]. In this work, RIE is employed to clean side-polished fibers, guaranteeing wax remnants left over from the polishing process are completely removed from the polished surface, leaving only a smooth substrate for the subsequent deposition of thin films. An Oxford Plasmalab 80 plus system was used.

RIE falls into the category of plasma etching. As described in the case of sputtering deposition, plasma is obtained after an electrical discharge applied to the working gas ionises it. An RF field sets the electrons and ions in the plasma in an oscillating motion between wafer platter and the upper part of the chamber. The frequency of oscillation only allows lighter particles, such as electrons, to accompany the rapidly varying polarity of the electric field,

leaving the more massive ions stranded in the centre of the chamber. As a result, a voltage difference is set up between the positive ions in the plasma and the negatively charged DC-isolated wafer platter. The accelerated ions strike the substrate on the wafer platter, etching it. This configuration ensures the ions are mostly accelerated perpendicularly to the substrate surface, leading to anisotropic etching.

Several degrees of freedom are at play when resorting to this technique. Of particular interest, bearing in mind our aim of simply cleaning side-polished fibres without any further concern regarding pattern etching, are the ionic species used, their volume percentage and etching time. Ar and O_2 are fed into the chamber with different volume percentages, 70% and 30%, respectively. O_2 is added into the mix given its affinity with organic compounds and the associated potential increase in the etching efficiency of the wax remnants, leaving the underlying glass relatively undamaged. Etching times vary depending on the degree of uncleanliness of the fibres, but etching runs of around 30 mins have proved successful in removing most of the dirt from the fibres, as attested by later SEM inspections. The pressure inside the chamber is usually set to $\sim 10^{-4}$ mbar.

Other contexts have favoured a more imaginative utilisation of this technique. Integrated circuitry in silicon wafers and advances in microelectromechanical systems (MEMS) owe a great deal to Deep Reactive Ion Etching (DRIE), allowing good quality high aspect ratio (HRA) trenches to be fashioned[127,128].

2.5. Polishing techniques

Side-polished fibres enable access to the evanescent field of the mode propagating along an optical fibre, by bringing the outer boundary of the waveguide closer to the core region, as a result of removing a portion of the cladding. The techniques employed to meet this end ensure a flat substrate is obtained, with a length along the propagation direction and a distance to the fibre core easily controllable during fabrication[129]. The transmission characteristics of the fibre are highly dependent on these fabrication parameters[130], but also on the properties of the medium deposited on top of the polished surface. Thin metallic films in close proximity to the fibre core can give rise to surface plasmon resonances[131] with spectral characteristics sensitive to the configuration of the side-polished fibre, but also to the film thickness and optical properties. Coupling to thicker overlay layers also introduces resonances in the spectral response of the fibre[132,133]. Several sensing schemes based on assessing transmission changes deriving from variations of external parameters in devices of this sort have been proposed[131-137].

Mechanical polishing is usually deployed as a means to remove a section of the cladding layer, exposing the area just above the core and allowing tapping into the evanescent light in optical fibers. The polishing wheel technique[129] consists in suspending a stripped optical fibre under slight tension over the polishing wheel, which spins at a given speed. In order to obtain a smoother polished surface, the wheel is lubricated with liquid paraffin. Both the polished length and depth (distance from polished plane to the fibre core) can be controlled, either by setting the appropriate polishing wheel diameter and the contact angle of the fibre on the wheel, or by running the process for the adequate amount of time, respectively. The longest polished lengths, around a few centimetres, can be quite substantial, especially if compared with the typical operation wavelength in optical fibre telecommunications, yielding ratios of about 2×10^4, which translates into potentially deep light-matter interaction. Reaching the vicinity of the core (i.e. within the decay length of the field outside the fibre core, around 2 μm) takes just a few minutes. Throughout the fabrication routine, transmission characteristics are monitored.

In the case of the polishing block technique, the fibre is stripped of its protective polymer jacket and bonded, using wax, into a groove cut through a metallic block. The depth of the groove is such that it allows polishing to the desired depth: deeper grooves will produce a polished plane very close to the core. A thick film of, for instance, aluminium oxide[97] is used to remove the bulk of the cladding section, while a proprietary polishing film is used to finish it off, making smooth surfaces of up to ~ 1 nm root mean square (of the roughness distribution) possible.

An important detail of the post-fabrication characterisation concerns the determination of the polishing depth[130]. Preliminary measurements have to be carried out, essentially aiming at linking a given measured loss to the distance between core and polished plane. For each item in a set of side-polished fibres with varying core-to-plane distances (shorter distances associated with longer polishing times), transmitted power is taken after depositing a high-index oil layer on the device. Different mixtures are tested, which allows plotting a transmitted power vs. oil index graph, for each of the fibres. The graph typically shows that, for all fibres under evaluation, as higher oil indices are considered, lower transmitted power is measured, eventually reaching a steady value. This value depends on the polishing depth and, as expected, goes down as deeper polishing is performed (the core is more exposed and light is less well confined). These experimental curves fit in relatively well with theoretical predictions, allowing assigning an approximate core-to-plane distance to a given “steady-state” value. In short, after measuring transmission for different overlay indices, a steady value is found, which allows estimating how close the polished plane is to the fibre core.

2.6. Scanning electron microscopy

Scanning electron microscopy (SEM) is a rather valuable characterisation technique when studying the surface morphology of varied structures[124], from continuous and patterned thin films to the roughness of the polished surface of a side-polished fibre.

This technique is based on collecting and characterising electrons after they interact with the sample under investigation. As hinted at by its designation, SEM images result from an accumulation of local pictures, gathered as the electron beam scans over the sample. This beam is thermionically generated by a filament in the SEM column and passes through a collection of apertures, condenser lenses, deflection coils and objectives with the purpose of defining its shape and size. Given the low mass of electrons, their penetrative power into the SEM-imaged sample is reduced and the interaction is confined to the topmost layers, resulting that most information concerns the surface.

From the interaction between the electrons in the SEM beam and the sample, secondary and backscattered electrons along with X-rays are generated, carrying with them distinct information. Upon impinging on the sample, electrons transfer energy inelastically to other electrons bound to atoms and to the lattice. The electrons proceed to scatter their way into deeper regions of the sample until they no longer possess the necessary energy to trigger these events. In the meantime, a legacy of electronic excitations is established and a number of electrons leaves the specimen and is up for detection.

Secondary electrons are the least energetic electrons reaching the detectors. They are commonly chosen as the primary providers of surface-related information precisely given their low energy, meaning they emanate from the topmost layers of the sample. Depending on the number of secondary electrons produced by a given region of the sample, the SEM image will appear darker or brighter, giving a sense of depth. Taking as an example the characteristic topography of one of our samples, consisting of arrays of GST cubes separated amongst themselves by deep, narrow trenches cutting all the way through the film into the substrate, an almost binary colour code, with bright grey and dark areas, characterises the obtained SEM picture. Bright grey areas, corresponding to the GST cubes, identify regions where more secondary electrons are generated, whereas dark areas, corresponding to the trenches, are those where fewer of these particles originate from.

Backscattered electrons are elastically scattered and, as a result, have higher energy than the inelastically scattered secondary electrons. The number of detected backscattered electrons depends on the atomic number of the specimen being imaged. Even though identification of the

specific materials making up the sample is not feasible, contrast between areas with different compositions (made up of elements with different atomic number) is usually good enough to infer how compositionally diverse the specimen is.

X-ray radiation emitted after the atoms in the sample are excited by the electrons in the SEM beam contains precious information concerning the composition of the specimen: different atoms will emit X-rays with different energy and the concentration of a given element can be derived from the number of X-ray photons generated by emission from atoms of that same element (photons with a given energy, characteristic of the electronic levels of that element).

2.7. Thickness characterisation

Measuring thin film thickness can be accomplished by cutting a cross section using an FIB machine and imaging it with an SEM beam. Resorting to a profilometer is perhaps a quicker and more straightforward method. The need to use this piece of equipment is dictated by the unfortunate fact that the sputtering machine employed in the fabrication of GST thin films lacks a reliable tool for thickness monitoring during deposition.

The profilometer engaged in our measurements (P-16+ Stylus Surface Profiler) performs a contact-based reading of the thickness. A calibration run is carried out in advance: a piece of glass substrate is covered along its length with a strand of kapton tape, meaning GST will only adhere onto the glass outside this area; after the deposition run is finished, the stripe of kapton tape is removed and the glass underneath exposed. Running the stylus of the profilometer along a direction perpendicular to the length of bare glass will provide a profile trace of the trench, allowing for an estimate of the film thickness to be obtained. Assuming film thickness increases linearly with deposition time, the required duration of the final deposition run can be determined based on the desired film thickness and the calibration information, which pretty much tells the growth rate. Repeating this procedure prior to every deposition is advised, given slight variations concerning, for instance, vacuum level can take place when there is an interval of a few days between depositions, or when other users deposit other materials, potentially contaminating, even if only slightly, the deposition chamber. All these oscillations of the parameters characterising the operation of the sputtering machine can affect the growth rate, stressing the importance of running a calibration run on a regular basis before the final deposition.

The working principle of a profilometer is quite simple. The stylus, with a diameter varying from a few tens of nanometres up to a few micrometres, scans the sample over a

horizontal direction previously defined by the user (in the case of the calibration runs performed in the context of this work, in a direction perpendicular to the length of the exposed glass to allow tracing the trench profile). All the while, the stylus is in contact with the sample surface and variations in its vertical (relative to the sample surface) position as induced by the topography of the specimen are registered. A final trace relating surface height and distance along the scanning direction is produced. Several parameters can be defined by the user such as scanned direction and length, scanning speed and stylus tracking force (typically a few milligrams).

2.8. Spectral characterisation

Spectral characterisation is a key step in this project, providing a thorough assessment of the optical response of the fabricated devices. Interaction between electromagnetic radiation and the structures investigated throughout this project can be reasonable well characterised by evaluating the reflection and transmission spectra of light. Depending on whether the device being tested is a fibre-coupled one or merely based on a structure fabricated on a flat glass substrate, an Optical Spectrum Analyser (OSA, Ando AQ-6315E) or a CRAIC microspectrophotometer (CRAIC QDI2010) is used, respectively.

The working principle of both pieces of equipment is the same: light resulting from interaction with the device passes through a diffractive unit and is split into very narrow wavelength bands. The power associated with each of these bands is detected by photon counters and a graph relating power to wavelength is produced.

In the specific case of CRAIC measurements, the spectrometer is combined with an optical microscope to allow identifying the area of interest on the flat substrate where the structure was fabricated and make sure illumination is cast upon it. A set of apertures and diaphragms are used to define the illumination beam diameter and intensity. Two sources are available, one in the ultraviolet part of the spectrum and the other one in the visible and near-infrared bands (up to 2 μm). Taking into account our favoured spectral region of operation, the latter source is used. Two individual sets of visible/near-infrared sources are in place. One is used for transmission measurements, providing illumination from the bottom for subsequent collection at the spectrometer on top of the microscope column. The other is used for reflection measurements, providing illumination from the top, which is then divided by a beam splitter into two propagation paths, one leading to the sample; light reflected by the sample travels up to the beam splitter and is again divided, one path leading to the spectrometer. Usually, a reference

for both transmission and reflection has to be taken prior to measurements. In the case of transmission, the reference is provided by simply collecting light generated by the transmission source prior to placing any substrate that would intercept its propagation path. When measuring reflection, a mirror is used.

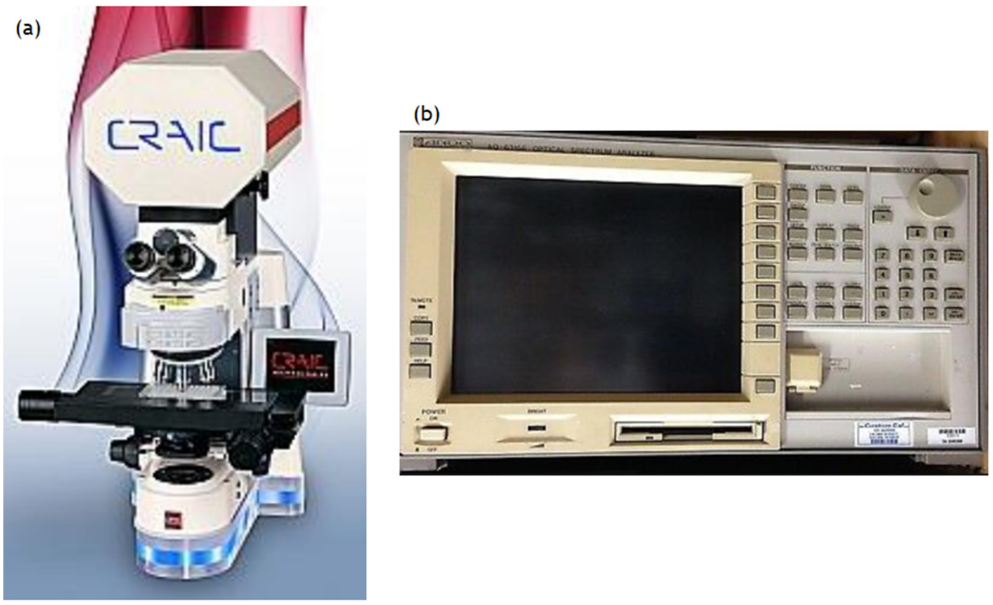


Figure 6 – (a) Craic microspectrophotometer[138]; (b) OSA[139].

OSA utilisation requires slightly different setting up. Light from a near-infrared source (Thorlabs SLS201L) is coupled into the device and the output is fed into the OSA. When characterising devices based on side-polished fibres, injecting light into them is no major challenge, since both input and output ends are connectorised. However, fibre tips pose a more interesting problem since the input end incorporates the structured facet, meaning attaching it to the source using a connector is not an option. A roundabout way of adequately illuminating the sample in these peculiar circumstances is using an objective (Mitutoyo M Plan Apo NIR 10x; NA = 0.26) to focus light from the source directly onto the structured tip; light resulting from this interaction is then directly fed into an OSA using a connectorised fibre end. This answers the question of how to retrieve the transmission spectra of our fibre-coupled devices. Reflection measurements need be aided by the inclusion of a 50/50 coupler (Thorlabs 10202A-50 - 2x2 SM Coupler) in the experimental setup. As Figure 7 shows, light from the source travels up to the coupler and is divided into two paths, one leading to the sample being characterised. Light reflected from the sample reaches the coupler again and half of it is directed towards the OSA. A coupler is chosen over an optical circulator given its typically wider wavelength band of operation. The obvious downside of this approach is high power loss occurring when light passes through the coupler.

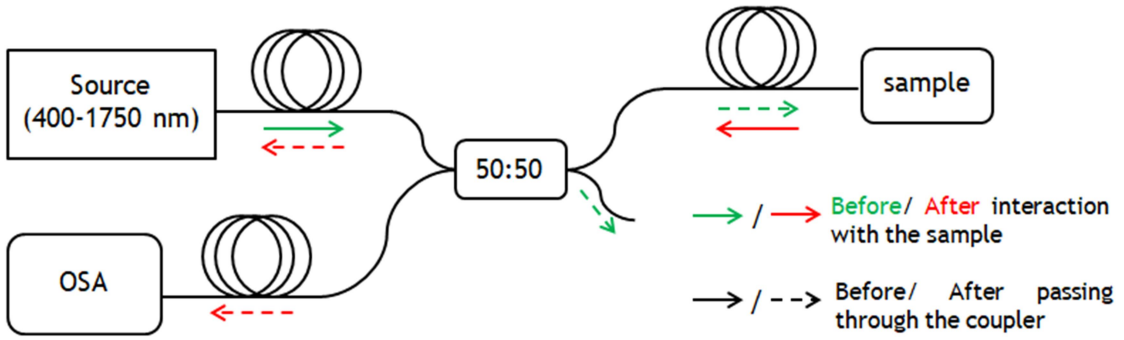


Figure 7 – Schematic diagram of the experimental setup for measurement of the reflection characteristics of fibre-integrated devices.

3. Chalcogenides

Chalcogenides are composite materials, being one of the constituents an element of the chalcogenide family, either sulphur (S), selenium (Se) or tellurium (Te). Germanium-Antimony-Telluride (GST), an integral part of all the devices characterised throughout this thesis, contains Te as the representative of the chalcogenide family; antimony (Sb) and germanium (Ge) assure a cohesive network is formed. The striking variability of the final stoichiometry of these compounds, given the number of chalcogenide elements and all the possible combinations with other network formers (gallium, silicon, phosphorus, arsenic), opens up the path for the creation of an exceptional number of different materials with distinct physical properties.

The overwhelming catalogue of properties these materials possess has deep technological implications in the fields of data storage[140-145], sensing and optical communication[146,147], as well as reconfigurable metamaterials[34-36,89,148-153]. Data storage was the first area of research to make good use of the particular characteristics of the crystallisation dynamics of these materials. The amorphous and crystalline phases of chalcogenide glasses are defined by starkly distinct optical properties[154]: upon crystallisation, the real part of the refractive index and the extinction coefficient increase conspicuously; in addition, electrical properties also suffer significant modulation, being the amorphous phase characterised by higher electrical resistivity[155]. The origin of the pronounced change in physical properties has been probed extensively over the last decades[2,140,143,146,147,156-159]. Unlike most semiconducting materials, where changes in the real part of the refractive index are usually tied to variations in material density, the concomitant variation of refractive index upon changing the phase of a chalcogenide material is due to the onset of a new bonding mechanism: in the crystalline phase, resonance bonding prevails, where two adjacent atoms are held together by a single electron; as for the amorphous phase, covalent bonding dominates. The prevalent bonding mechanism in the crystalline phase allows for high electronic polarizabilities, which translate into a higher optical dielectric constant, resulting in higher refractive index.

Phase transitions in chalcogenides are non-volatile, reversible and potentially fast[2]. Non-volatile transitions are made possible by the fact that the atomic arrangement of both amorphous and crystalline phases freezes into a stable configuration after the external stimulus triggering phase transition is applied and subsequently removed. Reversible means conversion between the two structural phases can be reversed: after moving from the amorphous to the crystalline state, a reversion to the amorphous state is possible, making rewritable memories based on phase-change materials (PCM) a reality. Amorphous-to-crystalline transitions are promoted by locally heating the sample above the glass transition temperature (T_g), rendering the atoms more mobile and allowing them to lock into the energetically more favourable crystalline state. Heat can be transferred into the chalcogenide material by a number of mechanisms: by raising the ambient temperature using a furnace or a hot plate; by locally heating the sample employing a CW or a

pulsed laser. Reverting back to the amorphous state is usually accomplished by a very short, high-power pulse, which rapidly heats the material above its melting temperature (T_m) but also quickly removes the thermal excitation afterwards, setting off a fast quenching process. The speed of these processes is limited by the slowest one, which is crystallisation (understandably, given its characteristically higher degree of structural organisation). The crystallisation speed is typically of the order of a few nanoseconds, compatible with devices operating at a few GHz.

Figure 8 conveniently illustrates in a graphic summary the differences in optical properties between the amorphous and crystalline phases of three PCMs: GeTe, $Ge_2Sb_2Te_5$ and $GeSb_2Te_4$. Along with these results, the behaviour of two ordinary covalent semiconductors, $AgInTe_2$ and InSb, upon crystallisation, is also plotted. Coherently with the previously described way in which crystallisation affects the bonding mechanisms in chalcogenides and conventional semiconducting materials, these graphs show the impact of a structural phase change on the optical parameters evaluated is more noticeable for the three PCMs.

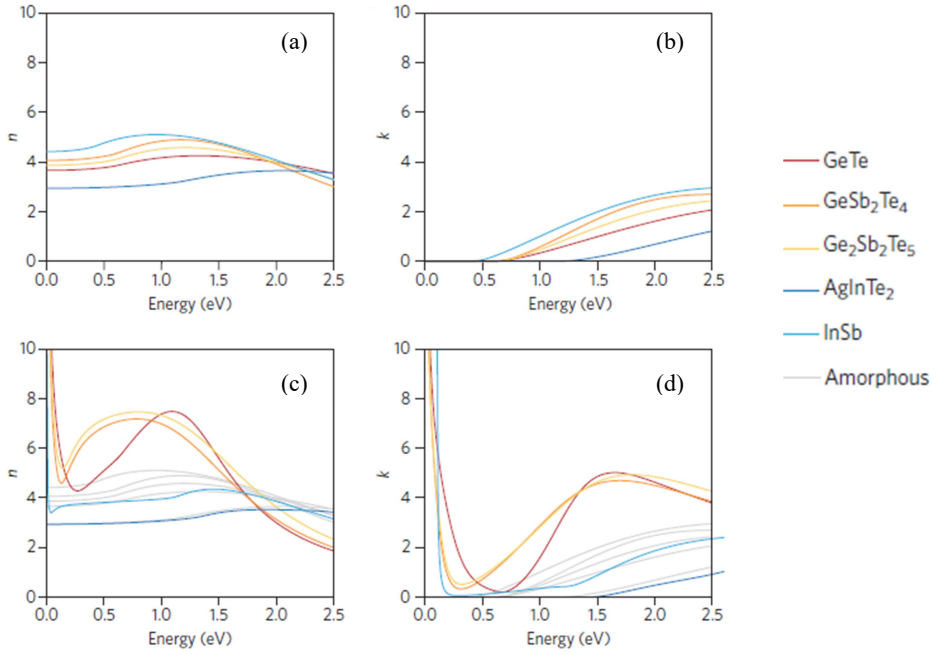


Figure 8 – Real part of the refractive index (n) and extinction coefficient (k) spectra for three different PCMS (GeTe, $Ge_2Sb_2Te_5$ and $GeSb_2Te_4$) and two ordinary covalent semiconducting materials, $AgInTe_2$ and InSb, in the amorphous (a, b) and crystalline (c, d) phases. Grey lines in c and d show results in the amorphous state for swifter comparison with those in the crystalline phase (adapted from [134]).

A brief introductory note regarding grey-scale crystallisation is of some pertinence, born of the formal framework designed for this thesis, granting a short preliminary chapter to the topic of chalcogenide materials, but also emerging from the more insistent utilisation of this refined crystallisation technique in technological solutions incorporating PCMs[102-104,106,146]. When applying short laser pulses to induce crystallisation of a chalcogenide layer, transition

from amorphous to crystalline phases is a gradual process rather than an instantaneous one: as a succession of pulses arrives at the sample, the degree of crystallinity progressively increases from a state of amorphous organisation to a fully crystallised structure. The massive change in optical properties between amorphous and crystalline states allows room for a still substantial variation of these properties even when only a fraction of crystallisation has occurred. Multi-level data storage based on this particularity of chalcogenide glass crystallisation has been reported[102,104] and has the potential for considerably increasing computation capability.

Another interesting property results from the combination of a high real part of the refractive index (n) and a low extinction coefficient (κ) in the infrared band, making chalcogenide materials good candidates for waveguiding applications. Amorphous GST, in the 1550-nm band, the wavelength range of choice in telecommunications, has n = 3.5 and a low $\kappa = 0.006$ (light propagates 13 wavelengths before its intensity drops to $1/e$ of its initial value). These distinctive optical properties arise from the unique atomic configuration of chalcogenides. High n is generally attributed to higher glass densities and stronger polarizability than registered for more conventional dielectric materials such as silica (SiO_2). Lower κ is linked to reduced absorption for infrared wavelengths: weaker inter-atomic bonds relative to those in oxides shift the bandgap to the visible. The magnitude of nonlinear effects, as predicted by Miller´s rule, is also expected to be high, giving rise to a multitude of practical implementations.

A more in-depth look into the crystalline structure of the chalcogenide material of choice for this project (GST) is worth the trouble. In the typical crystalline rock-salt-like structure of crystallised GST, Te atoms occupy one sublattice and Ge/Sb or vacancies occupy the other sublattice, as seen in Figure 9. The nearest-neighbour spacing is approximately 3 Å. When compared to binary chalcogenides such as As_2Se_3, this ternary compound presents increased network rigidity, higher T_g, strength and hardness. This is accomplished by an effectively three-dimensional network, where Ge atoms (network formers) create bonds between layers. Vacancies appear as a way to annihilate energetically unfavourable network organisation perks.

Changing the compositional configuration of chalcogenide compounds, i.e. varying the relative weights of the constituent elements, and studying its effect on material properties has spurred a considerable slew of publications[2,140,155,157,160]. Optical properties are significantly influenced by variations in the Ge content in GST: as this content increases along the pseudo-binary line, both n and κ increase (at least for a 405-nm wavelength)[2]. The impact of fluctuations in the concentration of vacancies and local network distortions on the properties of GST has also been assessed[159].

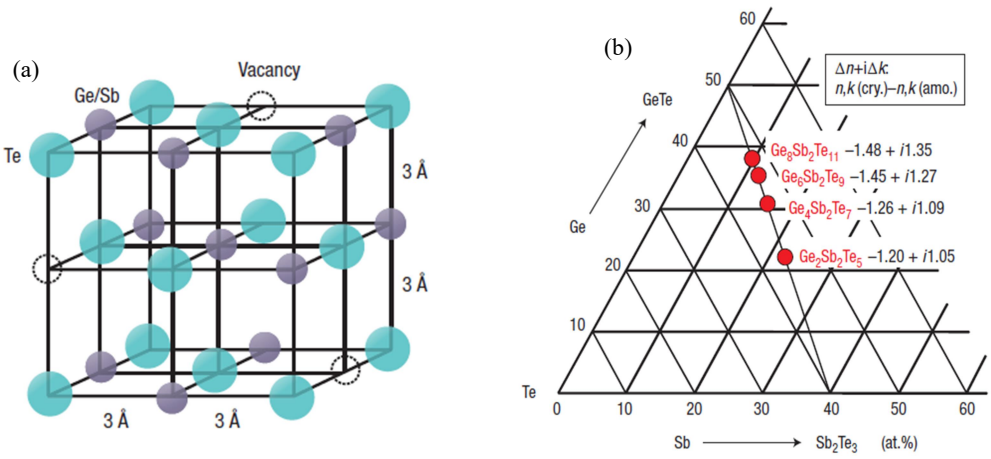


Figure 9 – (a) Crystalline structure of GST; (b) changes in optical properties (n and κ) as Ge content varies. (adapted from [2]).

Stoichiometry also determines the dynamics of crystallisation[140,143,157]. One of the first inquiries into this revealed diverse stoichiometries lead to different phase transition temperatures and distinct laser pulse durations are required to trigger these structural conversions[140]. Differential scanning calorimetry (DSC) results indicate that compounds of the GST group have crystallisation temperatures around 140 °C and reamorphisation temperatures close to 600 °C. The general trend identified in this work points to typically higher crystallisation temperatures as a result of higher Ge content. The process of laser-crystallising GST compounds of the kind $Ge_2Sb_{2+x}Te_5$, with varying concentration of Sb, has been studied[143]. Deviations from the pseudo-binary line (x = 0) affect crystallisation rates and critical temperatures of amorphous GST films. This is ascribed to the fact the excess Sb atoms remain in the amorphous state and concentrate at the grain boundary. Acceleration of crystallisation speed has been reported via addition of Sn[157]. Nucleation in the amorphous phase is favoured by the inclusion of Sn, making crystallisation faster and reducing its temperature. All the while, the crystalline structure retains the same single-phase-NaCl-type structure.

The dielectric nature of chalcogenide materials that this discussion has been confined to is wavelength dependent. In the visible/UV range, chalcogenides usually exhibit plasmonic behaviour (characterised by a negative value of the real part of the permittivity), as is the case of GST. One example of the richness of the optical response of these materials is the compositionally controlled plasmonics in amorphous BiTe compounds[161]. A plasmonic response over a band extending from 250 nm to between 530 nm and 978 nm, depending on alloy composition, is obtained. Obtaining plasmonic behaviour from materials other than metals, where optical losses are quite substantial, is an important step forward in bringing devices based on this physical phenomenon closer to practical applications. Exploring epsilon-near-zero

(ENZ) behaviour in chalcogenide glasses, verified at optical frequencies, as allowed interesting phenomena to be observed[54]: an array of subwavelength apertures in a metal film is filled with a chalcogenide semiconductor acting as a low-epsilon medium, leading to increased transmission. In the band of more exotic properties hosted by chalcogenide materials, one can also count topological insulation[58,59].

The main properties qualifying PCMs for application in technological solutions, among which data storage and optical switching are prime examples, are summarised below, along with specifications as to how they can best be taken advantage of.

Property	Specification
• High-speed phase transition;	• Induced by nanosecond laser pulse;
• Long stability of amorphous and crystalline states (non-volatile operation);	• Several decades at room temperature;
• Large optical change between the two structural phases (high switching modulation);	• Considerable difference in n and κ;
• Large cycle number of reversible transitions;	• More than 100,000 cycles;
• Chemical stability.	• High water-resistivity.

Table 1 – Technologically appealing properties of PCMs (adapted from [2]).

The properties of chalcogenide materials compiled in this brief introduction show unequivocally their technological relevance and, in particular, their suitability for inclusion in light-modulating devices. Given the fact the main aim of this thesis is to produce optical switches for integration with optical fibres, the employment of these thoroughly studied materials with proven advantages over other phase change media is a sensible choice. GST is chosen over other possible chalcogenides given the vast amount of research efforts dedicated to investigating its properties and crystallisation dynamics, providing a solid background of experimental knowledge, which makes leveraging their potential for optical switching in fibre-integrated devices less fraught with possible mishaps.

Data storage was the inaugural rite of passage for chalcogenides in their transition from being a novelty in the field of material science to scalable technological applications. Early work by Ovshinsky[156] had already demonstrated that reversible electrical switching in disordered structures could be achieved. In the following decades several new chalcogenide

compounds were discovered bringing different properties to the table. The first optical storage products based on these compounds started appearing in the early 1990s[141,142,160].

Since this primordial awakening of research revolving around chalcogenide materials, other applications have entered the picture. Considering the scope of this work, focus on metamaterials and waveguide-integrated devices is privileged in the following.

Reconfigurable metadevices have benefited a great deal from developments in chalcogenide semiconducting materials. Metamaterial reconfigurability can be enabled by mechanical actuation, which is complex and typically difficult to integrate in compact devices. The change in optical properties experienced by chalcogenides, upon phase transition, grants access to distinct metamaterial optical responses. Faster reconfiguration, limited by crystallisation speed (of the order of a few nanoseconds), is also attainable resorting to these phase-change media, when compared to geometrical rearrangement of the metastructure. In addition, multiple strategies can be engaged to induce structural phase conversion, from electrically to optically and heat-induced transitions. The ease with which PCMs can be combined with waveguides allows active control over the propagation of electromagnetic radiation along these structures. Monolithic devices ready for incorporation in telecommunication networks can thus be produced.

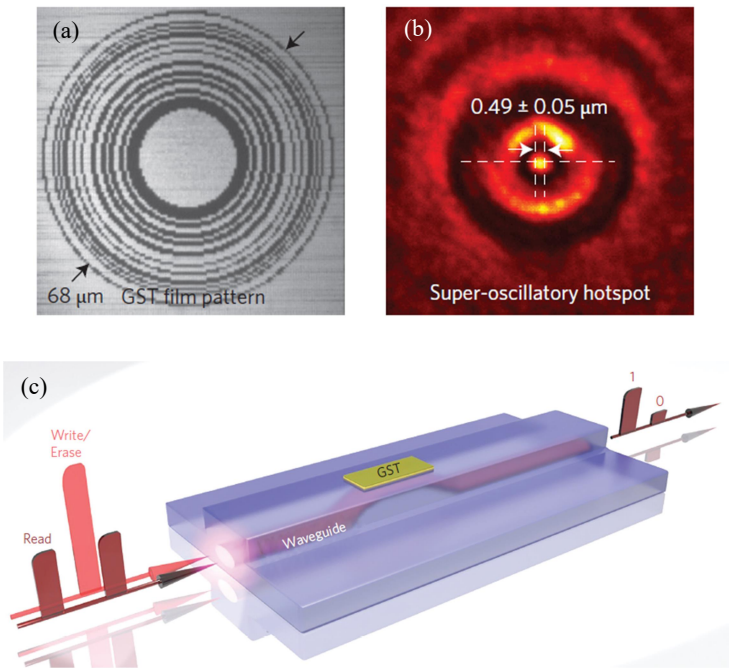


Figure 10 – (a) Super-oscillatory lens etched into a GST film using a femtosecond laser[152]; (b) corresponding hotspot; (c) schematic diagram of a GST film integrated into a waveguide[104].

4. Fibre tip-integrated phase-change metasurfaces

4.1. Introduction

Waveguide-integration of metamaterials has been the focus of a considerable number of research efforts[90-95], aiming at bringing the compelling physical properties hosted by metamaterials to the realm of practical devices based on widely implemented and mature waveguiding platforms, such as optical fibres.

This section addresses the fabrication and optical characterisation, both numerical and experimental, of fibre-integrated metasurfaces based on FIB-milled GST films deposited on cleaved fibre tips. Structuring the chalcogenide film enables the introduction of resonances in the transmission and reflection spectra. Tailoring the resonant wavelength as well as Q-factor is achievable by adjusting the metamolecule geometry, allowing placing the spectral feature in the wavelength band of interest, in this particular case, the near-infrared range, where conventional optical fibre communication is performed. Numerical simulations and experimental results demonstrate that this spectral tuning is in fact possible. The nature of the resonance is also probed by analysing the simulated field maps.

The spectral modifications linked to light-induced structural phase-change are investigated. Switchable intensity and dispersion control are reported, with modulation spectra which can be engineered by acting upon the geometry of the metamolecule or by promoting gradual crystallisation of the GST layer. An all-fibre setup where crystallisation is triggered by illuminating the metasurfaces with a continuous wave (CW) laser is designed, providing an elegant solution for a compact device where all-optical switching can be implemented.

4.2. Simulations

Simulations are run using a finite element numerical solver (COMSOL). The 3D model assumes a lossless non-dispersive silica substrate with refractive index of 1.45 and uses ellipsometrically measured values of the complex permittivity of GST, as presented in Figure 11a. The crystalline state exhibits a significantly higher refractive index, around 6 from 3.5 in the amorphous state at 1550 nm, and an enhanced extinction coefficient, around 0.7 from 0.01 before crystallisation, also at 1550 nm. In addition, normal-incidence illumination using a plane-wave is considered. The electric field is set perpendicular to the direction of propagation, along one of the lengths of the GST block sitting on top of the silica substrate. The top corners of the blocks are slightly rounded to account for over-milling during FIB fabrication. Light incidence upon the modelled structure is determined by the specifications of the two periodic ports, which allow choosing whether light travels from port 1 to port 2 or the other way around, the input power, angle of incidence and refractive index of the medium where the port is. By virtue of periodic boundary conditions, implemented using Floquet periodicity, an infinite array of GST cubes in the x-y plane is simulated. Throughout the numerical study of the interaction between this metamaterial design, based on an array of identical, evenly spaced GST blocks, and electromagnetic radiation, several parameters have been swept, namely those characterising geometrical features, such as period P, GST film thickness t and gap width between neighbouring GST blocks w; the structural phase of the GST film has also been changed. The impact of these modifications on transmission, reflection and absorption spectra, as well as on the field maps portraying the spatial profile of the electric and magnetic fields, are evaluated in the following. All simulations results up to Figure 15 concern amorphous GST.

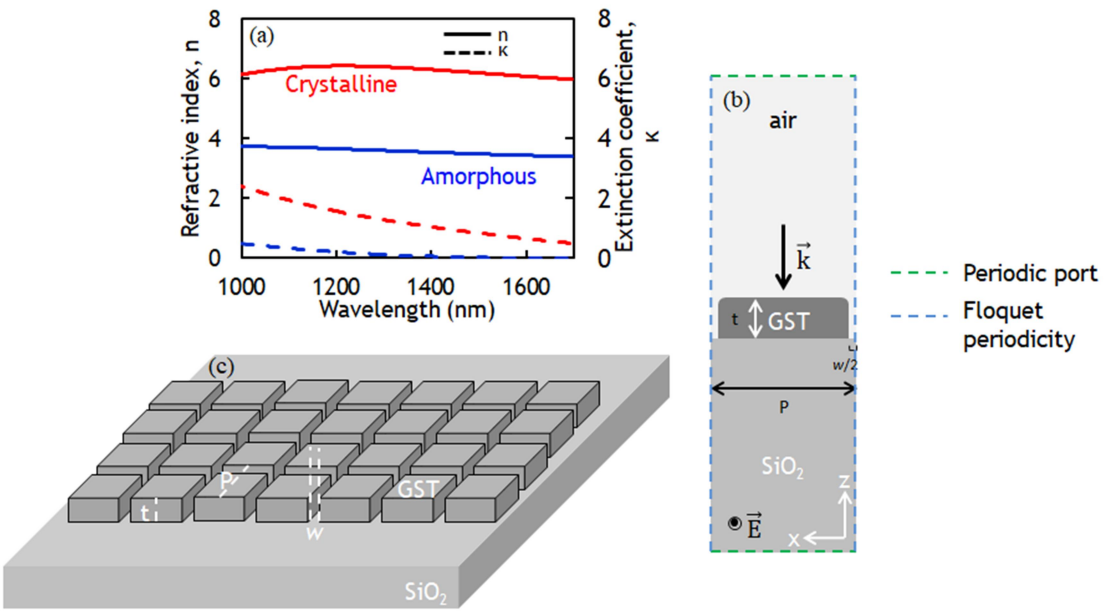


Figure 11– (a) Dispersion curves for the refractive index (n) and the extinction coefficient (κ) of GST in the amorphous (blue) and crystalline (red) phases; (b) 2D schematic diagram showing the COMSOL-modelled geometry, materials and configuration of the interaction between light and metamaterial structure; periodic input and output ports are considered, along with periodic boundary conditions; (c) 3D schematic representation of the periodic GST block array;

4.2.1. Spectral tuning via adjustment of the geometrical parameters

Transmission (T), reflection (R) and absorption (calculated as A = 1 – T – R) spectra from arrays with w = 80 nm, t = 190 nm and period taking three different values P = 900, 950 and 1000 nm are numerically obtained and depicted in Figure 12a, b. These metasurfaces show resonances with spectral positions dependent upon the assigned period: as longer periods are considered, all resonant features shift to longer wavelengths. As mentioned in Section 3, losses in GST reduce significantly as a result of shifting the operation wavelength band further into the near-infrared region. The simulated results do manifest a tendency to obtaining sharper resonances, associated to higher Q-factors ($Q = \lambda_r/\Delta\lambda$, where λ_r is the resonant wavelength and $\Delta\lambda$ is the spectral width at half-maximum), linked to longer array periods: varying the period from 900 nm to 1000 nm brings with it an increase in Q-factor from 25 up to 59; absorption is estimated to fall from a value at resonance around 27%, for P = 900 nm, down to an almost negligible level for P = 1000 nm. The field maps in Figure 12c-e, all along a vertical plane cutting through the GST block and containing the direction of light propagation, illustrate how the electric field norm morphs as a consequence of a change in the periodicity of the array:

longer periods favour tighter field concentration in the gaps between adjacent GST blocks. The two-lobe shape, hinting at the non-fundamental nature of this mode, is preserved throughout.

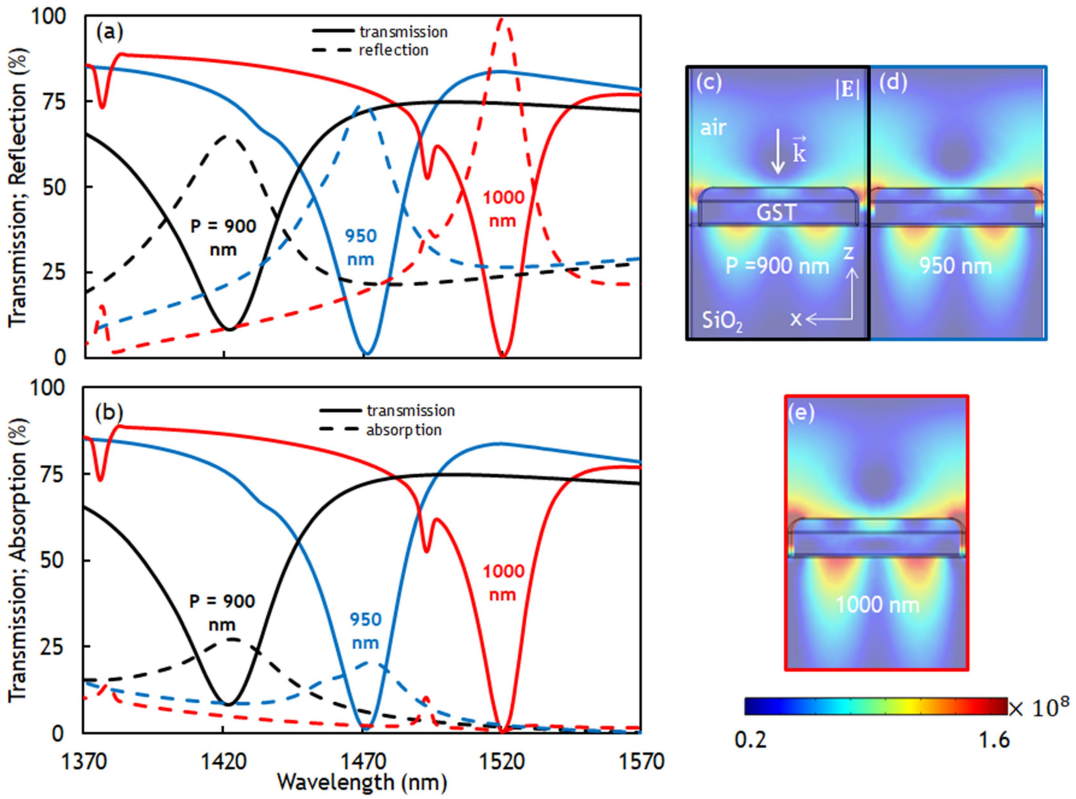


Figure 12 – Simulated (a) transmission, reflection and (b) transmission, absorption spectra for three different periods (900, 950, 1000 nm); (c)-(e) corresponding field maps displaying the norm of the electric field at resonance; w = 80 nm, t = 190 nm.

The nature of the mode supported by this structure can be further clarified by inspecting the field profile of other electric field components and that of the magnetic field norm, as presented in Figure 13. As evidenced by Figure 12c-e and corroborated by Figure 13a, the electric field norm funnels through the gap between neighbouring blocks, with little light intensity confined inside the GST layer. The z-component (Figure 13b) adds information regarding the dipolar nature of the resonant mode, exhibiting two lobes of negative and positive electric field amplitude. Again, as seen in the case of the norm of the electric field, most of the light is found outside the block (either in the silica substrate or constrained to the air/GST interface), with reduced light confinement within the GST block. Figure 13c reveals the x-component of the electric field to be responsible for the considerable field localisation near the gaps. Contrary to the electric field, the magnetic field is well confined inside the GST block, with typical amplitudes two orders of magnitude lower than those of the electric field norm.

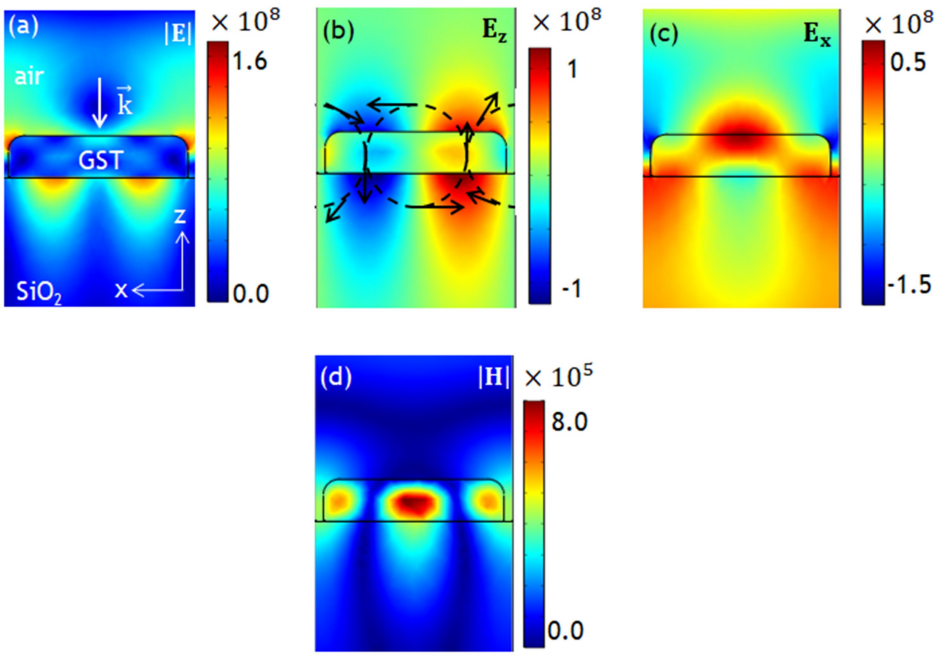


Figure 13 - Field maps displaying (a) the norm, (b) z-component and (c) x-component of the electric field; (d) profile showing the norm of the magnetic field; All field maps are taken at resonance; P = 900 nm, w = 80 nm, t = 190 nm.

Spectral tuning based on adjusting other geometrical parameters besides the period has also been investigated. The gap width between adjacent GST blocks is modified, keeping the period constant, and the resulting spectral changes are depicted in Figure 14. Wider gaps bear as a consequence a blueshift of all resonances: widening the gap while preserving the period translates into shorter GST blocks (along x and y directions), which is equivalent to reducing the effective refractive index perceived by light as it travels through the metamaterial, shifting all fringes to shorter wavelengths. Absorption levels tend to remain approximately the same throughout this parameter sweep, with only a slight decrease of the resonant value as wider gaps are simulated. Figure 14c-f display a qualitatively unchanged electric field norm profile except for enhanced field localisation in the gaps when their width decreases.

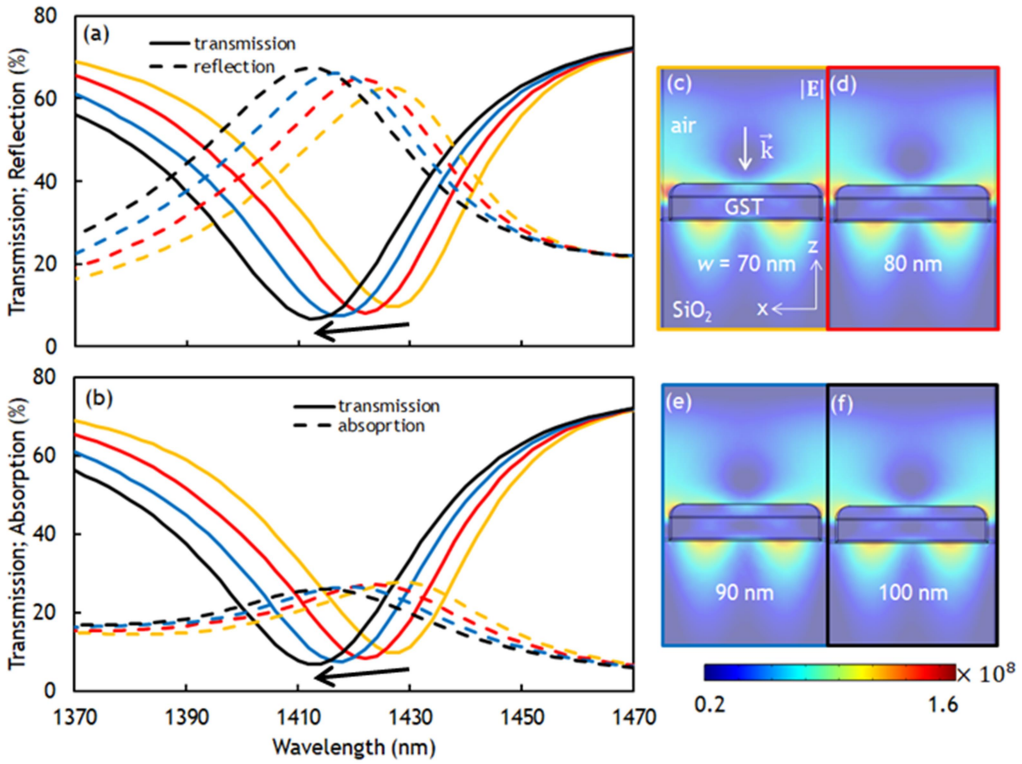


Figure 14 - Simulated (a) transmission, reflection and (b) transmission, absorption spectra for four different gap widths (70, 80, 90, 100 nm); (c)-(f) corresponding field maps displaying the norm of the electric field at resonance; P = 900 nm, t = 190 nm. Arrows show how the resonances shift as a result of widening the gaps.

Film thickness is another relevant geometrical parameter. The modifications in the spectral position of the transmission, reflection and absorption features take place depending on whether the film thickness increases or decreases: thicker films shift the resonances to longer wavelengths. Absorption levels decrease as thicker films are considered. This result is at odds with the line of reasoning adopted so far, based on primarily explaining variations in the absorption values by simply bearing in mind the spectral dependence of the extinction coefficient of GST. By examining the field maps in Figure 15c-f, one can see that enhanced field localisation occurs when thicker films are simulated, meaning the field is gradually less contained in the GST block and more confined to the gaps. As a result, light will funnel more efficiently through the gaps without being trapped inside the GST block, and less absorption takes place, even though a higher effective extinction coefficient is expected under these circumstances (thicker films, resulting in redshifted resonances). To make this point clearer, maybe thinking of the overall absorption as a variable depending both on the extinction coefficient and modal overlap with the GST block helps. In this particular case, a smaller modal overlap dominates over the higher extinction coefficient in determining the way thicker GST films alter absorption.

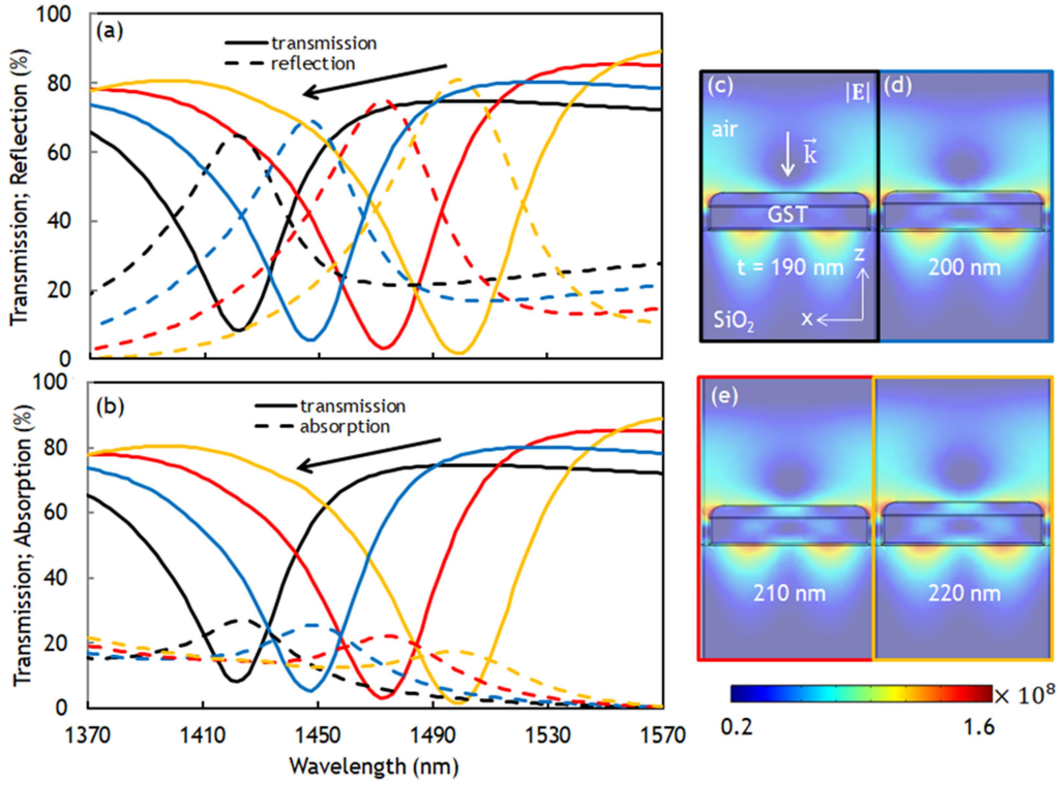


Figure 15 - Simulated (a) transmission, reflection and (b) transmission, absorption spectra for four different film thicknesses (190, 200, 210, 220 nm); (c)-(f) corresponding field maps displaying the norm of the electric field at resonance; P = 900 nm, w = 80 nm. Arrows show how the resonances shift as a result of simulating thinner GST films.

4.2.2. Assessing spectral modifications arising from changes in the optical properties of the GST layer

An equally important task is estimating how changes in the real part of the refractive index (n) and in the extinction coefficient (κ) impact on light interaction with these structures, helping predict the expected alterations in the transmission, reflection and absorption spectra. A first approach consists in replacing the dispersive GST with a non-dispersive dielectric material, with variable n and κ. The impact of varying n is studied by choosing a moderately lossy (κ = 0.01) dielectric material with fixed n for all wavelengths, which is varied from 3.5 (akin to amorphous GST, without dispersion) up to 4.0. Figure 16 features the transmission and reflection spectra, alongside field maps exhibiting the electric field norm. As expected, a dielectric block with higher n introduces redshifted resonances in the simulated spectra. In addition, the Q-factor decreases, from 36 down to 23, and reduced field confinement in the gaps takes place. The field maps in Figure 16c-g corroborate these observations.

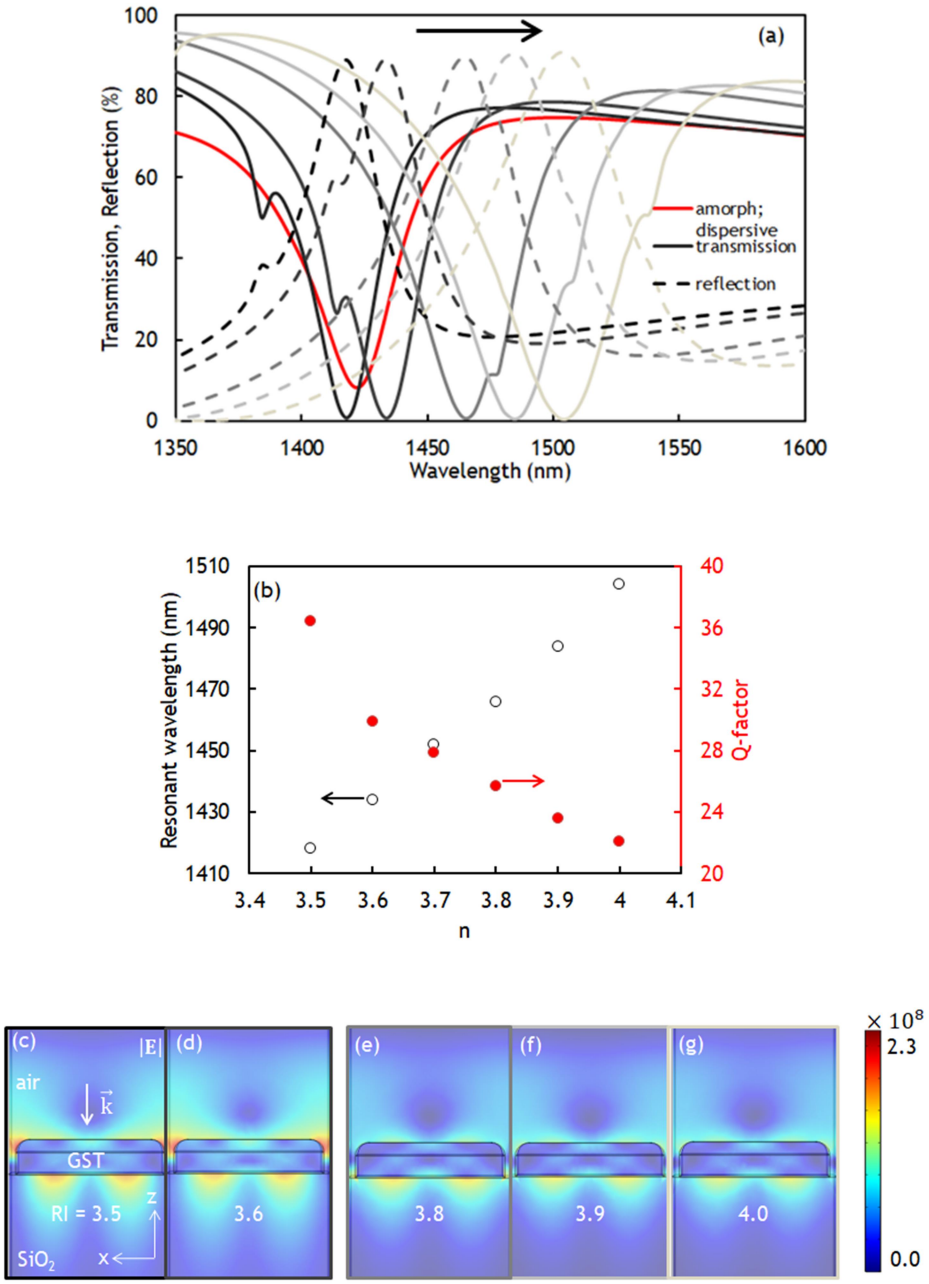


Figure 16 – Simulated (a) transmission, reflection spectra for five different values of the refractive index n (3.5, 3.6, 3.8, 3.9, 4.0) in the case of a non-dispersive dielectric material with extinction coefficient κ = 0.01; red line shows transmission for dispersive amorphous GST for comparison with a non-dispersive dielectric material (κ = 0.01) with n = 3.5; (b) resonant wavelength and Q-factor as a function of RI; (c)-(g) corresponding field maps displaying the norm of the electric field at resonance; arrow shows how the resonances shift as a result of increasing n; P = 900 nm, w = 80 nm, t = 190 nm.

Playing around with the loss in the GST film, as dictated by the value of κ, also enables controlling the characteristics of the resonant features. As expected, given the intimate connection between κ and absorption in the GST film, as κ increases from 0.01 up to 0.4 (n = 4.0), the absorption level goes from 8% up to around 50%. The Q-factor of transmission and

reflection resonant features gradually drops down from 23 (for κ = 0.01). The field maps in Figure 17c-g confirm these considerations, portraying a progressively less intense electric field as κ increases. The simulation results obtained considering a non-dispersive dielectric material with n = 4.0 and κ = 0.4 should constitute a reasonable numerical prediction of light interaction with a partially crystallised GST film.

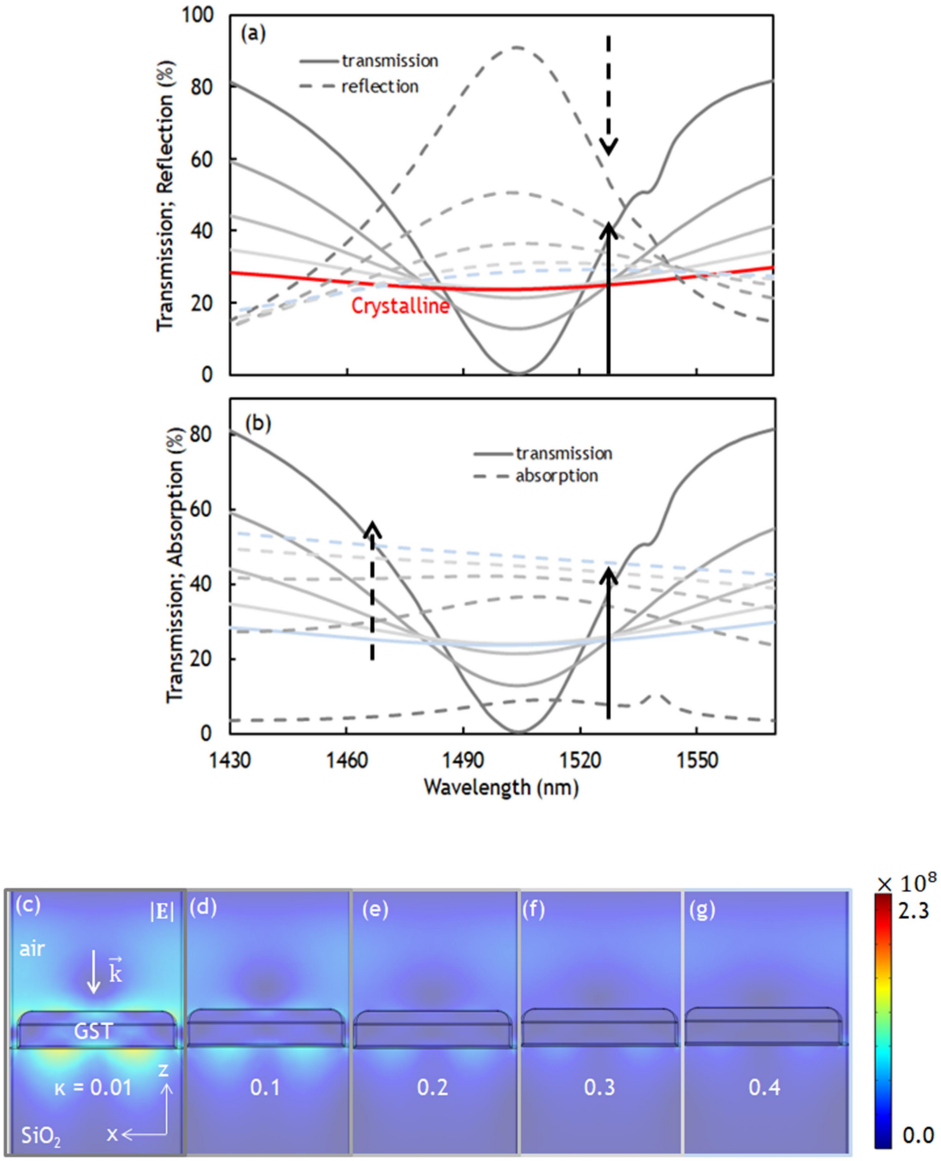


Figure 17 – Simulated (a) transmission, reflection and (b) transmission, absorption spectra for five different values of the extinction coefficient κ (0.01, 0.1, 0.2, 0.3, 0.4) in the case of a non-dispersive dielectric material with refractive index n = 4.0; red line shows transmission for a non-dispersive dielectric material with κ = 0.4 and n = 4.0 (akin to a relatively well crystallised GST film); (c)-(g) corresponding field maps displaying the norm of the electric field at resonance; arrows show how the resonance evolves as a result of increasing n; P = 900 nm; w = 80 nm, t = 190 nm.

A more elegant way of assessing transmission and reflection modulation upon crystallisation consists in considering, instead of a non-dispersive dielectric material with sensibly chosen n and κ, a dispersive material with optical properties derived from the ellipsometrically measured dispersion curves of n and κ in amorphous and crystalline GST shown in Figure 11a. The optical properties of partially crystallised GST can be calculated, for a given degree of crystallisation η, as a weighted average between their values in the amorphous and crystalline states:

$$\begin{aligned} n_\eta(\lambda) &= (1-\eta)n_{amorphous}(\lambda) + \eta n_{crystallised}(\lambda) \\ \kappa_\eta(\lambda) &= (1-\eta)\kappa_{amorphous}(\lambda) + \eta \kappa_{crystallised}(\lambda) \end{aligned} \quad (1)$$

The dispersion curves are plotted in Figure 18. As expected, both n and κ increase slightly upon partial crystallisation in steps of 10%, while retaining the shape of the dispersion curve for the amorphous state.

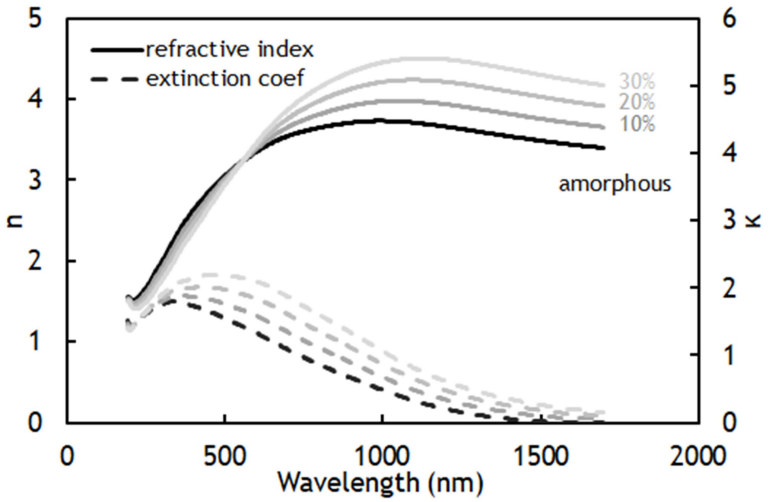


Figure 18 - Dispersion spectra of the refractive index n and extinction coefficient κ for the amorphous phase and different degrees of crystallisation (10%, 20% and 30%).

Tailoring the transmission and reflection properties of the proposed metasurface can be achieved by promoting partial crystallisation of the GST layer, as numerically estimated and presented in Figure 19. In keeping with the findings for a non-dispersive dielectric material with varying n and κ, a higher degree of crystallisation, entailing higher n and κ, redshifts the resonances and reduces the associated Q-factor. For instance, transmission resonances are shifted from 1422 nm (amorphous) to 1560 (η = 30%), while a Q-factor of 25 is rendered negligible. A degree of crystallisation η = 30% produces spectral changes similar to those registered for a non-dispersive dielectric material with n = 4.2 and κ = 0.4.

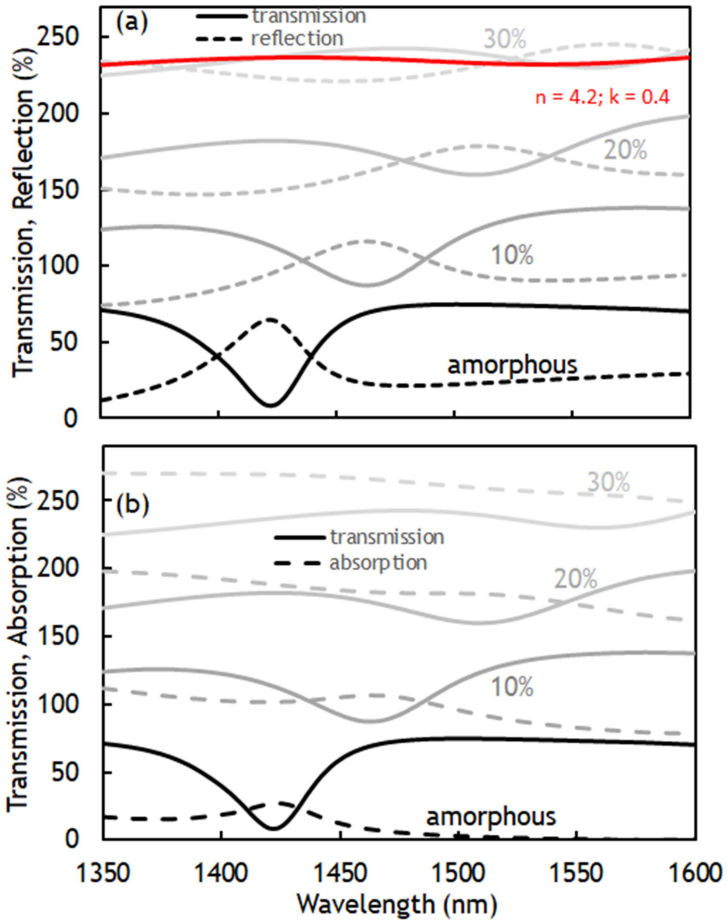


Figure 19 - Simulated (a) transmission, reflection and (b) transmission, absorption spectra for the amorphous phase and different degrees of crystallisation (10%, 20% and 30%); red curve shows transmission for a non-dispersive dielectric material with n = 4.2 and κ = 0.4; P = 900 nm, w = 80 nm, t = 190 nm.

Assessing phase modulation and group delay dispersion (GDD) for different metasurface geometries is of undeniable relevance, bearing in mind the technological applications in which wave-front manipulation and dispersion control are required[162-164]. COMSOL, besides calculating transmission and reflection from the designed metamaterial, also finds phase difference between input and output waves. GDD can be obtained through the group velocity dispersion (GVD)[165]:

$$\mathrm{GVD} = \frac{\mathrm{d}^2\mathrm{k}}{\mathrm{d}\omega^2} \tag{2}$$

Expanding this second derivative,

$$\frac{\mathrm{d}^2\mathrm{k}}{\mathrm{d}\omega^2} = \frac{\mathrm{d}}{\mathrm{d}\omega}\left[\frac{\mathrm{dk}}{\mathrm{d}\lambda}\left(\frac{\mathrm{d}\lambda}{\mathrm{d}\omega}\right)\right] = \frac{\mathrm{dk}}{\mathrm{d}\lambda}\left(\frac{\mathrm{d}^2\lambda}{\mathrm{d}\omega^2}\right) + \left(\frac{\mathrm{d}\lambda}{\mathrm{d}\omega}\right)\frac{\mathrm{d}}{\mathrm{d}\omega}\left[\frac{\mathrm{dk}}{\mathrm{d}\lambda}\right] \tag{3}$$

Writing $c = \omega\lambda/2\pi$,

$$\frac{d\lambda}{d\omega} = -\frac{\lambda^2}{2\pi c} \tag{4}$$

$$\frac{d^2\lambda}{d\omega^2} = \frac{\lambda^3}{2(\pi c)^2} \tag{5}$$

$$\frac{d}{d\omega} = -\frac{\lambda^2}{2\pi c}\frac{d}{d\lambda} \tag{6}$$

Recasting Eq. (3) in a more compact form yields

$$GVD = \frac{d^2k}{d\omega^2} = \frac{\lambda^3}{2(\pi c)^2}\left[\frac{dk}{d\lambda} + \frac{\lambda}{2}\frac{d^2k}{d\lambda^2}\right]\left[\frac{s^2}{m}\right] \tag{7}$$

As an electromagnetic wave propagates along a given length l, it accumulates phase φ given by

$$\varphi(\lambda) = k(\lambda)l \tag{8}$$

The GDD is calculated by multiplying the GVD by the propagation length l, thus providing a value that corresponds to the dispersion introduced by a given device as opposed to the dispersion of a given material:

$$GDD = GVD \times l = \frac{\lambda^3}{2(\pi c)^2}\left[\frac{d\varphi}{d\lambda} + \frac{\lambda}{2}\frac{d^2\varphi}{d\lambda^2}\right][s^2] \tag{9}$$

Figure 20 features the spectral dependencies of the phase and GDD for the three different periods considered so far (900, 950 and 1000 nm). Longer periods shift the resonant phase modulation and associated GDD behaviour to longer wavelengths. The peaks both in phase modulation and GDD occur at the same spectral locations as the transmission resonances, hinting at the close connection between them. Higher Q-factors tied with longer periods (owing to lower losses in GST) enable more pronounced phase modulation and higher GDD maximum values. In addition, positive and negative GDD values are registered near the resonances, which make normal and anomalous dispersion corrections possible, respectively. Maximum GDD values are improved from 0.015 ps^2 up to 0.13 ps^2, upon changing P from 900 to 1000 nm. Such optical properties have vast technological implications, with potential for application in dispersion compensation structures. This enticing electromagnetic behaviour, condensed into,

for instance, a fibre-tip-integrated light modulator of reduced dimensions (t ~ 200 nm; $\lambda/t \sim 8$), makes it possible for dispersion compensation that would require a sizeable stretch of singlemode optical fibre (~ 1 m of fibre, considering a dispersion parameter of 20 ps/(nm.km) and an operation wavelength of 1550 nm) to be performed within a fraction of the operation wavelength.

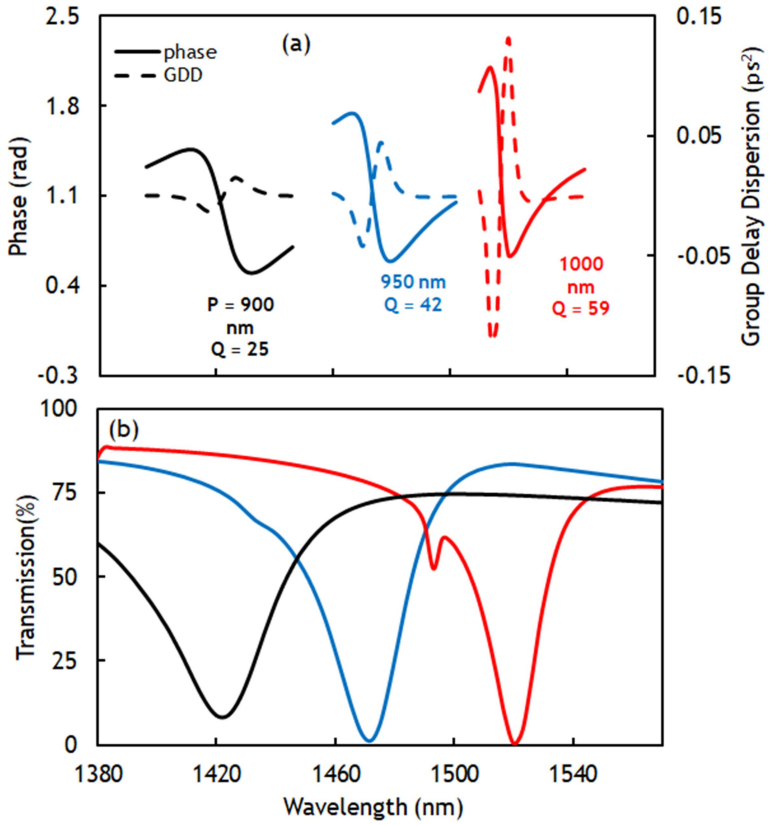


Figure 20 – (a) Simulated phase and group delay dispersion (GDD) for three different periods (900, 950, 1000 nm); (b) corresponding transmission curves; w = 80 nm, t = 190 nm.

Structural phase transitions also promote variations in the magnitude of the phase modulation and GDD. As Figure 21 exemplifies, by changing the phase of the GST layer in a structure with P = 900 nm, the considerable phase modulation observed in the amorphous state is rendered almost imperceptible after crystallisation (non-dispersive dielectric material with n = 4.0 and κ = 0.4). Consequently, the GDD collapses, being reduced from a maximum absolute value of 0.015 ps^2 in the amorphous state down to 0.001 ps^2 upon crystallisation. Hence, considerable dispersion compensation is attainable using such structures while GST is kept in the amorphous state, while this capability can be turned on/off by resorting to induced structural-phase transitions.

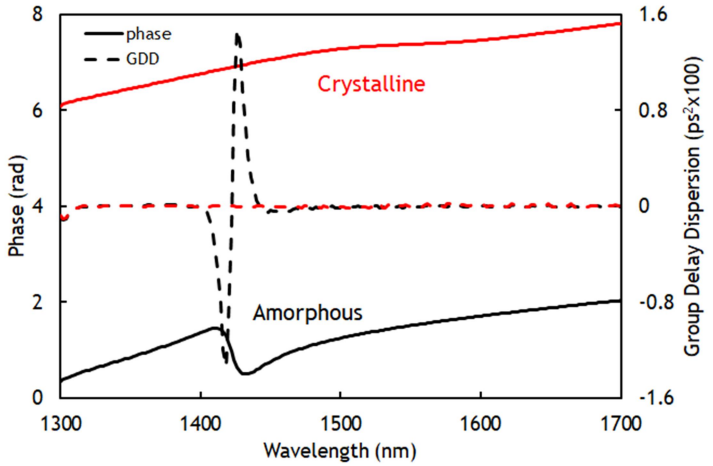


Figure 21 – Simulated phase and group delay dispersion (GDD) for both amorphous (black) and crystalline (red) states; P = 900 nm, w = 80 nm, t = 190 nm.

Finer tuning of the dispersion compensation performance is also available, besides via changing the period as already demonstrated, through controlled crystallisation. Figure 22 makes it clear that adjusting the spectral position and the value of the maximum GDD is possible by inducing a controlled degree of crystallisation. Modulation of the maximum GDD is given by $\left(\mathrm{GDD}_{\mathrm{amorph,\ max}}/\mathrm{GDD}_{30\%,\mathrm{max}}\right) = 1.48 \times 10^{-26}/7.98 \times 10^{-28} = 18.5$.

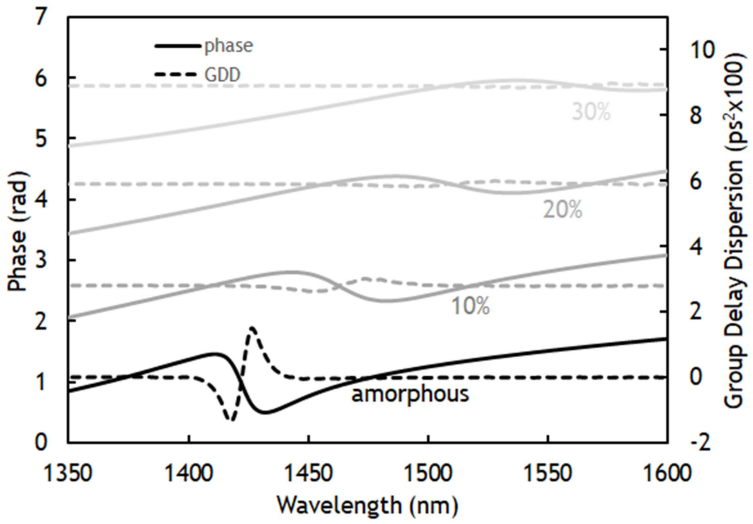


Figure 22 - Simulated phase and group delay dispersion (GDD) for the amorphous state and different degrees of crystallisation (10%, 20%, 30%); P = 900 nm, w = 80 nm, t = 190 nm.

Extracting phase directly from transmission and reflection measurements can prove helpful, if not in the context of numerical simulations where software like COMSOL can retrieve it quite efficient and accurately, at least in an experimental circumstance in which

phase-sensitive measurements are not feasible. Kramers-Kronig relations relate the real and imaginary parts of the refractive index[165]. Through transmission and reflection measurements, performed experimentally, absorption spectra can be retrieved. Absorption α and extinction coefficient κ are related through

$$\alpha(\lambda) = a\frac{2\pi}{\lambda}\kappa(\lambda) \tag{10}$$

where a is the absorptivity. The real part of the refractive index n can then be written as

$$n(\omega) = 1 + \frac{2}{\pi}\int \frac{\Omega\kappa(\Omega)}{\Omega^2 - \omega^2}d\Omega \tag{11}$$

being ω and Ω frequencies. Recalling that $c = \omega\lambda/2\pi$,

$$n(\lambda) = 1 + \frac{2}{\pi}\int \frac{\Lambda^{-1}\kappa(\Lambda)}{1 - \left(\frac{\Lambda}{\lambda}\right)^2}d\Lambda \tag{12}$$

being λ and Λ wavelentgths. Finally, n can be expressed as a function of the absorption α as

$$n(\lambda) = 1 + \frac{1}{a\pi^2}\int \frac{\alpha(\Lambda)}{1 - \left(\frac{\Lambda}{\lambda}\right)^2}d\Lambda \tag{13}$$

Recovering Eq. (8) and combining it with Eq. (13) gives

$$\varphi(\lambda) = 2\pi\frac{n(\lambda)}{\lambda}l = \frac{2\pi}{\lambda}\left[1 + \frac{1}{a\pi^2}\int \frac{\alpha(\Lambda)}{1 - \left(\frac{\Lambda}{\lambda}\right)^2}d\Lambda\right]l \tag{14}$$

The absorptivity a depends on the material and specific metamaterial design, but also on the film thickness t. One can assume a direct proportionality with a proportionality constant γ

$$a = \gamma l \tag{15}$$

The total phase accumulated, taking into account propagation in air followed by propagation in silica is given by

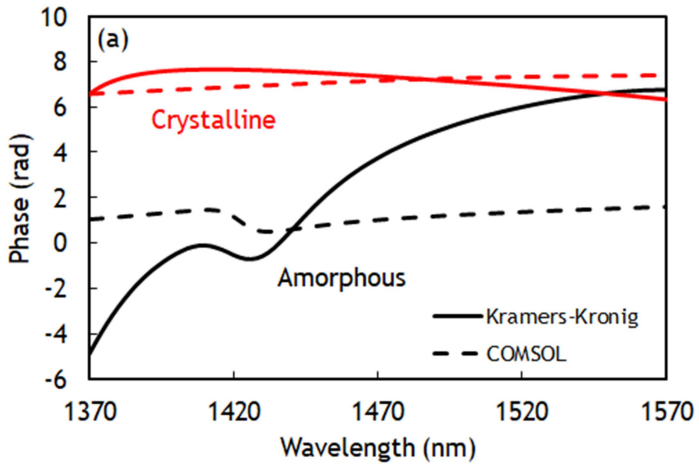
$$\varphi_{TOTAL}(\lambda) = \varphi_{air}(\lambda) + \varphi(\lambda) + \varphi_{silica}(\lambda) = \frac{2\pi}{\lambda}(l_{air} + n_{silica}l_{silica}) + \varphi(\lambda) \tag{16}$$

where the final form of the phase introduced by the metasurface is

$$\varphi(\lambda) = 2\pi\frac{n(\lambda)}{\lambda}l = \left[\frac{2\pi}{\lambda}l + \frac{2}{\gamma\pi\lambda}\int \frac{\alpha(\Lambda)}{1-\left(\frac{\Lambda}{\lambda}\right)^2}d\Lambda\right] \quad (17)$$

Since n(λ) is calculated in the same spectral range as α(Λ), a singularity will arise when Λ= λ. In order to avoid this, a slightly shifted spectral domain of n(λ) is considered. For instance, when Λ = λ = 1400 nm, the new (shifted) λ will be 1400.4 nm, and no singularity will have to be dealt with.

Typical values of γ can be estimated for both the amorphous and crystalline phases, taking into account simulated absorption and measured extinction coefficient, as well as film thickness. In the following, it is assumed that $\gamma_{amorphous} = 0.3$ and $\gamma_{crystalline} = 0.04$. A comparison between phase modulation calculated via COMSOL and resorting to the Kramers-Kronig framework, both for a structure with P = 900 nm, w = 80 nm, t = 190 nm, is carried out and graphically presented in Figure 23. The resonant feature, conspicuous in the amorphous state, is reasonably well replicated by the Kramers-Kronig derivation. In the crystalline state, both approaches reveal that little phase modulation is imparted by the metastructure to the propagating electromagnetic wave. GDD results are also similar, both treatments yielding normal and anomalous dispersion near the resonance and maximum values differing less than 5%[1], in the amorphous phase. Upon crystallisation, both give marginal dispersion compensation.



[1] Deviation (%) $= \frac{|GDD_{máx,KK} - GD\ _{máx,COMSOL}|}{GDD_{máx,KK}+GDD_{máx,COMSOL}} \times 100\% = \frac{|0.0165-0.015|}{0.0165+0.015} \times 100\% \sim 4.76\%$

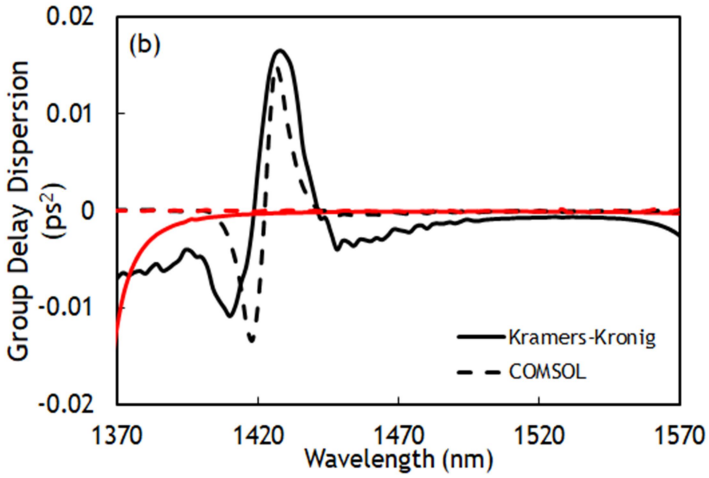


Figure 23 - Graphical comparison between (a) phase and (b) group delay dispersion (GDD) derived using Kramers-Kronig or COMSOL for both structural states; P = 900 nm, w = 80 nm, t = 190 nm.

4.3. Experimental results

4.3.1. GST blocks on flat glass substrates

Before addressing fibre-integrated arrays of GST blocks, a preliminary investigation was conducted to determine the transmission and reflection characteristics of these metasurfaces fabricated on flat glass substrates, both in the amorphous and crystalline states.

To this end, GST films with a thickness t of 200 nm were deposited on glass flat substrates by RF sputtering (Kurt J. Lesker Nano 38). A base pressure of 2×10^{-4} mbar is achieved prior to deposition and high-purity argon is used as the sputtering gas (70 ccpm to strike, 37 ccpm to maintain plasma). The substrates are held within 10 K of room temperature on a rotating platen 150 mm from the target to produce low-stress amorphous as-deposited films. Sub-wavelength period (i.e. non-diffractive) cubes, with a fixed linewidth w~80 nm and periods P ranging from 900 to 1100 nm, each covering an area of approximately 20 μm × 20 μm, were etched through the GST layer by focused ion beam (FIB) milling (FEI Helios NanoLab 600), as illustrated in Figure 24a. The normal-incidence reflection and transmission characteristics of these structures were subsequently measured using a microspectrophotometer (CRAIC QDI2010) with a sampling domain size of 15 μm × 15 μm. Crystallisation of the GST layer was induced using a CW laser operating in the visible range ($\lambda_{operation}$ = 532 nm) in order to maximise absorption in the GST film, given its high extinction coefficient in this spectral region. The intensity delivered onto the GST film is ~ 2 mW/μm^2.

Consequently, temperature in the film rises via Joule heating and crystallisation takes place. The sample is mounted on a computer-controlled translation stage, allowing control over its translation speed and raster area. This way, the beam scans a large area, potentially much larger than its spot size (typically $\sim 3-4$ μm), covering the whole metamaterial array. Figure 24b features a transmission optical microscope photograph of the entire ensemble of arrays, exhibiting noticeable changes in the GST film as a result of laser-induced thermal annealing: crystallised areas appear darker as a result of higher absorption leading the reduced light transmission.

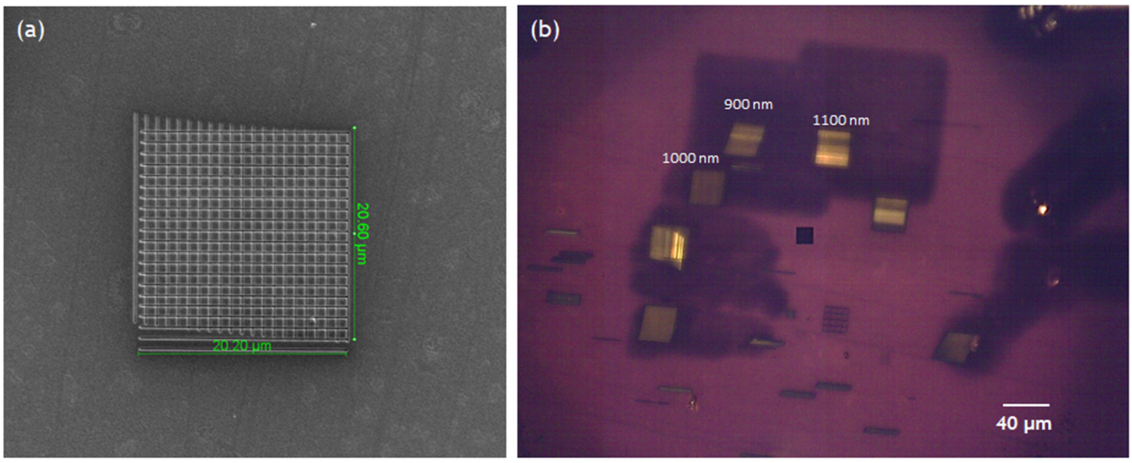


Figure 24 - (a) SEM picture of an array with period 1000 nm; (b) optical microscope picture of all the arrays (transmission) after crystallisation using a CW laser: dark areas (low transmission) correspond to crystallised areas whereas brighter areas (higher transmission) correspond to amorphous GST.

Transmission, reflection and absorption measurements are shown in Figure 25. As predicted by our numerical simulations, longer periods end up redshifting all the resonant features. Moving from an array with P = 900 nm to one with P = 1100 nm shifts the transmission resonance from 1400 nm up to 1646 nm, meaning appropriately choosing the value of this geometrical parameter allows placing the resonance anywhere around the technologically pivotal 1550-nm band, potentially covering a wide region in the near-infrared. Furthermore, good agreement between the numerically predicted and experimentally measured spectral location of the resonances is achieved. Features in the reflection spectra are not as sharp as transmission resonances. Absorption levels go up near the resonant wavelengths. For instance, for P = 1100 nm, absorption rises from a base level (off-resonance) around 20% (@ 1520 nm) to approximately 30% (@ resonance). At longer wavelengths (> 1700 nm), unexpected features are introduced. These are attributable to off-normal incidence: the CRAIC source has a non-zero numerical aperture (N.A.), meaning the samples are illuminated by a cone of light rather than by a collimated, near-paraxial beam. In the simulation results presented in this section, light

incidence is assumed to be normal, neglecting all other contributions. This ends up masking contribution from incidence at higher angles, which are present in experimental circumstances. Considering non-normal incidence at low angles (~ 5 deg) produces simulation results that already feature two resonances (Appendix A).

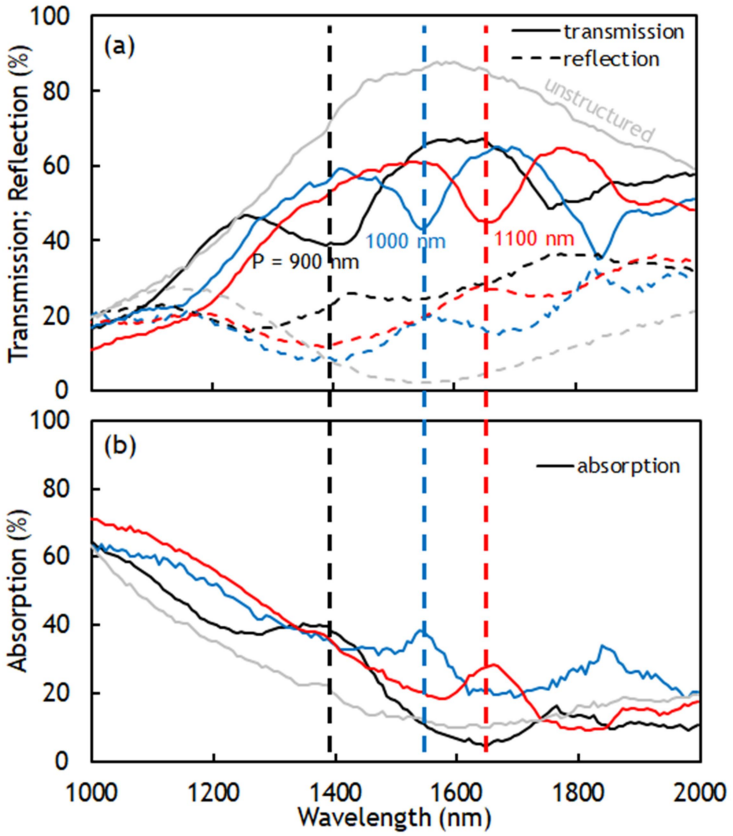


Figure 25 - CRAIC-measured (a) transmission, reflection and (b) absorption spectra for different array periods: 900, 1000 and 1100 nm; w = 80 nm, t = 200 nm.

Alterations due to light-induced crystallisation are summarised in Figure 26-28. In good accord with the expected redshift associated with the increase in the real part of the refractive index and the broadening of the resonances linked to higher extinction coefficient of the crystalline phase, all spectral features move to longer wavelengths and become slightly broader as a result of the promoted phase transition. Less pronounced shifts and attenuation than what would have been expected upon full crystallisation, as per simulation results, can be explained by the fact that laser intensity was short of the required value to fully crystallise the GST layer; in addition, Ga implantation during FIB fabrication changes the way structured GST responds to light-induced thermal annealing. Transmission and reflection modulation ratios are plotted for periods of 900 and 1100 nm, calculated as the ratio between transmission and reflection in the amorphous and crystalline phases. The spectral positions of the modulation ratio maxima coincide with that of the shifted resonances, where the contrast between transmission and

reflection is highest. Maximum transmission ratios are 3.46 dB and 1.88 dB, at 1530 nm and 1735 nm, for P = 900 nm and P = 1100 nm, respectively.

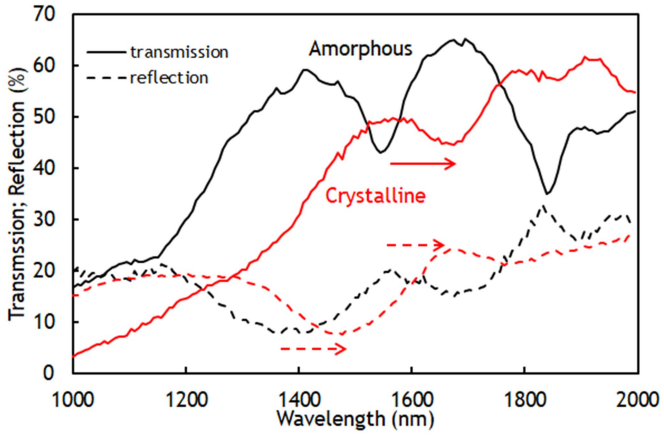


Figure 26 - Craic-measured transmission and reflection spectra for the amorphous and crystalline phases. Arrows show how the fringes shift as a result of crystallisation; P = 1000 nm, w = 80 nm, t = 200 nm.

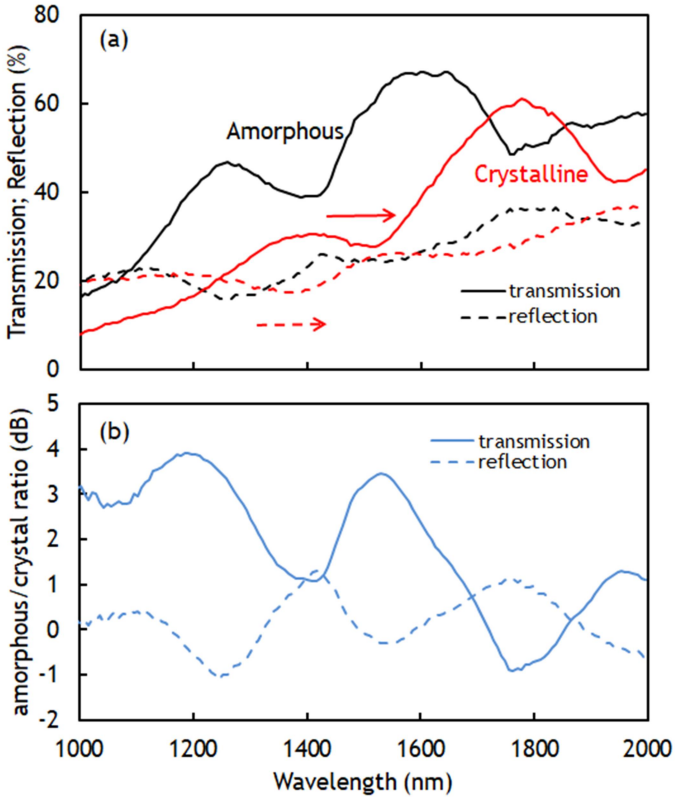


Figure 27 - (a) Craic-measured transmission and reflection spectra for the amorphous and crystalline phases; arrows show how the fringes shift as a result of crystallisation; (b) corresponding transmission and reflection ratios; P = 900 nm, w = 80 nm, t = 200 nm.

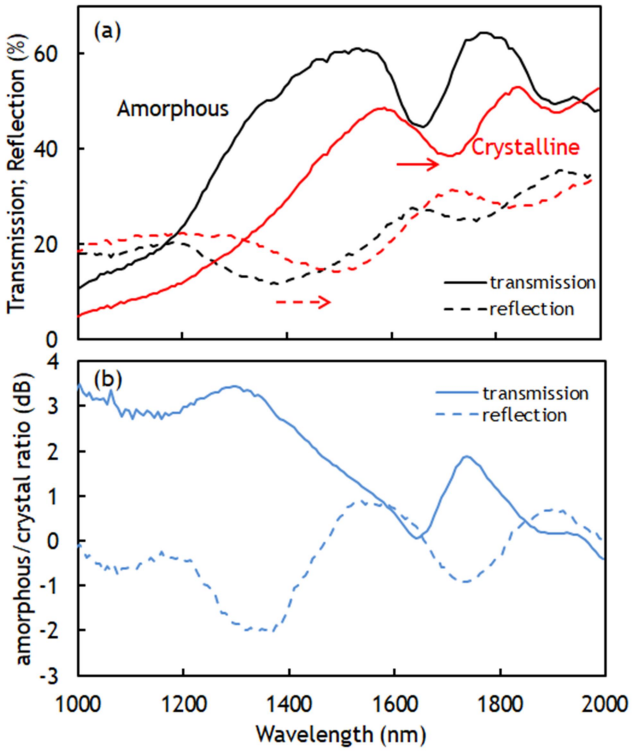


Figure 28 - (a) Craic-measured transmission and reflection spectra for the amorphous and crystalline phases; arrows show how the fringes shift as a result of crystallisation; (b) corresponding transmission and reflection ratios; P = 1100 nm, *w* = 80 nm, t = 200 nm.

4.3.2. Fibre-integrated metasurfaces based on arrays of GST blocks

The next step, envisioning a fibre-integrated intensity switch based on the proposed GST metasurface, is coming up with a suitable optical fibre platform where a thin film could be adequately grown, ensuring, simultaneously, that good interaction between the metamaterial and light guided by the fibre takes place. This requires a flat substrate, something which could be obtained simply by cleaving a fibre tip.

GST films with thickness t = 190 nm are sputtered onto the fibre tips, using the same procedures as described for the flat glass substrates. FIB machining also replicates the process employed in the preliminary study for these devices. During processing, special care is taken to align the nanostructured area over the fibre core, ensuring experimental light measurements reflect the interaction of light with the structured medium fabricated on the tip of the fibre. A structure like the one schematically drawn in Figure 29a is thus produced. An SEM image is placed alongside to allow evaluating the good overlap between metasurface and fibre core (located in the central part of the fibre) as well as the quality of the fabricated arrays of cubes, showing well milled trenches between neighbouring GST blocks. This is achieved using an ion

current of 17 pA and a dosage of 20 pC/μm^2. Higher ion currents can damage the surface or cause it to heat up to a temperature high enough to induce crystallisation, something to be avoided as we want the films to remain in the amorphous state throughout fabrication and optical characterisation up to the point when crystallisation is to be induced in a controlled fashion. Ion-beam-induced crystallisation leads to the formation of unwanted bubbles in the GST film (Appendix B). Electron-beam-induced crystallisation can also be triggered when employing high SEM voltages[166,167], an undesirable event in the context of this fabrication process.

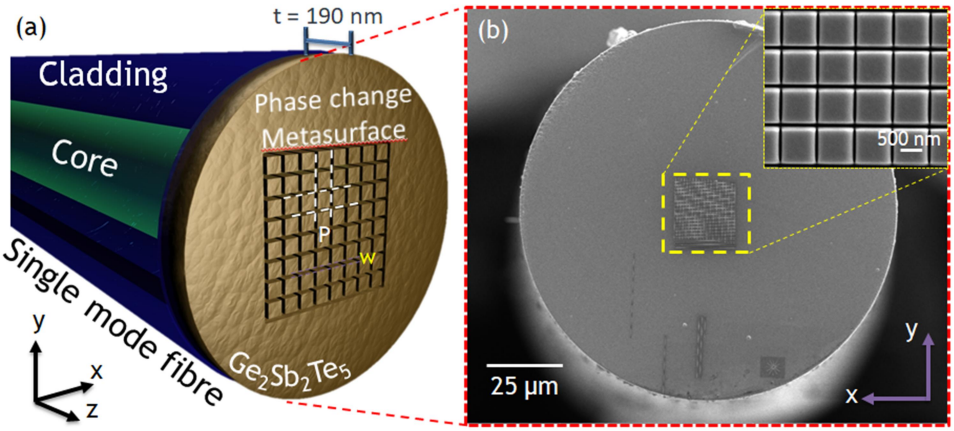


Figure 29 - (a) Schematic diagram of the proposed optical switch based on a GST phase change film deposited on an optical fibre tip; (b) SEM picture of the device; inset: close-up showing the structured area around the core in detail.

The transmission characteristics of the fiberised devices are subsequently measured by focusing near-IR light ($1000 \leq \lambda \leq 1750$ nm) from a broadband light source (Thorlabs SLS201L) onto the nanostructured fibre tip surface using a near-IR objective (Mitutoyo M Plan Apo NIR 10x; NA = 0.26) and collecting the output using an Optical Spectrum Analyser (Ando AQ-6315E). Figure 30a shows the measured transmission spectra, normalised relative to an unstructured GST-coated fibre tip, of three fibre-integrated phase change memory metasurfaces with periods 900, 950 and 1000 nm. Normalisation relative to an uncoated fibre tip (reproduced in Appendix C) gives noisier spectra with an insistent dip at long wavelengths, which vanishes when normalising relative to a coated tip, meaning this dip is introduced by the film itself rather than by the structuring of it, a feature of little importance when characterizing the spectral changes introduced by the metasurface. These fibre-integrated metasurfaces show transmission resonances with spectral positions dependent upon the period of the nanostructured cube metasurfaces. The experimental Q-factors of the transmission resonances associated with the fabricated structures peak at 34 for an array with P = 1000 nm. Figure 30b presents the

simulated transmission spectra corresponding to three different arrays of GST cubes with the same geometry as those experimentally fabricated. There is very close agreement between experimentally measured and numerically simulated transmission spectra, especially when it comes to the spectral position of the resonances. Owing to the fact that the nanostructured GST covers an area of the fibre tip surface significantly greater in size than the core, considering a simple geometry for our model consisting of a periodic array of GST cubes on top of a silica substrate with refractive index equal to that of the fibre core is found to be sufficient in establishing a good qualitative and quantitative representation of the fibre-tip-integrated experimental device characteristics. Minor discrepancies are found to be related to manufacturing imperfections, i.e. deviations from the ideal model geometry such as slight over-milling of etched lines into the substrate, and the tapered/rounded cross-sectional profile of milled lines; and to contamination/stoichiometric change in the GST layers during FIB milling, which may slightly modify the refractive index.

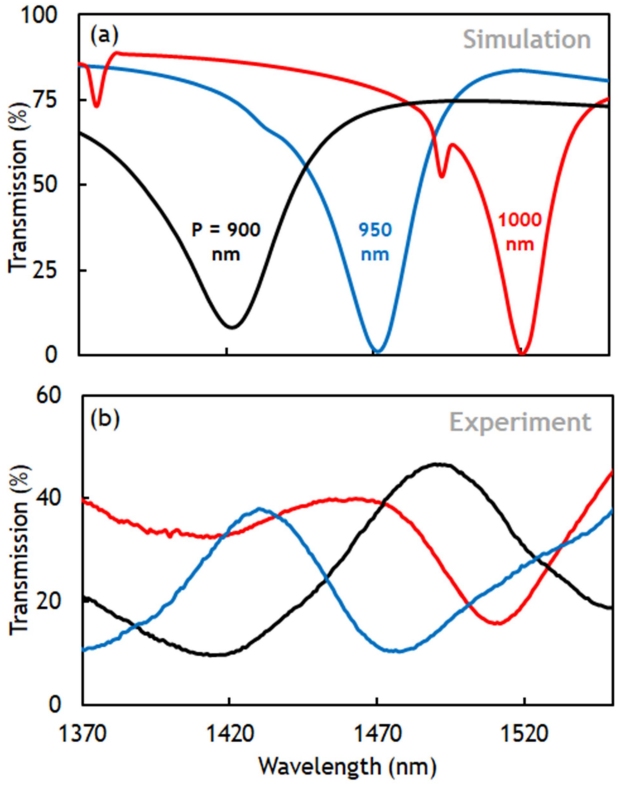


Figure 30 – (a) Simulated and (b) experimentally measured transmission spectra for arrays of GST cubes with w = 80 nm, t = 190 nm and P taking three different values: 900, 950 and 1000 nm.

Reflection measurements are also taken, resorting to the experimental configuration detailed in Section 2. Spectra are normalised relative to that of an Ag-coated fibre tip, acting as a reference mirror. The noisy profile is due to the high losses introduced by the 50/50 coupler (75% of the original signal is lost). Again, and despite the low quality of reflection

measurements, reflection features are located where they were expected to be, in the same spectral range as the corresponding transmission resonances. The same is valid for absorption.

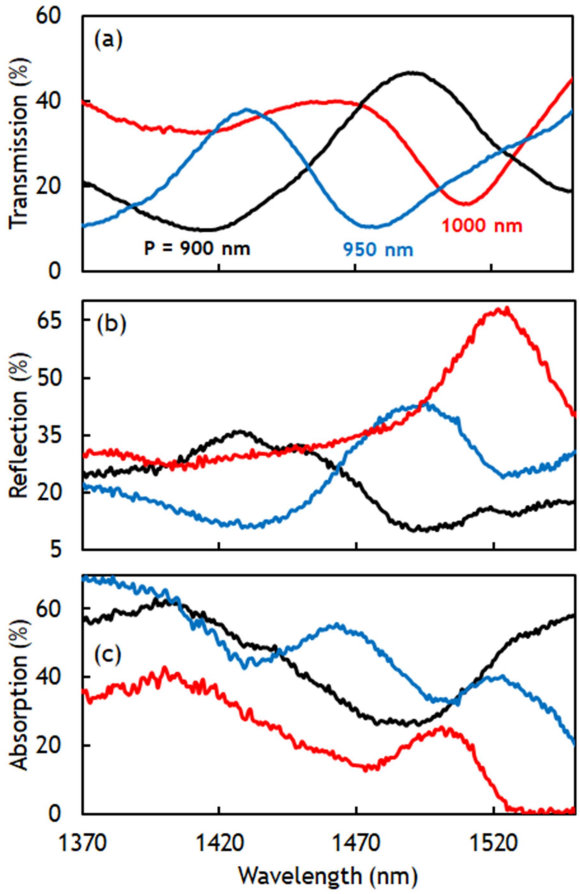


Figure 31 – Experimentally measured (a) transmission, (b) reflection and (c) absorption spectra for arrays of GST cubes with w = 80 nm, t = 190 nm and P taking three different values: 900, 950 and 1000 nm.

To evaluate the performance of our devices as a fibre-optic memory switch, the fibre-integrated metasurfaces are illuminated with light from a CW laser (Thorlabs LDC 500) operating at 1550 nm, delivering an intensity of ~ 1 mW/μm^2, which thermally anneals the surface area overlapping the fibre core, where the metasurface is fabricated. In the experimental setup designed for this purpose, as illustrated in Figure 32, laser light is amplified by an Erbium Doped Fibre Amplifier (EDFA; IPG photonics, EAD series) prior to being coupled, via an optical circulator (Thorlabs 6015-3-FC), to the fibre-integrated metadevice. This amplification guarantees the required light intensity to induce crystallisation in the phase change metasurface. Light reflected back from the metasurface on the fibre tip is detected by a powermeter (Thorlabs PM320E) and the onset of crystallisation is determined by monitoring reflected power and identifying when a pronounced increase in its value (~ 1.55), promoted by the GST phase transition, takes place. This experimental configuration, enabling light-induced crystallisation of the deposited GST layer from inside the fibre, paves the way for remotely programmable fibre-

integrated compact device configurations where single wavelength light-by-light modulation can be attained.

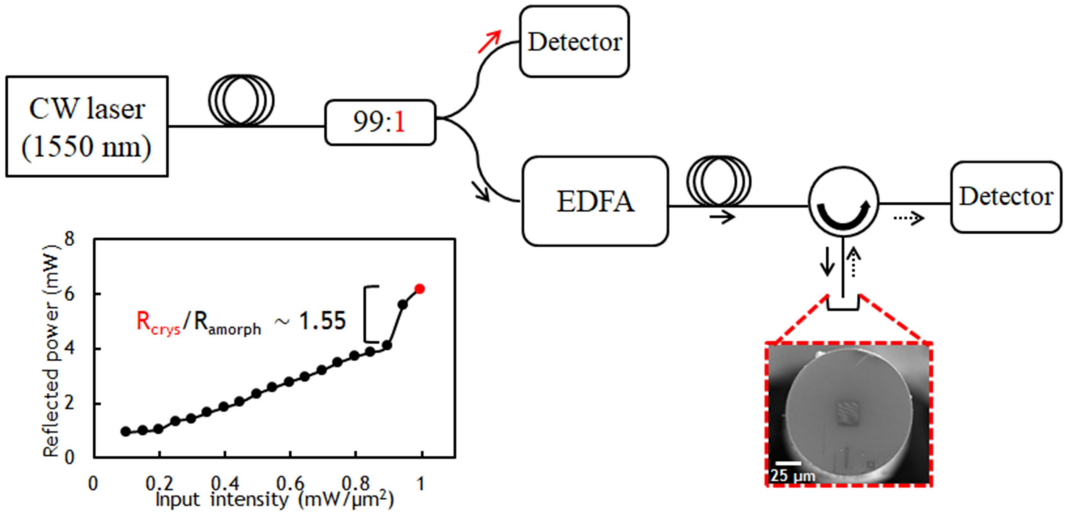


Figure 32 – Schematic diagram showing the in-fibre crystallisation setup using CW laser radiation.

The changes in the transmission spectra resulting from the crystallisation of the nanostructured GST layer on top of the fibre tip are presented in Figure 33. The optically induced phase transition of the GST metasurface yields a substantial change in the optical parameters characterising the fibre-integrated device. The transition from the amorphous to the crystalline state involves an increase in the real part of the GST refractive index which results in a red-shift of the resonant feature by around 120 nm. The corresponding increase in the imaginary part of the refractive index brings about a decrease in average transmission of the device across the spectral range under investigation and a broadening of the resonance feature.

The closest agreement between experimental results and simulations is obtained when considering a non-dispersive GST layer with a refractive index equal to 4.2 and an attenuation coefficient of 0.4, rather than when using the values of dispersive crystallised GST. This is consistent with a partial crystallisation of the GST layer, which can be understood in light of Gallium implantation during FIB milling, changing the overall makeup of the layer on top of the fibre tip and, again, significantly affecting the way it responds to thermal annealing.

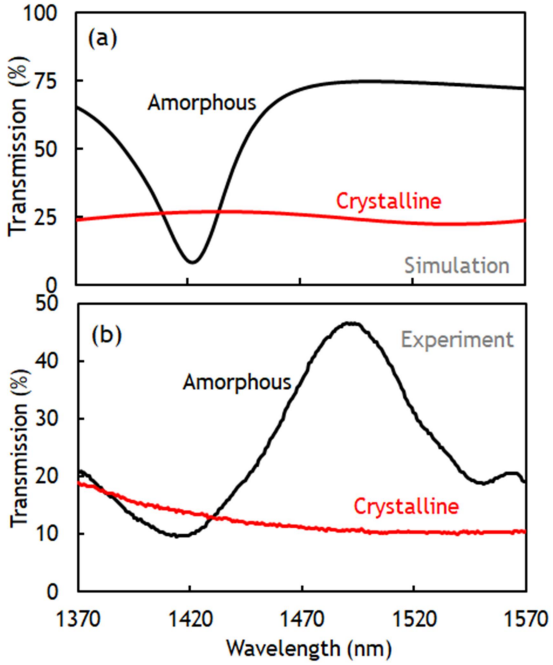


Figure 33 – (a) Simulated and (b) experimentally measured transmission spectra in the amorphous and crystalline states; P = 900 nm, w = 80 nm, t = 190 nm.

Numerically simulated field maps display the spatial profiles of the electric and magnetic fields (Figure 34) in both amorphous and crystalline phases. These field profiles demonstrate that, for both the electric and magnetic fields, the variation in optical parameters associated with the structural phase transition induced in the GST film leads to enhanced field absorption, with maximum electric and magnetic field intensities dropping drastically.

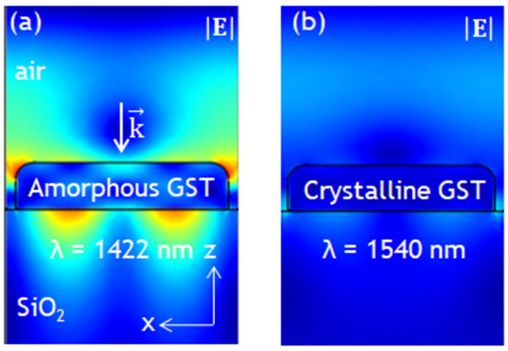


Figure 34 – Field maps displaying the norm of the electric and magnetic fields in the amorphous and crystalline phases. P = 900 nm, w = 80 nm, t = 190 nm.

This structural phase change entails a considerable variation in the absolute transmission of the fibre-integrated metasurface around the resonant wavelength band, by as much as 6.63 dB (experimentally measured, at 1500 nm), as seen in Figure 35. Simulated and experimentally obtained modulation spectra exhibit similarities when it comes to the spectral location of both

the minimum and maximum transmission modulation, around 1420 nm and in the [1500; 1550] nm band, respectively.

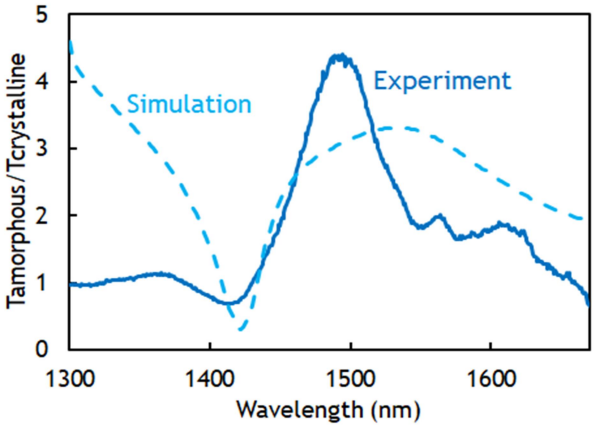


Figure 35 – Simulated and experimentally measured transmission ratios between amorphous and crystalline phases.

4.4. Conclusion

In conclusion, it has been demonstrated that the proposed fibre-integrated reconfigurable chalcogenide photonic metasurface is capable of realising intensity and dispersion switching. Experimentally measured intensity switching ratios reach 6.63 dB, at 1550 nm. Converting from amorphous to crystalline GST also enables switching on/off the dispersion control capabilities offered by this device. As numerically simulated, anomalous and normal dispersion near the resonant wavelengths are available, for all the periods investigated, with maximum GDD of 0.13 ps^2, on par with the best devices[91]. Besides, the use of metasurfaces enables the tuning of the spectral position of the metasurface resonances, by adjusting metamolecule geometry, enabling structurally engineered resonant operation anywhere within the near-infrared range.

5. Side-polished-fibre-integrated phase-change devices

5.1. Introduction

The integration of light-modulating devices with optical fibres can rely on methods other than merging chalcogenide layers, patterned or unpatterned, with fibre tips. In this context, side-polished fibres are an appealing alternative. Fibre-tip integration relies on intercepting the guided light beam by directly placing the light-modulating medium in its propagation path. The immediate downside of this approach is light absorption and a consequently weaker transmitted signal. In the case of side-polished fibres, the goal is to bring light guided along the core closer to the outer boundary of the fibre and facilitate its interaction with the material deposited on the side-polished surface. As, in this case, only evanescent interaction takes place, losses can be reduced when compared to the employment of fibre tips, while the long interaction length available in this configuration can help enhance the achievable maximum modulation depth. Lastly, the side-polished surface provides a large planar area on which thin film growth and device integration can be realised for a variety of different applications.

This section addresses the fabrication and optical characterisation, both numerical and experimental, of fibre-integrated devices based on GST films deposited on side-polished fibres. Resonant behaviour is induced by the presence of the high-index thick GST film, aiding coupling between the fundamental and higher-order cladding modes, which, in turn, help extend interaction to the GST film, thick enough to support a cavity mode. Tailoring the resonant wavelength as well as the visibility is achievable by adjusting the film thickness and core-to-plane distance, respectively, allowing placing the spectral feature in the wavelength band of interest, in this particular case, the near-infrared range. Numerical simulations and, to some extent, experimental results demonstrate that this spectral tuning is in fact possible. The nature of the resonance is also probed by analysing the simulated field maps.

The spectral modifications linked to light-induced structural phase change are numerically and experimentally investigated. Switchable intensity is reported, with modulation ratios of up to a factor of 9, at wavelengths longer than 1600 nm, and of a factor of 2 near the resonance, at 1340 nm.

Nanopatterning of the GST layer and ensuing spectral modifications are experimentally checked into, showing sub-wavelength periodic structuring could potentially provide an alternative route to spectral tuning.

5.2. Simulations

Lumerical MODE Solutions is employed for eigenmode analysis to identify the modes supported by the designed structure (schematically represented in Figure 36). These are then used as input to a finite-difference time domain (FDTD) propagation model from which transmission spectra and cross-sectional electric field distributions are derived. The geometrical model, shown in Figure 37, consists of three sections: two normal cylindrical fibres as the input and output waveguides, and the side-polished fibre in-between, in an attempt to more accurately replicate the experimental scenario in which light couples from the source into the side-polished fibre and then in to the spectrum analyser via singlemode, unpolished fibres. The input modes are generated at the input end of the first unpolished section, and the fundamental one is chosen for propagation along the proposed device. Symmetric boundary conditions along z are selected (given the structural symmetry along that direction), making the computation more efficient. Experimentally measured dispersion curves of the refractive index of the core and cladding materials of a standard singlemode fibre (SMF) are used. Core and cladding dimensions are chosen in order to reproduce those of an SMF: core and cladding diameters of 8 μm and 80 μm, respectively. Cladding diameter is smaller than that of a real SMF (typically 125 μm), in order to save on computation time. Nevertheless, a diameter of 80 μm should suffice in establishing a propagating mode which approximately resembles that of a real SMF[2]. The model assumes a polished length l = 160 μm (Appendix D). Ellipsometrically measured dispersion curves of amorphous and crystalline GST are also considered (Figure 11a). The transmission spectra are obtained by performing wavelength sweeps in the desired wavelength range (1200 – 1700 nm) and analysing the output light from the modelled device. Field maps are extracted by placing field monitors in the middle of the polished section.

[2] The normalised frequency is given by $V = \frac{2\pi a}{\lambda}\sqrt{n_{core}^2 - n_{cladding}^2}$, where a is the core radius, λ is the operation wavelength, n_{core} and $n_{cladding}$ are the refractive indices of the core and cladding, respectively. The normalised frequency is then determined by a, λ, and the index contrast between core and cladding. This contrast is only marginally affected by considering a cladding layer with a diameter of either 125 μm or 80 μm.

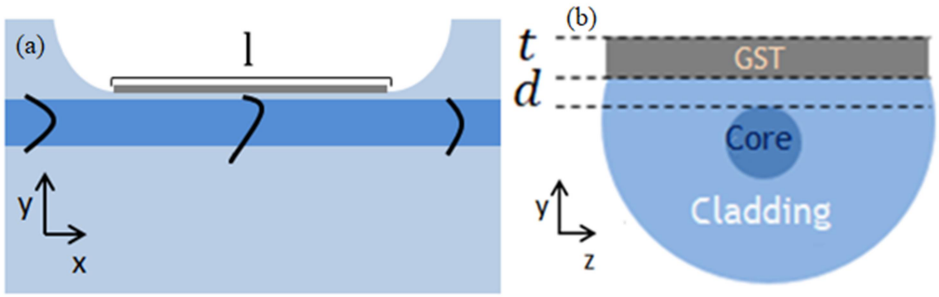


Figure 36 - (a) Pictorial representation of the mode profile as it propagates along the GST-covered side-polished fibre; (b) 2D schematic drawing of the cross-section profile of our structure; **l** – GST film length; **t** – GST film thickness; **d** – core-to-plane distance.

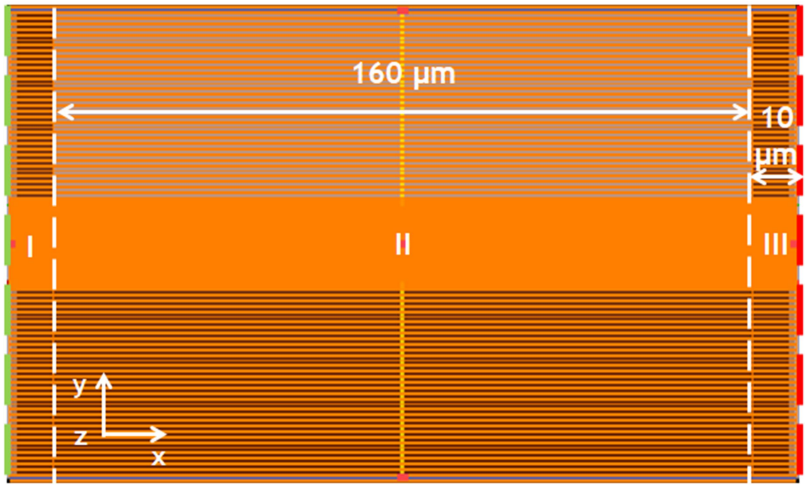


Figure 37 – Detail of the Lumerical MODE simulation environment, showing the three-section geometry of the modelled structure: I – unpolished input fibre; II – polished section; III – unpolished output fibre. Green and red dotted lines identify the input and output ports, respectively.

Mode propagation along the GST-covered polished section of a side-polished fibre can be well understood by drawing attention to the pictorial representation in Figure 36a: the original unperturbed fundamental mode propagating along the normal fibre enters the side-polished section, on top of which a high-index film has been deposited, and its profile is reshaped by this new waveguide configuration; this modification of the spatial profile of the fundamental mode results in an asymmetric power distribution with a more significant portion of the new propagating mode overlapping with the cladding layer, as the envelope wing closer to the film extends further out of the core. This a consequence of the presence of a high-index film which alters the refractive index distribution perceived by light, facilitating coupling to a higher order cladding mode, asymmetric given the intrinsic asymmetry of the structure being dealt with.

Varying the core-to-plane distance d will potentially modify this interaction. Interaction length l and film thickness t are set equal to 160 μm and 500 nm, respectively. Figure 38 illustrates how changing d from 2.4 μm down to 0.5 μm impacts on the strength of the interaction between guided light and the high-index GST film on top of the polished plane. In the bare side-polished fibre, light is confined to the core and the transmitted signal shows no particular features, being characterised by a flat dispersion. However, after adding the GST film, even for distances d close to 2 μm, the mode profile is clearly modified. This modification translates into the electric field distribution no longer being restricted to the core. The high-index thick GST film favours coupling between the fundamental mode, guided along the core, and a cavity mode supported by the thick GST film itself. The reasonable confinement within this GST layer results from the high refractive index contrast relative to the surrounding environment (cladding layer underneath and air above), combined with the sufficiently thick film, acting as a cavity. As d decreases from 2.4 μm down to 0.5 μm, the GST layer approaches the core and is able to more effectively interact with the guided mode. This results in more light coupling out of the core and in turn in higher modulation depth, as Figure 39b,c confirm in rather good spatial detail. This resonant response takes place at a specific wavelength, around 1340 nm for a 500-nm-thick GST film.

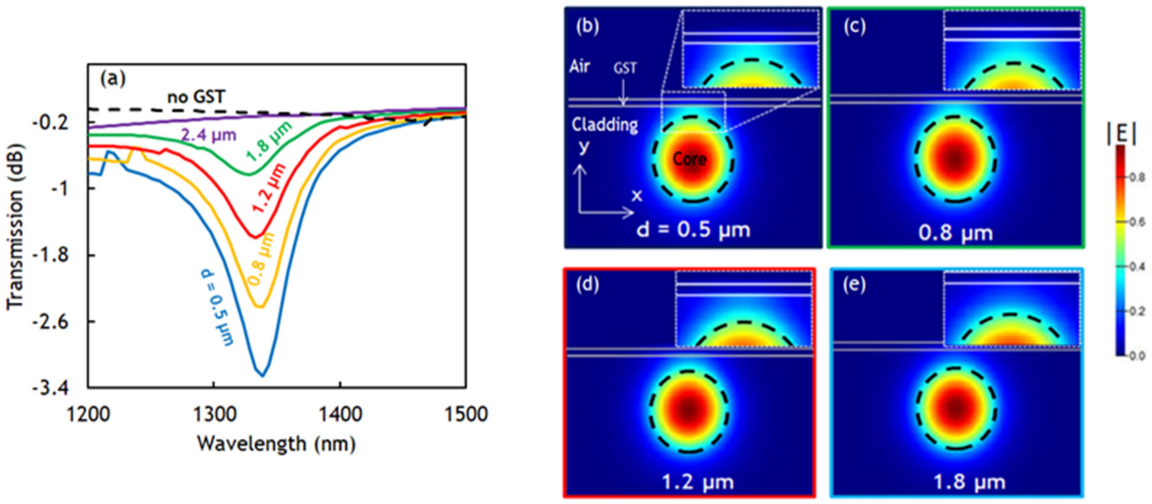


Figure 38 - (a) Simulated transmission spectra for different core-to-plane distances **d** (**t** = 500 nm, l = 160 μm); (b)-(e) corresponding simulated field profiles, taken at resonance (white lines indicate the GST layer).

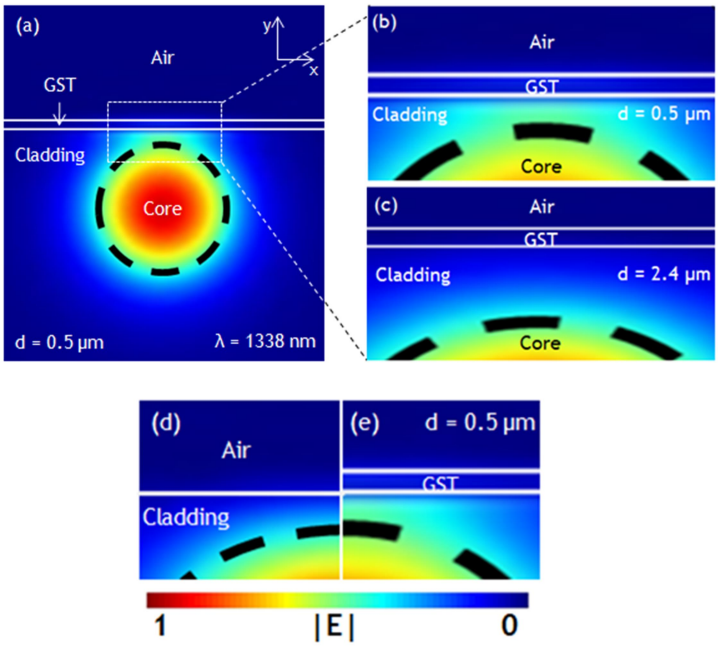


Figure 39 - (a) Electric field map at resonance when d = 0.5 μm and t = 500 nm; zoomed-in pictures of the cladding area above the core when t = 500 nm and (b) d = 0.5 μm or (c) d = 2.4 μm; detail of the cladding area of interest (d) in the case of a bare side-polished fibre and when (e) t = 500 nm and d = 0.5 μm.

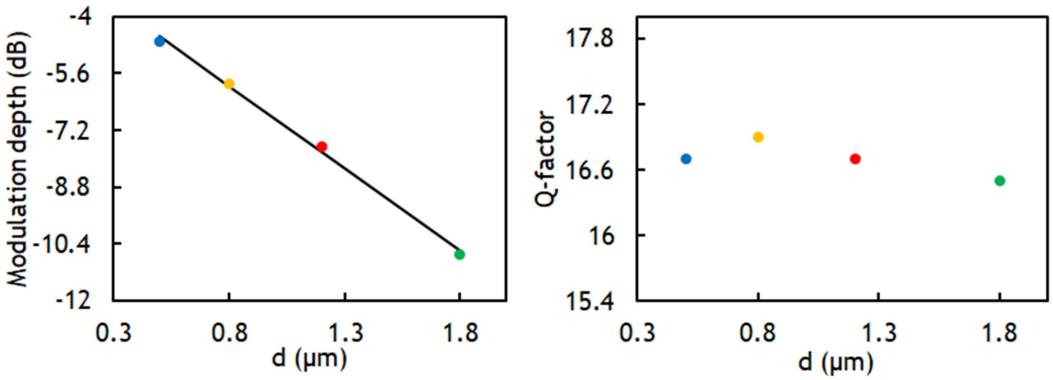


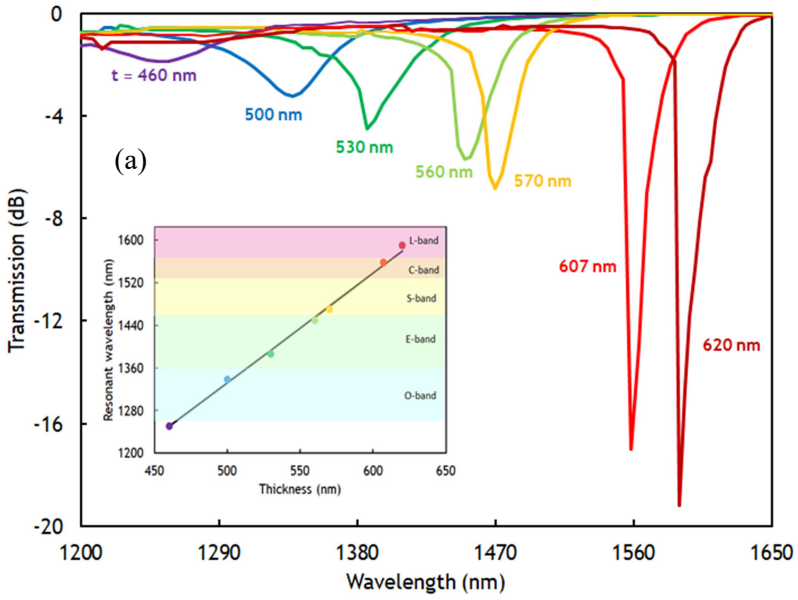
Figure 40 - (a) Modulation depth and (b) Q-factor as functions of the core-to-plane distance (**t** = 500 nm, l = 160 μm).

Figure 40a evidences that when d exceeds 2 μm, maximum transmission modulation depth ΔT_{max}[3] is lower than 0.05, meaning interaction is rendered very weak by the longer distance between core and plane, longer than the operation wavelength. Reducing d clearly affects transmission modulation, causing this parameter to vary from 0.2 (d = 0.5 μm) to negligible values (d = 2.4 μm). As Figure 40b indicates, the Q-factor is only marginally influenced by variations in d up to 1.2 μm, meaning the spectral selectivity of the coupling process between core and cavity modes is not significantly altered within this range of core-to-

[3] $\Delta T_{max}=(T_{max}-T_{min})/(T_{max}+T_{min})$

plane distances. Field maps of the electric field norm at resonance for different d help clarify that as the GST film is further removed away from the core, light intensity ascribed to the cladding mode, transferred via coupling between this mode and the fundamental one, reduces, explaining the increasingly lower visibility. Intensity associated with the excited cladding mode (and in turn with the cavity mode within the GST film), even for shorter d, as perceived by examining the field maps, does not seem compatible with the reasonably high visibility values obtained. In order to solve this incongruity it should be borne in mind that the interaction length is quite long (~ 160 μm, ~ $106\lambda_{operation}$), allowing for a cumulative effect to take place.

Controlling the transmission characteristics of the proposed GST-covered side-polished fibre can also be achieved by adjusting the GST film thickness t. Changing this geometrical parameter essentially contributes to redefining the coupling conditions between fundamental and cavity modes. This spectral tuning enables covering a wavelength range in the near-infrared that stretches, at least, from 1250 nm to 1590 nm, upon varying the thickness from 460 nm to 620 nm, encompassing the telecoms O- to L-bands. Interaction length l and distance d are set equal to 160 μm and 0.5 μm, respectively.



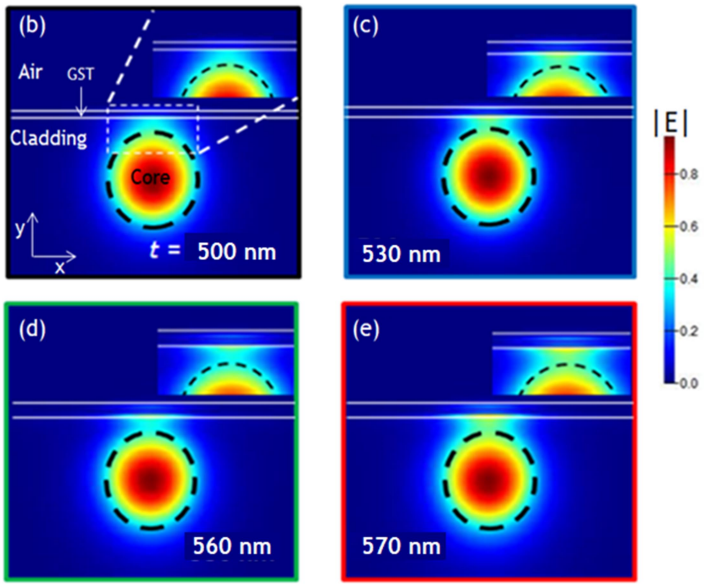


Figure 41 - (a) Simulated transmission spectra for different GST film thicknesses (d = 500 nm, l = 160 μm); insets: resonant wavelength as a function of t, field map when t = 620 nm; (b)-(e) corresponding simulated field profiles, taken at resonance (white lines indicate the GST layer).

Figure 41a already makes it apparent that thicker GST films lead to enhanced maximum modulation depths and Q-factors. Figure 42 shows this information in a more compelling fashion, stressing that setting t = 620 nm yields maximum values for both these parameters, equal to -0.11 dB and 61. When compared to the scenario when t = 460 nm, this represents an increase of 6.94 dB and by a factor of 5, respectively. This is due to the fact that thicker GST films facilitate coupling between core and cladding modes (and consequently, the cavity mode), leading to higher modulation depths.

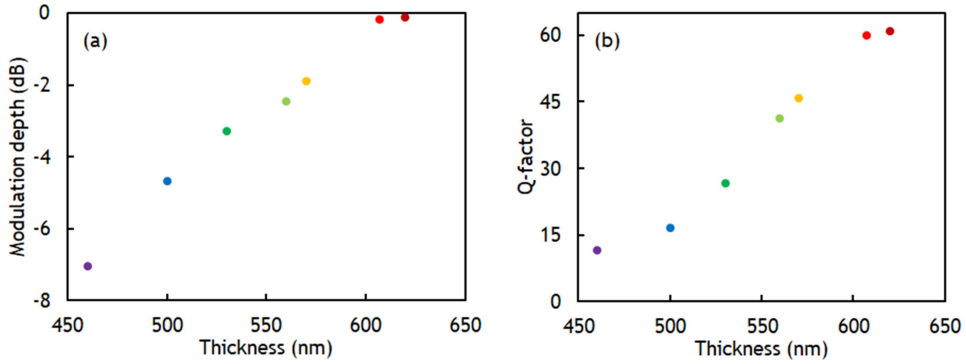


Figure 42 - (a) Transmission modulation depth and (b) Q-factor as functions of GST film thickness; (d = 0.5 μm, l = 160 μm).

It is shown that, even without structuring, a resonance can be introduced in the transmission spectrum of GST-covered side-polished fibres by exploring coupling between the fundamental core mode and a higher-order cladding mode, which in turn, helps extend interaction to the GST film (cavity mode). This coupling is made easier by the presence of a

high-index thick film deposited on top of the polished plane, which effectively alters the effective index ruling propagation in this context. The coupling conditions can be adjusted by tweaking some of the geometrical parameters of the structure, namely film thickness and its distance to the fibre core. Therefore, it is possible to tailor both the resonant wavelength and fringe visibility.

5.3. Experiments

Experimental realisation of this device concept is carried out first by preparing the side-polished fibres (l = 5 mm; Appendix D), essentially making sure they are clean enough for subsequent GST film deposition, being film adhesion a crucial aspect which might be hindered by remnant dirt on the side-polished surface. Leftover impurities still on the fibre after the polishing process are likely to be of an organic nature: wax used to fix the fibre onto a polishing block or oils used to measure transmission losses in a high-index medium in order to infer the core-to-plane distance. The cleanliness of the original side-polished fibres is evaluated using an SEM. Figure 43a shows a rather thick coating of what is supposed to be some leftover oil still on top of the side-polished surface. Reactive ion etching with a mixture of Ar and O_2, exploring oxygen´s ability to more efficiently target organic compounds, is carried out (30 mins, 70% Ar and 30% O_2, 210 V, 20 mTorr). The final result of this cleaning step is displayed in Figure 43b, being evident a cleaner surface is obtained. GST films with a thickness of 500 nm were subsequently deposited on single mode side-polished fibres, with a core size of 8 μm, by RF sputtering (Kurt J. Lesker Nano 38). A base pressure of $2x10^{-4}$ mbar is achieved prior to deposition and high-purity argon is used as the sputtering gas (70 ccpm to strike, 37 ccpm to maintain the plasma). The fibres are held within 10 K of room temperature on a rotating platen 150 mm from the target to produce low-stress amorphous as-deposited films. The surface of the GST film, as seen in Figure 43c, is characterised by a certain degree of roughness, which should not affect significantly the device operation.

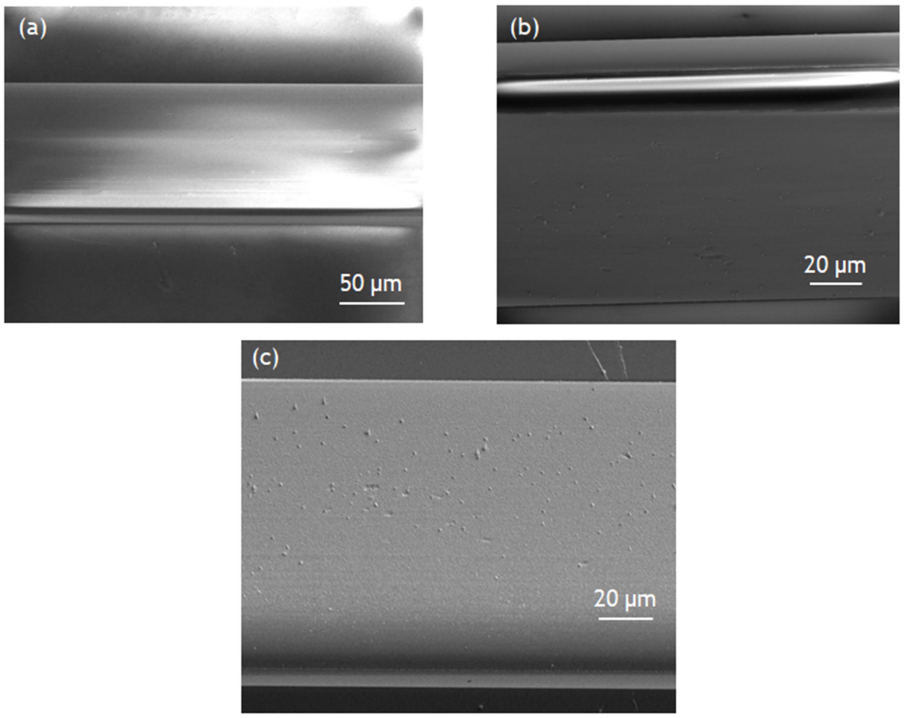


Figure 43 - SEM pictures of the side-polished surface (a) before and (b) after reactive ion etching; (c) SEM picture of a GST-coated side-polished fibre (GST deposited after the etching run).

The cross-section profile is imaged in order to perform a more accurate measurement of the core-to-plane distance, as portrayed in Figure 44. This step is taken at the end of the whole characterisation routine, but for reasons of formal coherence the results are presented in tandem with the SEM pictures of the polished surface, in what constitutes a more complete and thorough geometrical and morphological evaluation. In one of the fibres, the plane sits very close to the core, at a distance shorter than the operation wavelength (d = 0.5 µm); in the other, this distance is much longer, longer than the wavelength (d = 2.4 µm), meaning interaction between the high-index GST film and the core mode is expected to be very weak, as per the simulations results.

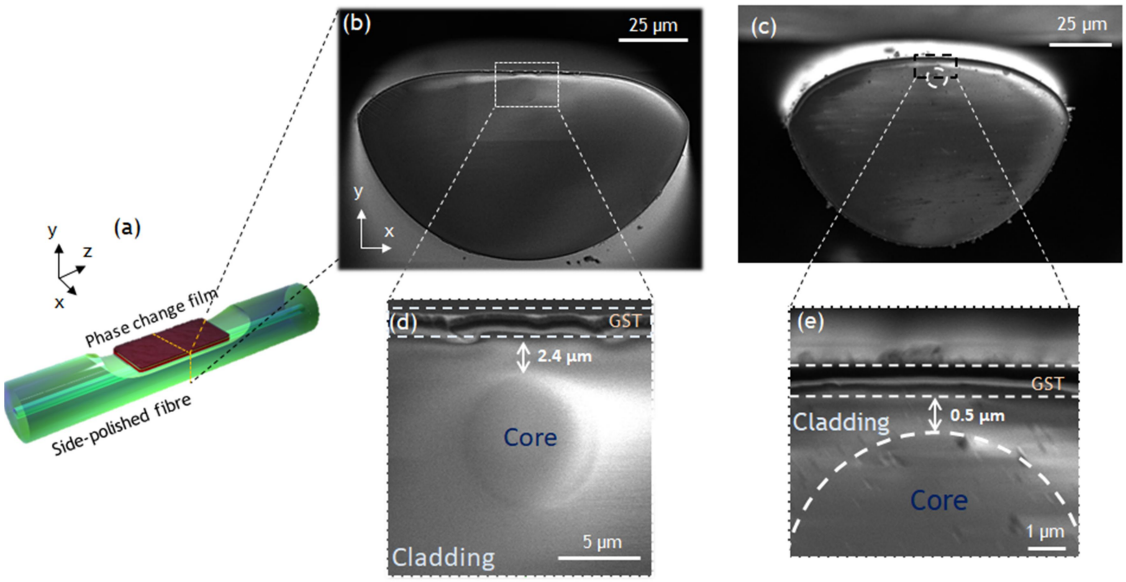


Figure 44 – (a) 3D schematic diagram of the device; (b)-(e) SEM pictures of the device and its cross-section profile. Both tested devices are shown (core-to-plane distances are displayed).

The transmission spectra were measured by launching near-infrared light ($1000 \leq \lambda \leq 1750$ nm) from a broadband light source (Thorlabs SLS201L) into the fibre and the output collected using an Optical Spectrum Analyser (Ando AQ-6315E). Figure 45 presents the measured transmission spectra of a normal single mode fibre along with the two side-polished fibres, before depositing the active chalcogenide layer. All curves exhibit a similar profile and relatively low losses, showing a flat response across the measured spectral range. The transmission characteristics change drastically upon depositing the phase change GST layer as shown in Figure 45b. It is observed that when the polished plane is close to the fibre core ($d = 0.5$ µm), depositing a GST film on the side polished surface gives rise to a clear resonance at $\lambda = 1330$-1340 nm in the transmission response of the side-polished fibre, a spectral modification brought about by the numerically predicted coupling between the fundamental and a higher-order cladding mode. On the other hand, when the polished plane is further away from the core ($d = 2.4$ µm), even with the inclusion of a high-index GST layer, the transmission response remains flat.

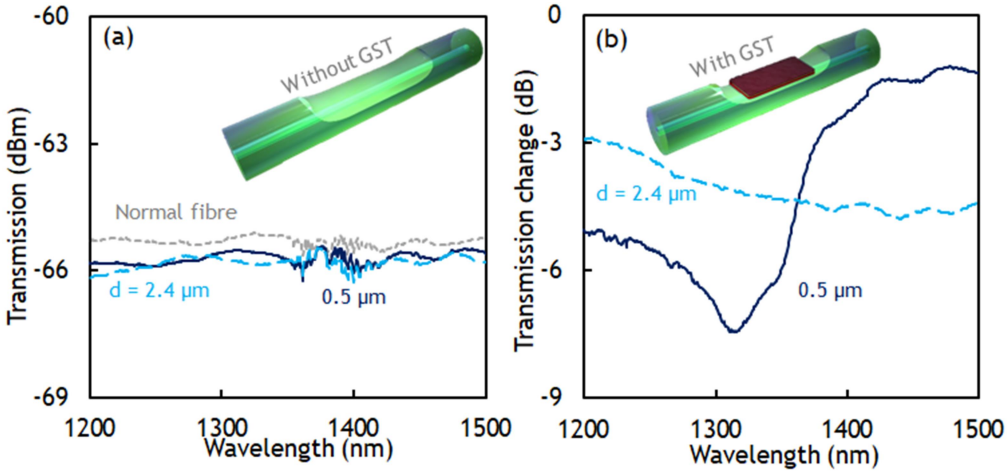


Figure 45 – Measured transmission spectra of (a) the tested bare side-polished fibres and of a normal singlemode fibre, as well as of (b) the GST-coated side-polished fibres (normalised relative to the respective bare side-polished fibre transmission spectrum); **t** = 500 nm, l = 5 mm; Dark and light blue curves correspond to different core-to-plane distances.

To assess the performance of our device as a fibre-optic switch based on a phase-change material, the side-polished surface is thermally annealed, using a hot plate on which the fibre sample is held, at 300°C for 20 minutes to fully convert the GST phase from amorphous to crystalline. The transmission characteristics shown in Figure 46 reveal that the increase in the real part of the GST refractive index associated with the amorphous-to-crystalline transition redshifts the resonant feature by around 370 nm. As a result of the phase transition in the chalcogenide layer, the absolute transmission of the structure close to the resonant wavelength changes by -2.8 dB, at 1338 nm (where transmission is higher in the crystalline phase), and by 9 dB at $\lambda > 1650$ nm (where transmission is higher in the amorphous phase). This is elegantly reproduced in our numerical simulations (Figure 46b) where, given the higher refractive index and attenuation of the crystalline phase, the simulated transmission spectrum for a side-polished fibre with d = 0.5 μm shows a near identical redshift of the spectral position of the observed resonance and a lower electric field intensity in the GST film. Any discrepancies between simulations and experimental measurements are related to manufacturing and crystallisation imperfections, i.e., deviations from the ideal model geometry such as a slight angle offset on the side-polished surface due to over-polish or to possible contamination/stoichiometric change in the uncapped-GST during crystallisation, which may create changes in the refractive index (real and imaginary parts), generating a more or less pronounced disparity between the actual optical properties of the deposited film and those used as reference (Figure 11a). In fact, measuring a higher experimental Q-factor than the one obtained numerically, as comparison between Figure 46a and b highlights, suggests a lower extinction coefficient of crystalline GST in the experimental device than assumed in simulations (Appendix E sheds some light on the possible

impact of considering different values of the extinction coefficient on the Q-factor of the resonance after crystallisation). Figure 46c,d, and Figure 47 more emphatically so, communicate that, besides stronger coupling between core and cladding modes in the amorphous state (less hampered given the lower extinction coefficient in this structural phase), the guided mode extends further beyond the core in the crystalline state. This could be attributed to higher reflection from the crystalline GST layer in combination with less efficient light confinement at 1708 nm than at 1338 nm (spectral locations of the resonance in the crystalline and amorphous states, respectively). The extent of this second contribution can be grasped by evaluating how the evanescent field decay length in a normal SMF fibre changes with wavelength (Appendix F)

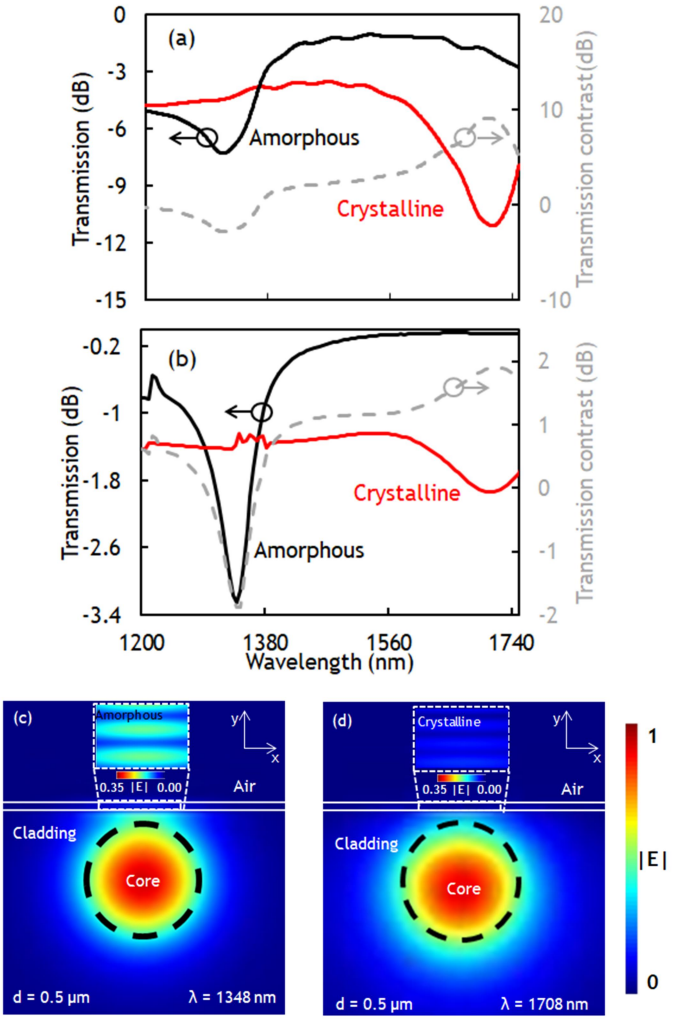


Figure 46 – (a) Experimental and (b) simulated transmission spectra of a side-polished fibre coated with amorphous (black) and crystalline (red) GST (**t** = 500 nm, **d** = 0.5 µm) along with the measured contrast ratio between transmission in the amorphous and crystalline phases (dashed grey line); field maps at resonance for a side-polished fibre coated with (a) amorphous and (b) crystalline GST (**t** = 500 nm; **d** = 0.5 µm; amorphous @ 1338 nm; crystalline @ 1708 nm).

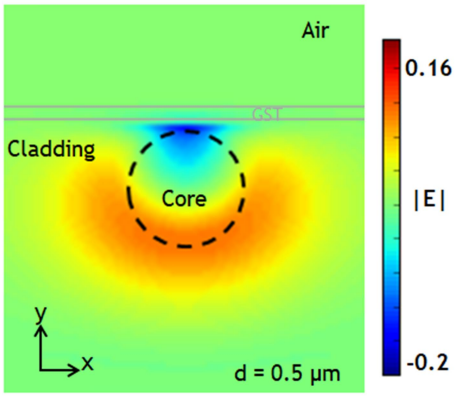


Figure 47 - Change in the strength and spatial distribution of field between the two phase states of the GST layer, evaluated as the difference between panels (c) (d) in Figure 46.

5.4. Patterned GST layer on a side-polished fibre

This concept can be further extended to include patterned dielectric films and take advantage of potentially enhanced interaction between these structures and light guided along optical fibres. As a way of putting this hypothesis to the test, a rather crude attempt is made at fabricating a long grating on a GST-covered side-polished fibre. This endeavour is limited to the experimental side of things, since the model introduced in the beginning of this section does not perform well when this sort of structure, essentially consisting in a periodic patterning of the chalcogenide layer at the subwavelength scale, is tested. The values of the geometrical parameters of the grating are selected based on a preliminary COMSOL simulation of GST gratings on SiO_2 substrates, in which these values show good resonances in the desired wavelength range, around 1500 nm (Appendix G). This is, evidently, very tentative, since in the actual devices under investigation light interaction takes place under distinct circumstances, such as illumination with guided modes interacting evanescently with the grating instead of using a normally-incident plane wave, or the existence of a cladding layer acting as a buffer between core and structured film.

A very long grating (240-µm long) is FIB-machined on the GST film, ensuring the interaction length is potentially long enough to attain a noticeable change in the transmission characteristics of the fibre. GST deposition follows the same procedure as the one established for thick film deposition, being the film thickness (deposition time) the only difference: 300-nm-thick films are grown instead. A sub-wavelength period (i.e. non-diffractive) grating, with a fixed linewidth w ~ 200 nm and period P equal to 960 nm, each covering an area of approximately 30 µm × 240 µm, were etched through the GST layer by FIB milling (FEI Helios NanoLab 600), as illustrated in Figure 48a. During processing, special care is taken to align the

nanostructured area over the fibre core, ensuring experimental light measurements reflect the interaction of light with the structured medium fabricated on the side-polished plane. Given the size of the grating, much larger than the field of view preferentially used to obtain good enough resolution (~ 20 nm), eight 30 µm × 30 µm gratings were stitched together, each of which with a size compatible with the aforementioned field of view.

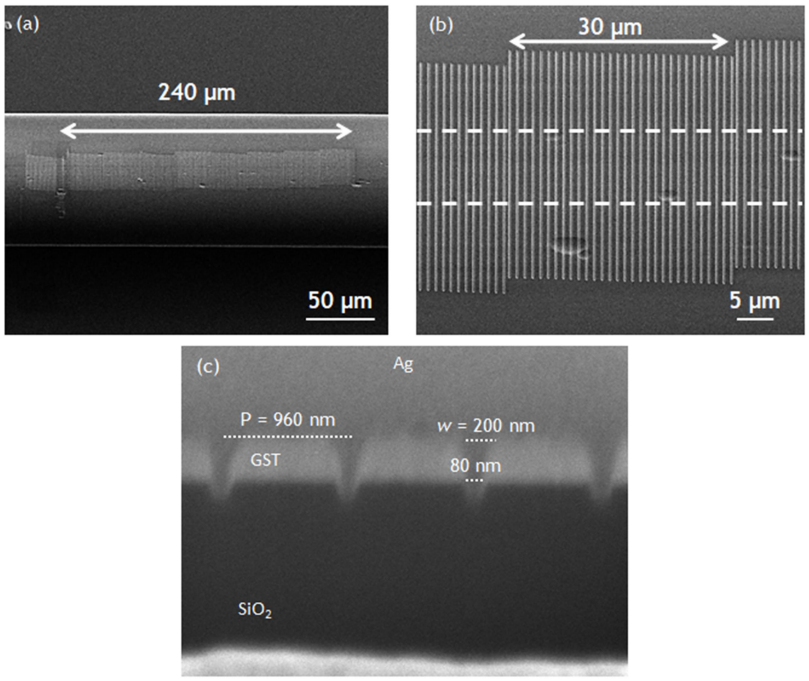


Figure 48 – (a) SEM picture of a 240-µm-long grating etched on the 300-nm GST layer deposited on a side-polished fibre; (b) close-up of the transition region between three 30-µm stitched gratings (white dashed lines identify the fibre core; (c) cross-section profile of the structured GST film.

The transmission spectrum of the side-polished fibre before and after GST grating fabrication is taken, following the same procedure for transmission measurements employed in the case of a fibre with a thick unstructured chalcogenide film deposited on top of it. The curves plotted in Figure 49 confirm that spectral changes are induced by periodically structuring the GST film: as longer gratings are fabricated, the more pronounced the spectral feature around 1290 nm seems to be. The poor fringe visibility can be explained by a long core-to-plane distance, even though this parameter was not measured in this specific instance, leaving this consideration without experimental backing. As it is, a lack of sufficiently strong experimental evidence supporting claims regarding the exact nature of this resonance is manifest. In order to be unequivocally able to associate this resonance with possible light interaction with the grating, a battery of extra tests would have to be run, particularly: repetition of the fabrication and characterisation process to ensure reproducibility; fabrication and characterisation of gratings with different periods to assess the resulting shifts in the spectral position of the resonance.

Extra work on adapting the Lumerical model to more adequately simulate light interaction under these specific circumstances might prove helpful in probing the type of resonant behaviour being dealt with.

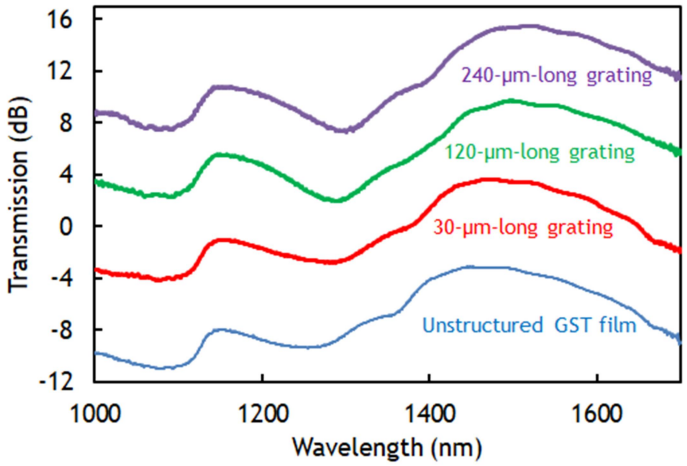


Figure 49 – Transmission of a side-polished fibre covered with an unstructured GST film and after fabrication of a grating, of increasing length, milled through that same GST layer (normalised relative to the bare side-polished fibre; each curve is offset by 6 dB).

5.5. Conclusion

In conclusion, a side-polished fibre-integrated phase change memory device capable of non-volatile switching around the 1330 nm telecom band is demonstrated for the first time. Maximum modulation of the transmitted light in our side-polished fibre coated with a 500 nm-thick GST film, upon crystallisation, reaches -2.8 dB at 1338 nm and 9 dB at longer wavelengths, contrast ratios that are more than adequate for short-reach (intra-/interchip) optical interconnect applications in data processing architectures[168]. By adjusting the thickness of the phase-change layer, a transmission resonance could be engineered anywhere within the transparency range of the high-index, phase-change medium and supporting fibre, without the need for costly nanopatterning techniques, covering the telecoms O- to L-bands. It should also be noted that full amorphous-crystalline phase switching is not essential to maximising optical switching contrast at the amorphous phase resonance wavelength: it can be seen from Figure 46a that partial crystallization, resulting in a smaller refractive index change and smaller red shift, would suffice to deliver the same transmission switching function; and this would be at considerably lower switching energy (the extent of crystallisation being a function of annealing temperature and time).

Sub-wavelength periodic structures carved into the chalcogenide layer can prove to be an interesting strategy in coming up with new interaction configurations that might enhance the resonance quality factor and transmission contrast, as well as improve spectral tuning via manipulation of the geometrical parameters characterising the nanoscale array. The experimental data produced in this project is still fragile, but it definitely shows that pursuing this path can lead to novel fibre-integrated devices.

6. Phase change Huygens´ metasurfaces based on GST nanodiscs

6.1. Introduction

Subwavelength dielectric nanodiscs constitute the most widely implemented strategy aimed at experimentally realising Huygens´ metasurfaces[169-184]. These structures play host to magnetic and electric dipoles whose spectral characteristics, namely the wavelength at which the respective extinction maxima occur, can be tuned by changing the configuration of the nanodiscs array, particularly by adjusting the disc diameter. Notably, spectral overlap between the two extinction coefficient maxima can be achieved for a given array design, owing to the different sensitivity these dipoles exhibit to variations in the geometrical parameters of the ensemble, yielding suppressed backscattering of light, which translates into very low reflection. Adding to this remarkable feature, the use of low-loss dielectric materials such as silicon results in high levels of light transmission in the near-infrared, approaching unity[169,171]. Furthermore, the dielectric nature of the resonances ensures that large mode volumes can be generated, which leads to pronounced light-matter interaction[169,177].

Wave-front engineering in the near-infrared relying on Huygens´ metasurfaces has been successfully attempted[171,172,176]. The key to attaining the desired wave-front shape rests on the fact that the optical phase imparted to light travelling through the metasurface depends on the specific dimensions assigned to the structure being used as a beam-shaping device. Among the most relevant achievements in the context of wave-front manipulation, one can count beam steering and pulse compression[172], made possible by the strong negative group-delay dispersion imparted by the metasurface, conversion of ordinary Gaussian beams into more exotic shapes such as vortex beams[171], and more complex wave-front control employed resorting to holographic Huygens´ metasurfaces to obtain less conventional shapes[176].

By virtue of the possibility of controlling field confinement and enhancement, structured media stand out as a preferred means to enhance the conversion efficiency in optical nonlinear phenomena. Second-[177,184] and third-harmonic generation[170] using semiconductor all-dielectric metasurfaces have been reported, with enhancement factors of several orders of magnitude relative to unstructured surfaces.

The ability to dynamically tune the spectral characteristics of the resonances associated with Huygens´ metasurfaces emphasises their suitability for employment as reconfigurable devices[173,174,179-182]. Dynamic control of the spectral features these metasurfaces play host to can be achieved through a number of strategies, for instance, by embedding nanodiscs arrays in liquid crystals, whose optical parameters can be thermally[173,181] or electrically[179] manipulated, or via ultrafast all-optical light modulation resting on semiconductor metasurfaces[174,180]. Combination of Huygens´ metasurfaces with an ENZ thin film targeting dynamic transmission

control has also been pursued[182]. Exploring the nonlinearities present in Huygens´ surfaces made out of semiconducting materials such as GaAs has also paved the way for broadband optical frequency mixing[183].

Practical applications for these all-dielectric platforms also include shaping the photoluminescence spectra of quantum dots[175] as well as the development of highly sensitive biosensors[178].

This section addresses the fabrication and optical characterisation, both numerical and experimental, of phase-change Huygens´ metasurfaces based on FIB-milled GST films deposited on flat glass substrates. Structuring the chalcogenide film enables the introduction of tunable resonances in the transmission and reflection spectra. Tailoring the resonant wavelength is achievable by adjusting the metamolecule geometry, allowing placing the spectral feature in the wavelength band of interest, in this particular case, the near-infrared range. Numerical simulations and experimental results demonstrate that this spectral tuning is in fact possible. The nature of the resonance is also probed by analysing the simulated field maps.

The spectral modifications linked to light-induced structural phase-change are investigated. Switchable intensity is reported, with modulation spectra which can be engineered by acting upon the geometry of the metamolecule. Maximum modulation ratios of 2 and 2.2, in reflection and transmission, respectively, are registered.

6.2. Simulations

Simulations are run using a finite element numerical solver (Lumerical FDTD Solutions). The model assumes a dispersive SiO_2 substrate (Palik) and uses ellipsometrically measured values of the complex permittivity of GST, as presented in Figure 50a. Normal-incidence illumination using a plane-wave is considered. The electric field is set perpendicular to the direction of propagation, along one of the lines of GST nanodiscs sitting on top of the silica substrate, as exemplified in Figure 50b. Light incidence upon the modelled structure is determined by the specifications of the source, which allows choosing whether light travels from the SiO_2 substrate into the discs or the other way around, the input power and angle of incidence. By virtue of periodic boundary conditions, an infinite array of GST discs in the x-y plane is simulated. Throughout the numerical study of the interaction between this metamaterial design, based on an array of identical, evenly spaced GST discs, and electromagnetic radiation, several parameters have been swept, namely those characterising geometrical features, such as diameter D, GST film thickness t and gap width between neighbouring GST discs w; the structural phase of the GST film has also been changed. The impact of these modifications on reflection spectra, as well as on the field maps portraying the spatial profile of the electric and magnetic fields, are evaluated in the following.

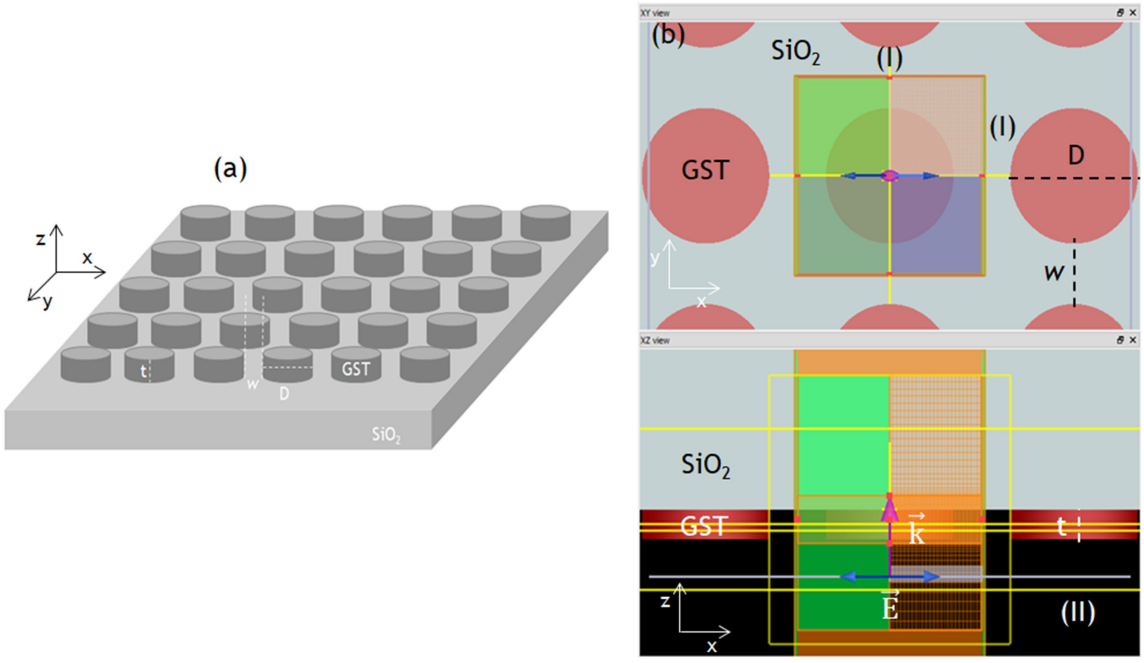


Figure 50 - (a) 3D schematic representation of the periodic GST disc array; (b) 2D schematic diagram showing the Lumerical-modelled geometry, materials and configuration of the interaction between light and metamaterial structure; (I) Periodic boundary conditions; (II) reflection monitor.

The reflection spectra are obtained for different diameters D of the GST nanodiscs, ranging from 800 nm down to 450 nm, being w and t equal to 200 nm and 220 nm, respectively, and plotted in Figure 51a. In the case of large D, the reflection curve features two spectrally close resonant modes in the near-infrared region: electric dipole (ED) at shorter wavelength and magnetic dipole (MD) at longer wavelength. As D is reduced, the resonances blueshift and the ED mode ends up collapsing, while the other spectral feature is preserved throughout the entire diameter sweep, albeit exhibiting continuously lower quality factors (Q-factor), owing to the increasingly higher extinction factor of the GST layer. The simulated field maps associated with the two reflection resonances for d = 800 nm display clear differences: while the MD resonance shows a well-confined electric field within the GST disc and a dipolar structure for the magnetic field, the ED feature reveals an electric field more localised near the edge of the disc accompanied by a well-contained magnetic field. Given the different spatial profiles of the associated fields, the resonances harboured by our structure respond to changes in the geometry of the array unit cell in a distinct fashion, which explains why only the one characterised by a confined electric field is preserved throughout this diameter sweep. Considering smaller disc diameters continually blueshifts the now single reflection resonance. The fact that, unlike in other dielectric Huygens´ metasurfaces made out of materials with lower losses in the near-infrared such as silicon[169], the spectral overlap between the preserved mode and the one generated by smaller dielectric discs cannot be resolved can be attributed to the now relevant losses registered in GST, considerably enhanced as one moves to shorter wavelengths, which contribute to a significant broadening of the resonances at play.

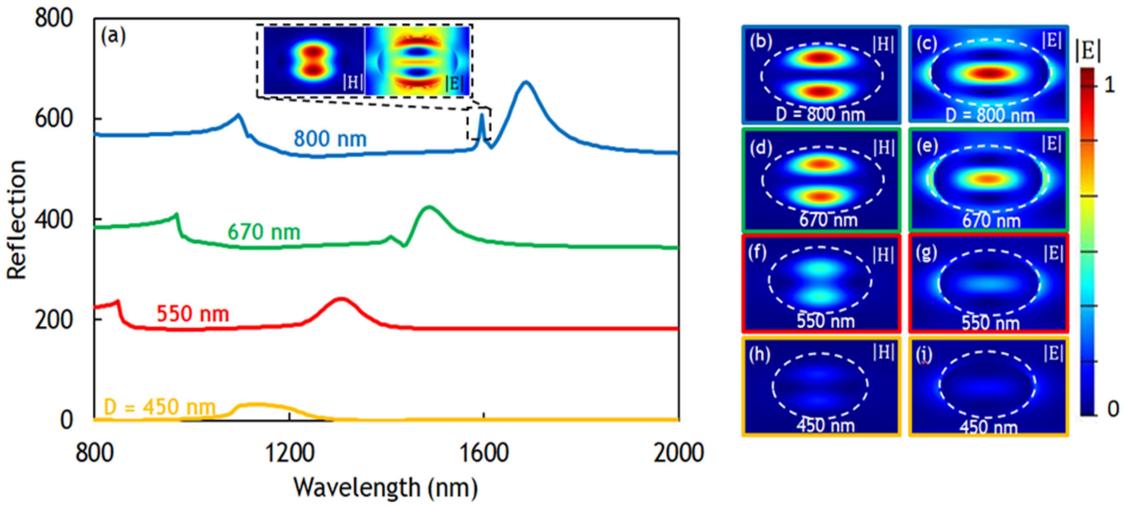
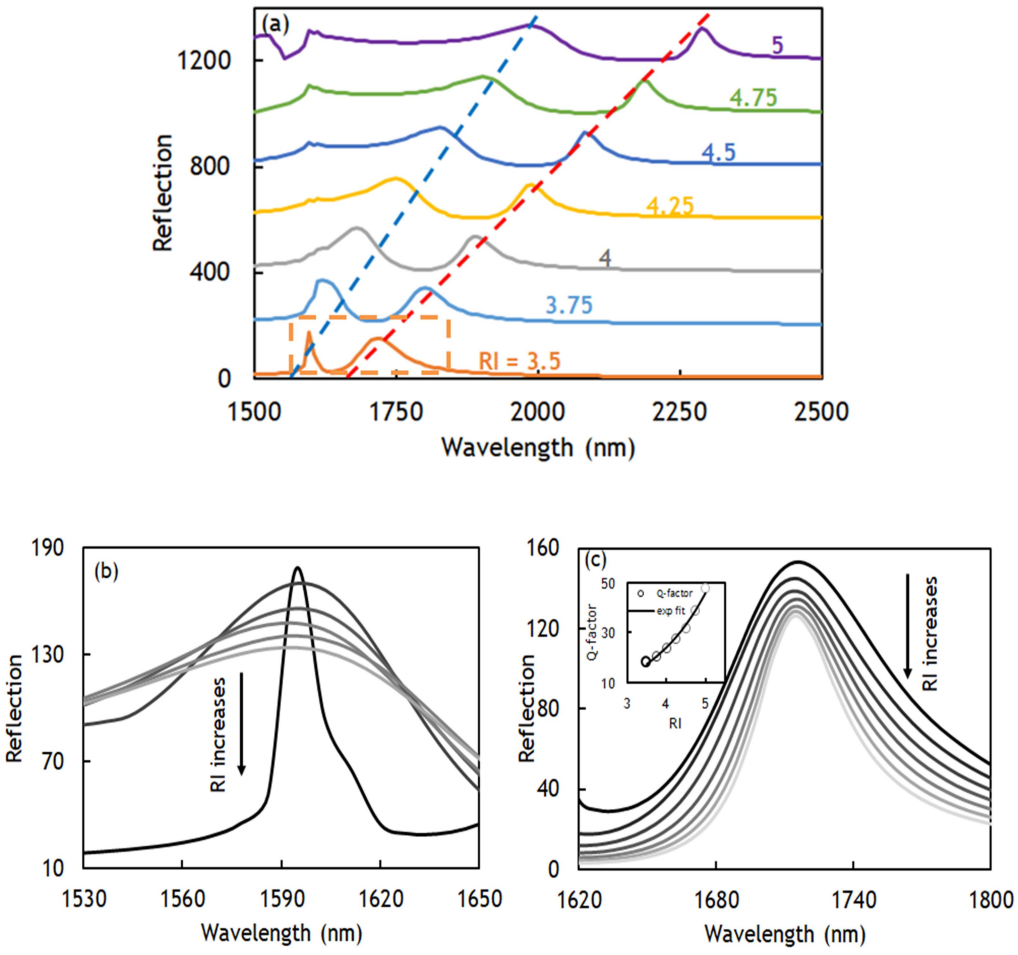


Figure 51 - (a) Reflection spectrum of arrays of discs, made out of amorphous GST, with varying diameter D; (b)-(i) corresponding electric and magnetic field maps at resonance (MD); Inset: electric and magnetic field maps corresponding to the ED, for D = 800 nm; w = 200 nm, t = 220 nm.

In an attempt to predict the disc array behaviour when the real part of the refractive index increases, Figure 52 depicts the simulated reflection spectra of an array of nanodiscs with D = 800 nm, w = 200 nm and t = 220 nm, made from a non-dispersive, lossless dielectric material with a refractive index (RI) varying from 3.5 (akin to lossless GST) up to 5. As expected, increasing the refractive index results in a redshift of both resonances. However, given the different spatial profiles of the fields associated with these features, the shift imposed on the resonance at longer wavelength is more pronounced (field better confined inside the GST disc). In the case of the ED mode, analysing the overlapping resonances in Figure 52b reveals an increasingly poorer quality factor as the refractive index approaches the maximum value investigated. As for the other peak (Figure 52c), maximum reflection suffers from an increase in refractive index, but the associated quality factor is actually enhanced, increasing in an approximately exponential fashion (inset Figure 52c). The field maps plotted in Figure 52d-p**,** illustrating how both the magnetic and electric field magnitudes change as the refractive index varies, reinforce these observations, exhibiting enhanced and weaker field intensities associated with the MD and ED modes as the refractive index increases, respectively.



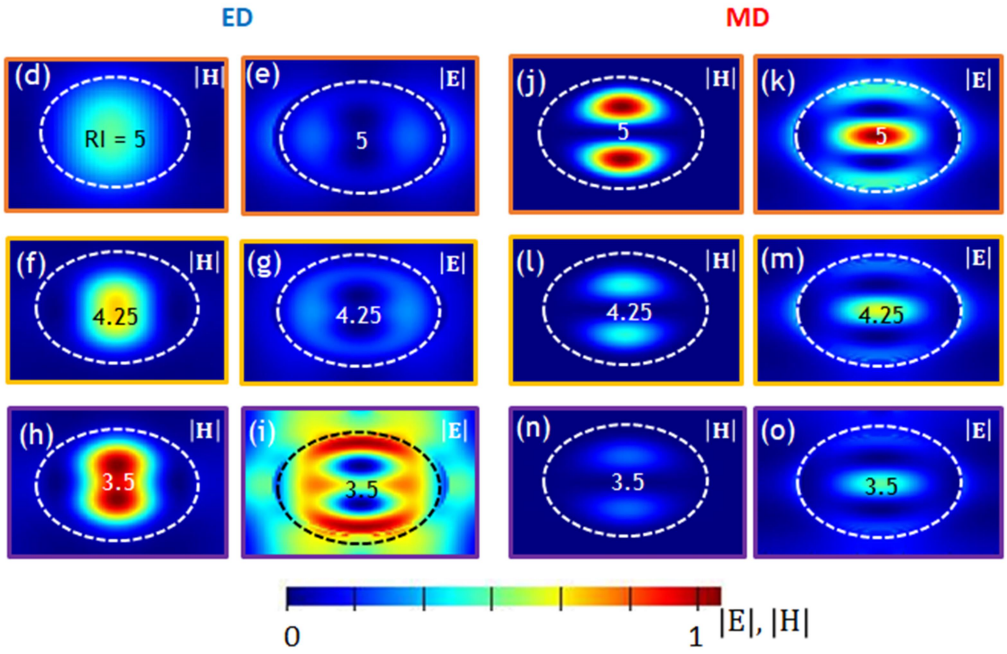


Figure 52 - (a) Reflection spectra of arrays of discs made out of a non-dispersive dielectric material with varying RI and κ = 0.0 (each curve is offset by 200; blue and red dashed lines serve as visual aids to isolate the two dipole modes); overlapping (b) ED and (c) MD resonances; Inset: Q-factor as a function of RI; (d)-(o) corresponding electric and magnetic field maps at resonance, for both the electric (ED) and magnetic dipoles (MD) (dashed lines identify the GST disc); w = 200 nm, t = 220 nm.

Figure 53a features the simulated reflection spectra of an array of nanodiscs made from a non-dispersive, lossless dielectric material with a refractive index equal to 5.5, when D varies from 800 nm down to 500 nm, being w = 200 nm and t = 220 nm. These show that under these circumstances, i.e. when losses are neglected, after the extinction of the ED mode, observed when D = 600 nm, a further reduction of D brings about mode crossing, with the mode that used to sit at longer wavelength (MD) now sitting at shorter wavelength. Again, this mode is the only one preserved throughout the whole diameter sweep, retaining its characteristic well-confined nature, as demonstrated by the field maps in Figure 53b-o. This sweep is performed primarily as a sanity check on our model and the assumption that, in the event of a lossless dielectric material with high RI (> 3.5), we are dealing with Huygens surfaces where the previously described mode crossing would take place.

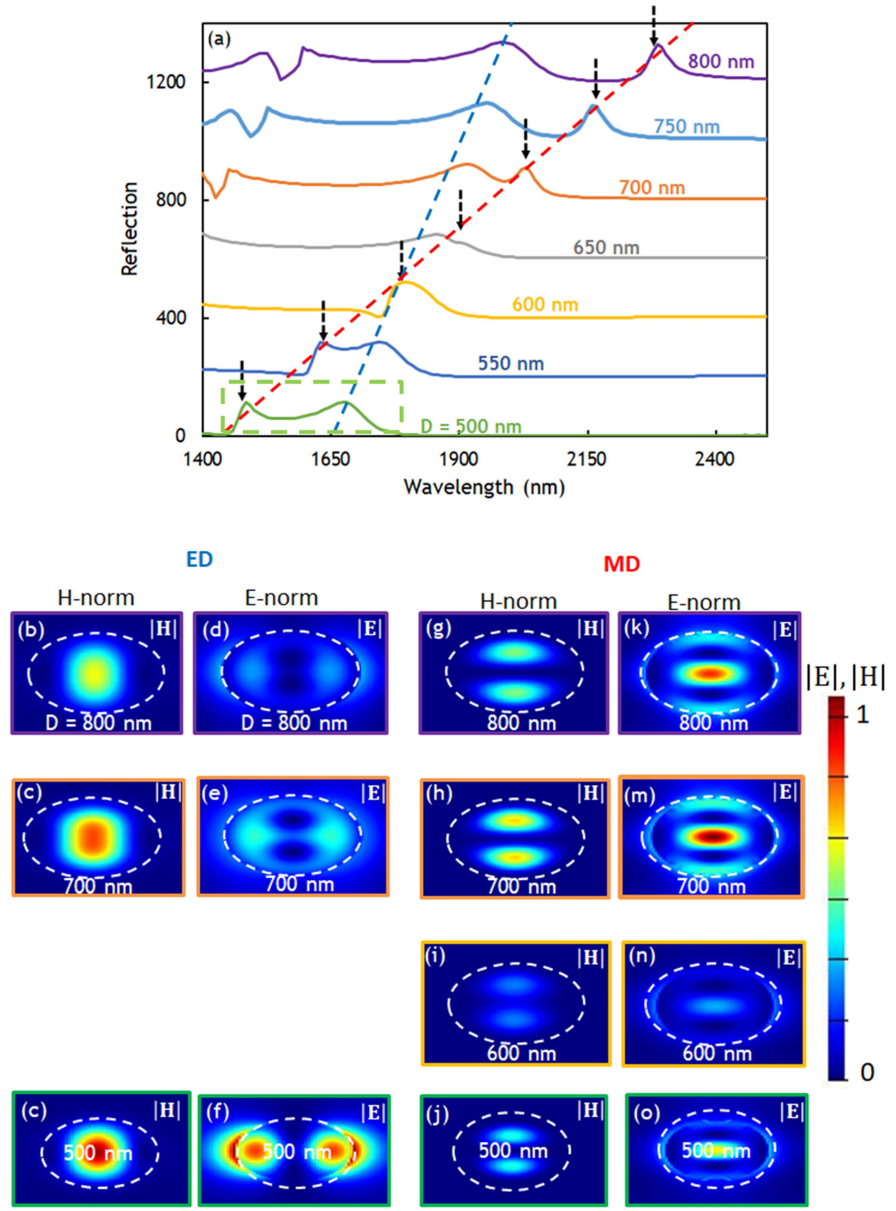
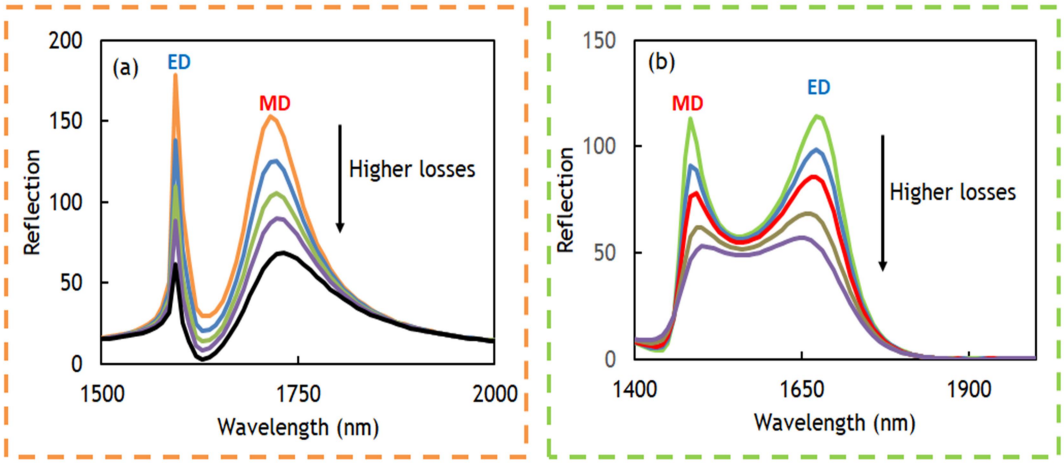


Figure 53 - (a) Reflection spectrum of arrays of discs with varying D, made out of a non-dispersive dielectric material with RI = 5.0 and κ = 0.0 (each curve is offset by 200; blue and red dashed lines serve as visual aids to isolate the two dipole modes); (b)-(o) corresponding electric and magnetic field maps at resonance, for both the electric (ED) and magnetic dipoles (MD) (white dashed lines identify the GST disc); dotted arrows identify the ED mode; *w* = 200 nm, t = 220 nm.

In this instance, inspecting how the reflection spectral features respond to increasing losses in the dielectric layer is relevant, especially when considering the possibility of promoting spectral tuning via crystallisation of the GST layer, which inevitably entails an increase in the extinction coefficient. This inspection is carried out in two specific scenarios: non-dispersive dielectric material with varying κ, setting D = 800 nm, w = 200 nm, t = 220 nm, RI = 3.5 as well as D = 550 nm, w = 200 nm, t = 220 nm, RI = 5.0. The first case

corresponds to discs made out of a lossy, non-dispersive dielectric material with the same RI as amorphous GST, with a diameter which yields the highest MD mode field intensity, resulting in higher resonance visibility, a circumstance whose experimental replication is quite appealing. The latter concerns discs made out of a lossy, non-dispersive dielectric material with the highest RI tested in the simulations, close to that of fully crystallised GST. In both cases, an increase in κ, from 0.0 to 0.2, damps the reflection resonances, clearly reducing the associated maximum reflection values. This observation, besides being confirmed by the spectra in Figure 54a,b, is also backed by the filed maps in Figure 54c,d, where a clear decrease in field intensity at resonance for both ED and MD modes accompanies the introduction of higher losses in the dielectric layer. These filed profiles also demonstrate that the characteristic field distribution of the MD mode remains unchanged, regardless of diameter and RI, whereas the electric and magnetic fields of the ED mode suffer a change of spatial configuration, brought about by diameter reduction (from 800 nm down to 500 nm) when RI = 5.0, as Figure 54 had already illustrated. For the array made out of a non-dispersive material with RI = 3.5, both resonances are spectrally close, meaning there is a degree of spectral "contamination" between MD and ED modes, which explains the onset of a "quasi-dipolar" structure of the magnetic field of the ED mode (a monopolar profile would be expected, in the absence of this spectral "contamination").



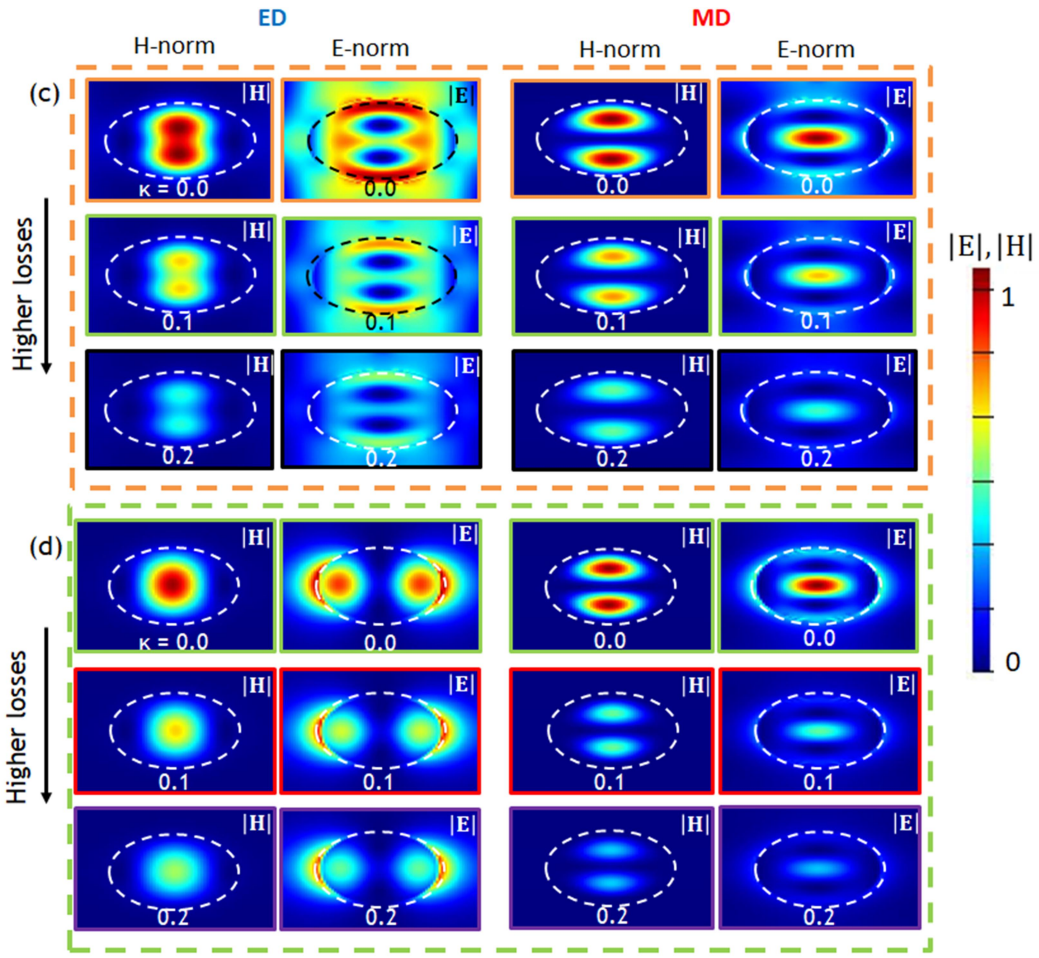


Figure 54 - Reflection spectra of arrays of nanodiscs made out of a non-dispersive dielectric material with varying κ and (a) D = 800 nm, w = 200 nm, t = 220 nm, RI = 3.5 as well as (b) D = 550 nm, *w* = 200 nm, t = 220 nm, RI = 5.0; (c), (d) corresponding electric and magnetic field spatial profiles for both ED and MD for varying extinction coefficient.

As a matter of completion, both t and w are changed and the ensuing spectral modifications assessed. Increasing the thickness of a dielectric material out of which the discs are fabricated implies a higher effective refractive index perceived by light as it travels through the array. Hence, varying t, from 200 nm up to 230 nm, results in a redshift of the reflection resonances, as confirmed by the spectra in Figure 55a. The ED mode appears more sensitive to these geometric alterations: reducing t down to 200 nm is enough to dissipate the ED resonance. Given the dielectric nature of the resonances at play, field confinement is in great measure determined by the modal volume. The larger modal volume associated with the ED mode is patent in Figure 55b, explaining the enhanced susceptibility this mode exhibits to variations in film thickness.

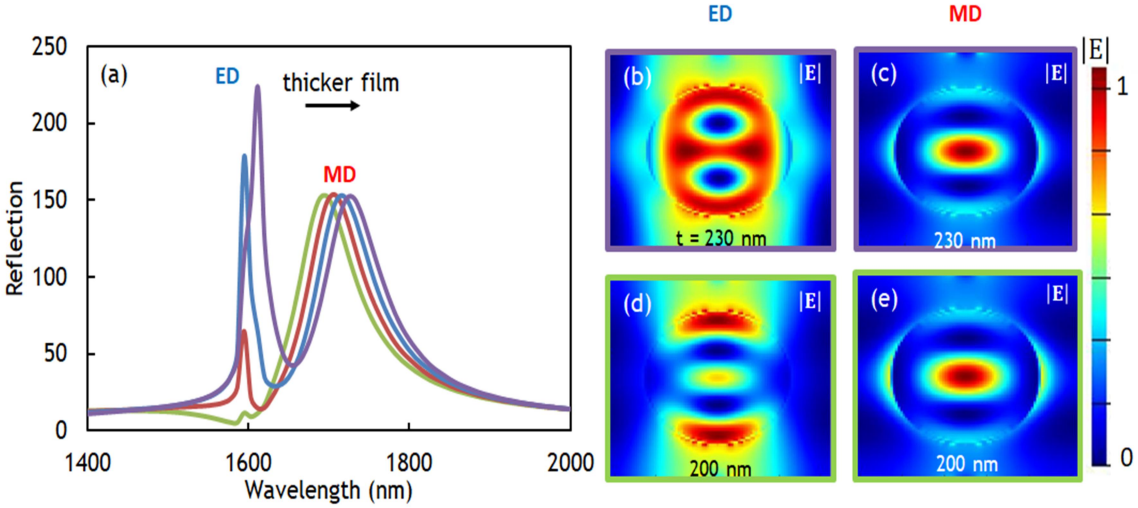


Figure 55 - (a) Reflection spectra of arrays of nanodiscs, made out of a non-dispersive dielectric material with RI = 3.5 and κ = 0.0, with varying t (from 200 nm to 230 nm); (b)-(e) corresponding electric field spatial profiles for both ED and MD; D = 800 nm, w = 200 nm.

Wider gaps, while maintaining the diameter constant, translate into longer periods (distance between neighbouring discs), which contributes to shifting the resonances to longer wavelengths. Figure 56a attests to this, and adds information regarding, once again, resonance responsiveness to this particular brand of geometrical reconfiguration: the ED mode turns out to be more sensitive. This can, as well as in the case of varying thickness, be ascribed to the larger modal volume of this mode. For w = 220 nm, the resonance associated with the ED mode is virtually dissolved, and Figure 56d,e corroborate this idea that only the resonance linked to the MD mode survives by showing very similar field profiles, typically identified with this mode.

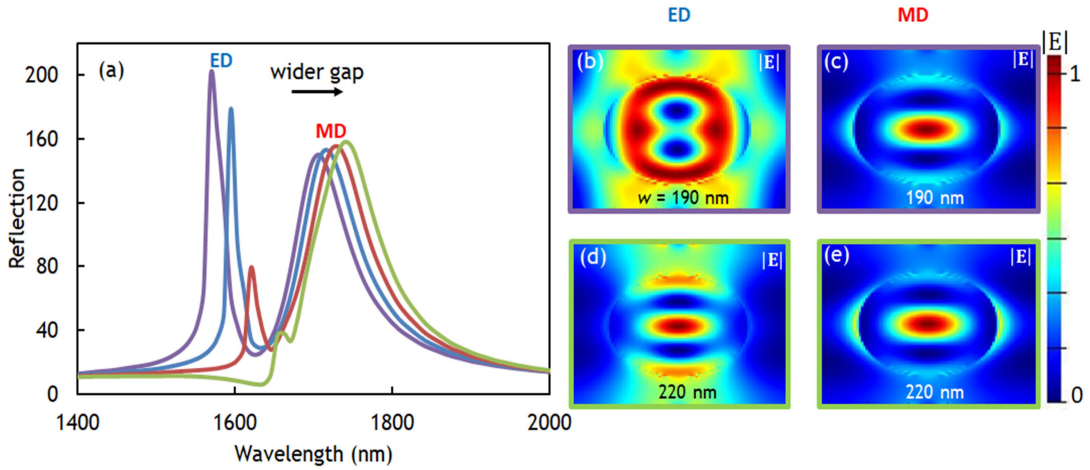


Figure 56 - (a) Reflection spectra of arrays of nanodiscs, made out of a non-dispersive dielectric material with RI = 3.5 and κ = 0.0, with varying w (from 190 nm to 220 nm); (b)-(e) corresponding electric field spatial profiles for both ED and MD; D = 800 nm, t = 220 nm.

6.3. Experiments

Designing phase-change Huygens´ metasurfaces based on chalcogenide materials such as GST, whose refractive index can be controlled by promoting structural phase transitions, can provide a relevant solution for broadening the range of strategies used in order to dynamically reconfigure the optical response of these metasurfaces. Across the near-infrared range, a band of indisputable relevance in telecommunications, the parameters that characterise the optical response of GST in the amorphous phase, namely the real part of its refractive index and extinction coefficient, exhibit a moderately dispersive behaviour, with losses as low as $\kappa \sim 0.006$ accompanied by a high refractive index $n \sim 3.5$ (in the 1550-nm region). This particular set of attributes makes this chalcogenide material a top contender for integration in light-modulating devices designed to be embedded in optical-fibre platforms. The specific spectral profile associated with the metamaterial structures being studied, characterised by the presence of a resonant feature in an otherwise flat reflection spectrum, suits our primary goal of efficiently modulating light, ensuring that a spectral shift of these reflection peaks, induced by the structural phase transitions previously alluded to, could lead to improved switching ratios.

To this end, GST films with a thickness of 220 nm are deposited on a flat glass substrate by RF sputtering (Kurt J. Lesker Nano 38). A base pressure of $2x10^{-4}$ mbar is achieved prior to deposition and high-purity argon is used as the sputtering gas (70 ccpm to strike, 37 ccpm to maintain the plasma). The substrate is held within 10 K of room temperature on a rotating platen 150 mm from the target to produce low-stress amorphous as-deposited films. Huygens´ metasurfaces based on GST nanodiscs, as presented in Figure 57b, with a fixed spacing between neighbouring discs $w \sim 200$ nm and disc diameters D varying from 550 nm to 950 nm, each covering an area of approximately 30 μm × 30 μm, are etched through the GST layer by FIB milling. The normal-incidence reflection and transmission characteristics of these structures were subsequently measured using a microspectrophotometer (CRAIC QDI2010) with a sampling domain size of 15 μm × 15 μm. Figure 57a presents the obtained reflection and transmission spectra, measured using linearly polarised light to illuminate the arrays. Two orthogonal polarisation states are tested, in order to investigate the polarisation-tolerant performance of the nanodiscs, revealing either vertical or horizontal polarisation states yield similar spectral features, both in reflection and in transmission. Our experimental measurements show good agreement with the numerically predicted spectral position of the resonances associated with the nanodiscs array. In addition, these spectral features respond to changes in D as predicted by our model, i.e. larger discs lead to a redshift in the resonance spectral position. Consequently, covering a wide wavelength band in the near-infrared range,

shown in our case to exceed 500 nm, by adjusting the disc diameter and tuning the resonance spectral location, is possible. The exact value of D for which ED mode extinction takes place (D_{ext}) is not easily determined experimentally given the broad profile of our resonances, attributable to fabrication imperfections resulting in poorer quality factors than those registered in our simulations. Nevertheless, an estimate for the value of D_{ext} can still be produced: as D decreases from 950 nm down to 670 nm, the spectral profile changes from a scenario where two resonances can be identified, to one where only one is visible, placing the value of D_{ext} somewhere between 950 and 670 nm. An even finer estimate can be attempted by noting that, for D = 800 nm, a second resonance seems to be jutting out of the main body of the spectral feature, meaning resonance extinction is about to be achieved, pending further reduction of D, placing the value of D_{ext} somewhere between 800 and 670 nm.

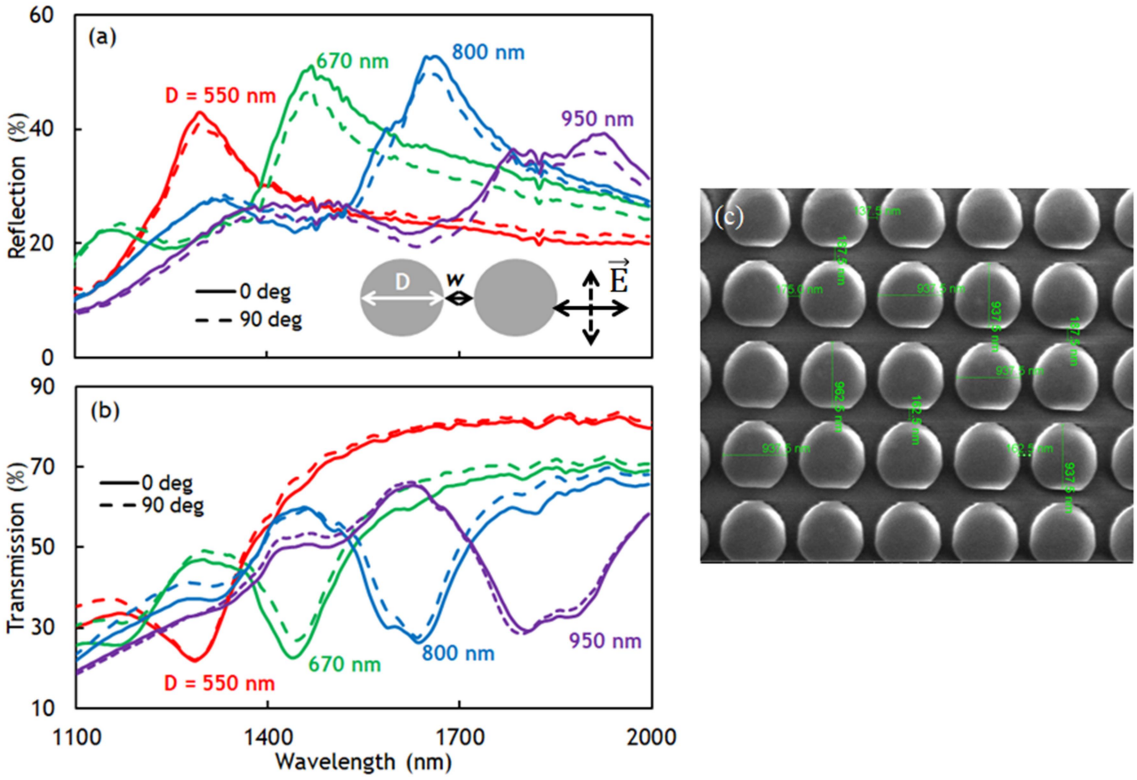


Figure 57 – (a) Reflection and (b) transmission spectra of arrays of GST nanodiscs with D = 550 nm, 670 nm, 800 nm, 950 nm, for two orthogonal polarisation states; SEM picture of an array of nanodiscs with D = 950 nm; w = 200 nm, t = 220 nm.

To assess the performance of our device as an all-optical switch based on a phase-change material, the whole array is crystallised using the same laser-assisted setup described for crystallisation of arrays of GST cubes on flat glass substrates. Optical microscope pictures,

taken in reflection mode, show an array composed of discs with D = 950 nm before and after crystallisation: a slightly brighter GST layer after crystallisation is in line with higher reflectivity in the crystalline phase. The spectral changes in the reflection and transmission spectra resulting from the crystallisation of the nanostructured GST layer are presented in Figure 59. Both sets of curves clearly display the expected trend linked to the increase in the real part of the refractive index of the GST layer brought about by crystallisation, redshifting all the resonant features, by as much as 130 nm. Higher losses in the new structural phase achieved after laser irradiation account for the lower reflection and transmission levels.

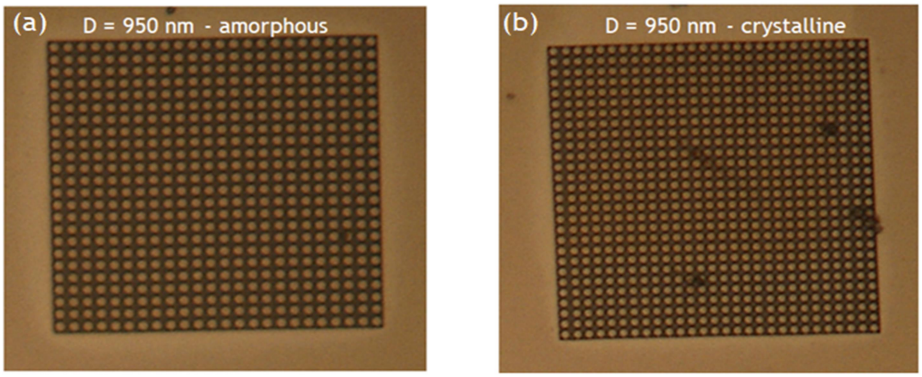


Figure 58 - Optical microscope pictures of an array of GST discs with D = 950 nm, w = 200 nm, t = 220 nm, in the (a) amorphous and (b) crystalline states.

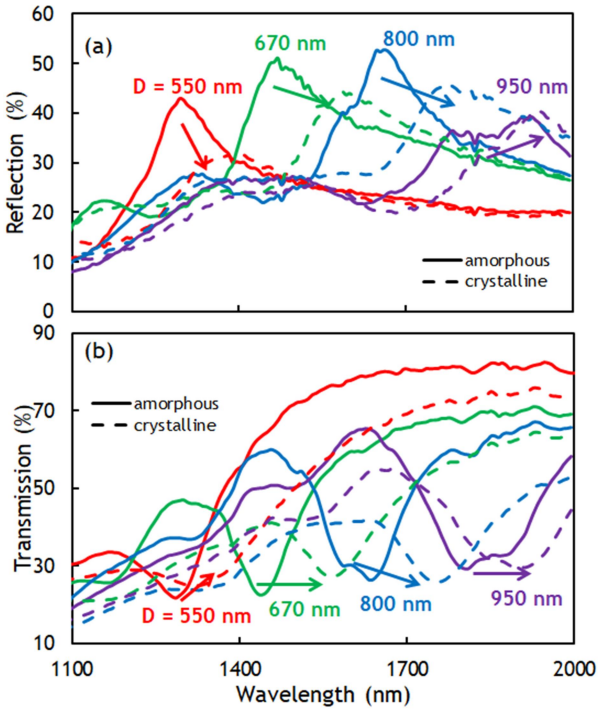


Figure 59 - (a) Reflection and (b) transmission spectra of arrays of GST nanodiscs with D = 550 nm, 670 nm, 800 nm, 950 nm, for two structural phases; Arrows illustrate how the resonances shift upon crystallisation; w = 200 nm, t = 220 nm.

These spectral shifts are congruent with partial crystallisation of the GST layer, an observation backed by our simulation results, featured in Figure 60. The best agreement between experiments and numerical simulations, in the case of an array with D = 550 nm, is achieved when considering the nanostructured layer to be made out of a non-dispersive dielectric material with n = 4.0 and κ = 0.3, rather than composed of fully crystallised dispersive GST. This fact can be attributable to Ga implantation. The higher extinction coefficient associated with crystallised GST explains the noticeable decrease in the average reflected and transmitted power. Field maps featuring electric and magnetic field norm support these observations, showcasing less intense fields in the partially crystalline phase.

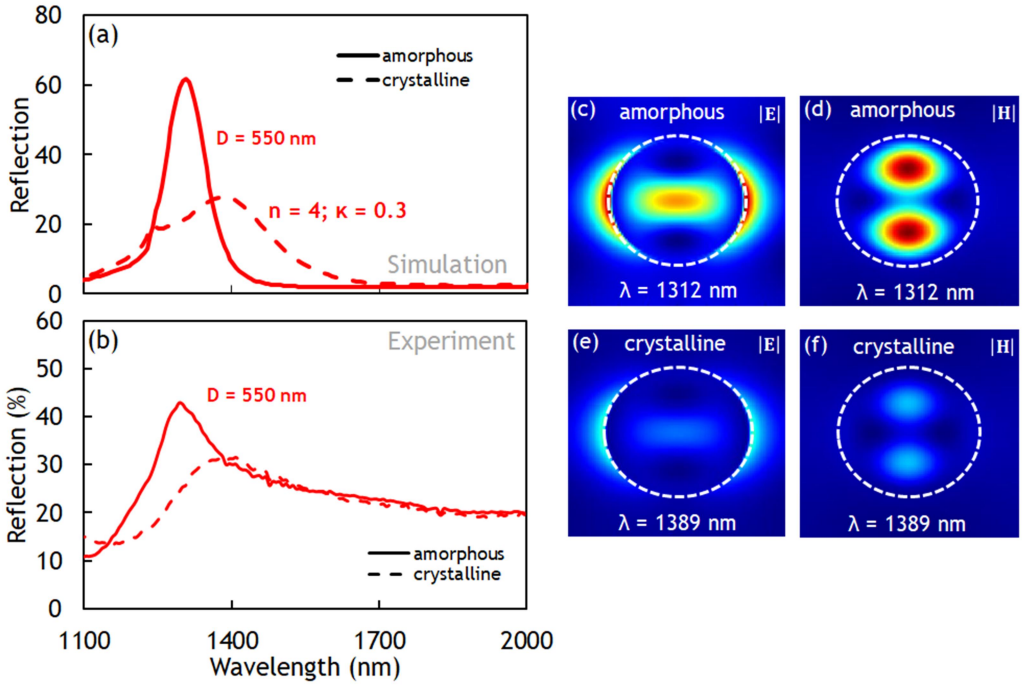


Figure 60 - (a) Simulated and (b) experimentally measured reflection spectra of an array of GST nanodiscs with D = 550 nm, w = 200 nm, t = 220 nm, for two structural phases; (c)-(f) filed maps showing both electric and magnetic field norm in the amorphous and crystalline phases, at resonance (MD).

Transmission and reflection modulation ratios (calculated as amorphous over crystalline), based on experimental results, are plotted in Figure 61. The maximum transmission ratio, equal to 2, is obtained for an array with D = 670 nm; the maximum reflection ratio, equal to 2.2, is obtained for an array with D = 800 nm. For each set of geometrical parameters, maximum modulation occurs in the vicinity of the spectral region where the resonance is located. This is explained by the induced redshift: near the resonance and upon crystallisation, the scenario changes from either high to low reflection or from high to low transmission, yielding intensity modulation. As a consequence, the spectral profiles of modulation ratios can be engineered by

tuning D. These modulation ratios depend, as patent in Figure 61, on the value of D. The contrast between reflection or transmission in the amorphous and crystalline states depends on a variety of aspects, from fringe visibility, contingent on fabrication quality, as well as on the employed crystallisation routine, which does not guarantee light-induced transitions are exactly the same for all the arrays (each array is crystallised individually).

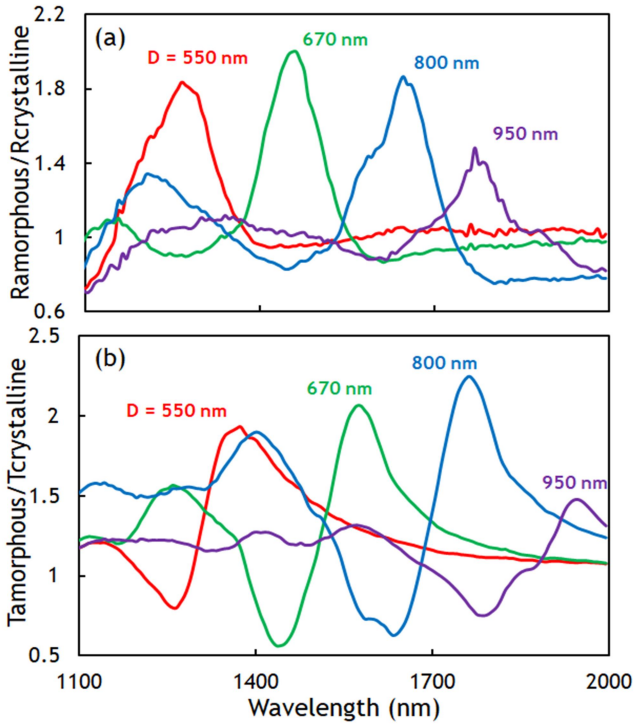


Figure 61 - (a) Reflection and (b) transmission modulation spectra of arrays of GST nanodiscs with D = 550 nm, 670 nm, 800 nm, 950 nm; w = 200 nm, t = 220 nm.

6.4. Conclusion

In conclusion, we propose the realisation of phase-change Huygens' metasurfaces relying on arrays of GST nanodiscs. The inclusion of this chalcogenide material paves the way for all-optical, non-volatile switching of the spectral features supported by our structures, bolstering switching ratios of up to 2.2. The spectral reconfiguration brought about by laser-induced crystallisation of the nanostructured GST layer is substantial, promoting wavelength shifts of up to 130 nm. The spectral profile of the switching contrast can also be tailored by appropriately adjusting the metamaterial geometry, allowing covering a wide wavelength band, stretching more than 500 nm in the near-infrared region. In addition, the metamolecule design enables polarisation-tolerant performance, a relevant attribute when considering the possibility of merging reconfigurable metamaterials with well-established light-guiding platforms, such as optical fibres, in which polarisation control is a delicate and complex task. Designing polarisation-insensitive light-modulating architectures such as the one proposed in this work is a crucial step in guaranteeing a place for fibre-integrated metamaterials in future telecommunication networks.

Furthermore, this concept is transferrable to other spectral bands through using different chalcogenide alloys. Our simulation results demonstrate that, when employing low-loss higher-index dielectric materials, phase-change Huygens' metasurfaces can operate above 2 μm, exhibiting ED and MD modes considerably more spectrally separated than in the particular case of the metasurfaces explored in this work, allowing these resonances to be unequivocally identified in experimental measurements.

7. High Q-factor double-period gratings

7.1. Introduction

Enhancing the Q-factor of resonances resulting from interaction between light and nanostructured media is attainable via the fabrication of double-period gratings[185]. High Q-factors are sought out for specific applications, including notch filters and harmonic generation.

In this section, the origin of Q-factor enhancement in a GST double-period grating is studied, probing the modes excited through the breaking of the translation symmetry of a conventional grating: this asymmetry induces Fano resonances, typically sharper than ordinary dielectric resonances. The impact of varying the values of the geometrical parameters of the double-period grating, namely GST film thickness, degree of asymmetry and gap width, on both the Q-factor of resonances as well as their spectral position, is numerically investigated. Phase modulation and dispersion control using these structures is also proposed.

7.2. Simulations

Simulations are run using a finite element numerical solver (COMSOL). The model assumes a lossless non-dispersive silica substrate with refractive index of 1.45 and uses ellipsometrically measured values of the complex permittivity of GST, as presented in Figure 11a. In addition, normal-incidence illumination using a plane-wave is considered. The electric field is set perpendicular to the direction of propagation. Light incidence upon the modelled structure is determined by the specifications of the two periodic ports, which allow choosing whether light travels from port 1 to port 2 or the other way around, the input power, angle of incidence and refractive index of the medium where the port is. By virtue of periodic boundary conditions, implemented using Floquet periodicity, an infinite array along the x direction is simulated. Throughout the numerical study of the interaction between this metamaterial design, based on a GST double-period grating, and electromagnetic radiation, several parameters have been swept, namely those characterising geometrical features, such as asymmetry $\alpha = 1 - (d_2/d_1)$, where d_1 and d_2 are the widths of the largest and smallest GST blocks, respectively, as well as GST film thickness t and gap width w. The impact of these modifications on transmission, reflection and absorption spectra, are evaluated in the following. Electric field maps which help clarify the nature of the modes at play are also inspected. All simulation results concern amorphous GST.

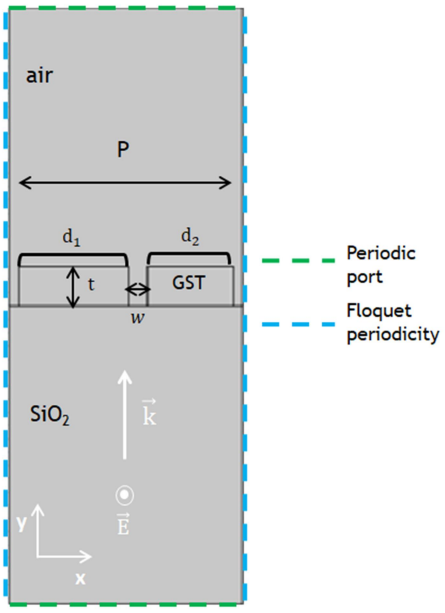


Figure 62 - 2D schematic diagram showing the COMSOL-modelled geometry, materials and configuration of the interaction between light and metamaterial structure; periodic input and output ports are considered, along with periodic boundary conditions.

As soon as conventional grating translation symmetry, associated with a single unit vector $\vec{u} = (d + w)\vec{e_x}$ ($d_1 = d_2 = d$), is broken, by considering $d_1 \neq d_2$, a sharper resonance, with an asymmetric spectral profile, is introduced in the transmission spectrum, in addition to the pre-existent feature linked to a grating with a single translation invariance, located at shorter wavelength. The new resonance is characterised by a higher Q-factor, visually patent in its narrower profile, and is redshifted relative to the pre-existent one. From this point on, bearing in mind the disparity between the corresponding Q-factors (from ~ 15 all the way up to ~ 200, and possibly higher as will be seen further ahead) the resonance at shorter wavelength is designated as low-Q resonance whereas the feature at longer wavelength is labelled high-Q resonance. Figure 63 shows that as α varies from 0 (symmetric grating with $d_1 = d_2 = 710$ nm) to 0.39 (highly asymmetric grating with $d_2 = d_1(1-\alpha) = 539.6$ nm), the low-Q resonance is redshifted while the other one is blueshifted, the former by as much as 40 nm and the latter by more than 120 nm. It becomes apparent by observing the spectra in Figure 63 that the high-Q resonance is more sensitive, both in respect to its resonant wavelength and Q-factor, to variations in α. These results concern a structure with t = 300 nm and w = 140 nm. In order to obtain the subsequent spectra up to Figure 64, α is varied between 0 and 0.39 (each α corresponds to the same pairing of d_1 and d_2)[4]. Analysing the z-component of the electric field E_z of both resonances reveals a distinctly different spatial profile: low-Q mode exhibits a more symmetric profile with a single maximum and minimum inside the GST block; high-Q mode displays a clearly asymmetric profile with counter-propagating current density flowing between neighbouring GST blocks, characteristic of a Fano mode.

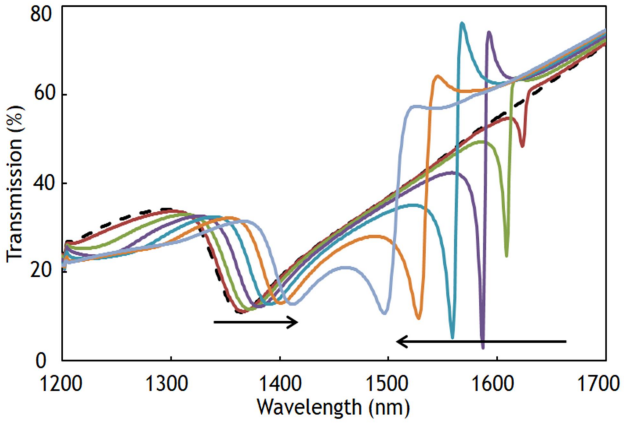


Figure 63 - Transmission spectra for different α; dashed black line shows transmission in a symmetric grating structure; arrows illustrate how the fringes shift when α increases; t = 300 nm, w = 140 nm.

[4] $\alpha = 1 - d_2/d_1$; α is varied by steps corresponding to considering d_2/d_1 = [50/50, 48/52, 46/54, 44/56, 42/58, 40/60, 38/62], with $d_{1,\alpha\neq0} = d_2/d_1 \times d_{1,\alpha=0}$ and $d_{2,\alpha\neq0} = (1 - d_2/d_1) \times d_{2,\alpha=0}$; $d_{1,\alpha=0} = d_{2,\alpha=0} = 710$ nm.

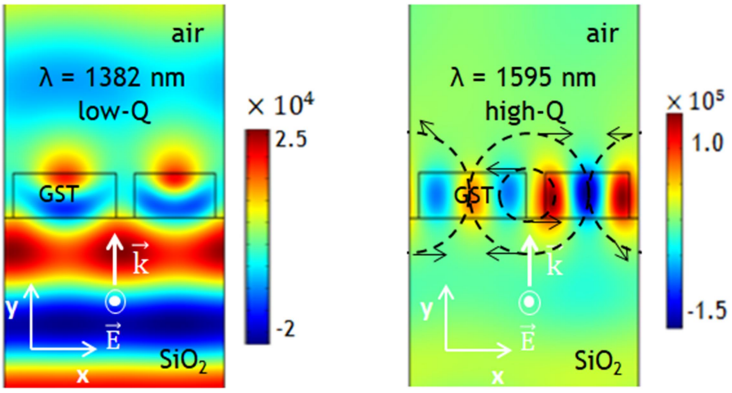


Figure 64 - E_z field maps for α = 0.21; dashed circular lines and arrows identify the current density flow; t = 300 nm, w = 140 nm.

Reflection and absorption spectra, taken for the same structure and for the same values of α, show similar trends to transmission, regarding Q-factor and resonant wavelength evolution as the asymmetry changes.

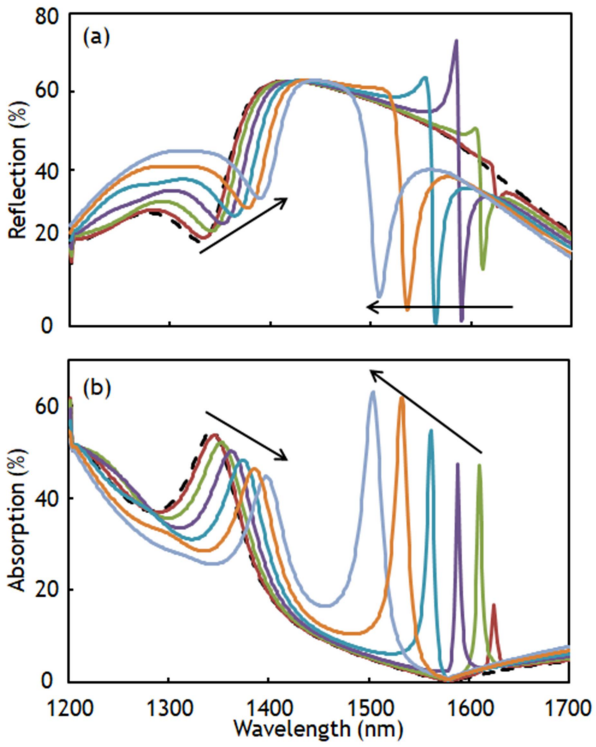


Figure 65 - (a) Reflection and (b) absorption spectra for different α; dashed black lines show reflection and absorption in a symmetric grating structure; arrows illustrate how the fringes shift when α increases; t = 300 nm, w = 140 nm.

Considering thinner GST films also produces spectral changes. Simulating thinner films is equivalent to considering a smaller effective refractive index, as perceived by light, leading to a shift of all resonances to shorter wavelengths, relative to t = 300 nm, being the low-Q resonance more sensitive to this type of geometric modification. Figure 66 displays how the

transmission spectra change as a result of choosing different α, in the case of t = 270 nm and t = 250 nm. Table 2 summarises how the resonant wavelength changes as a function of t, when α = 0.21 (maximises Q-factor of high-Q resonance).

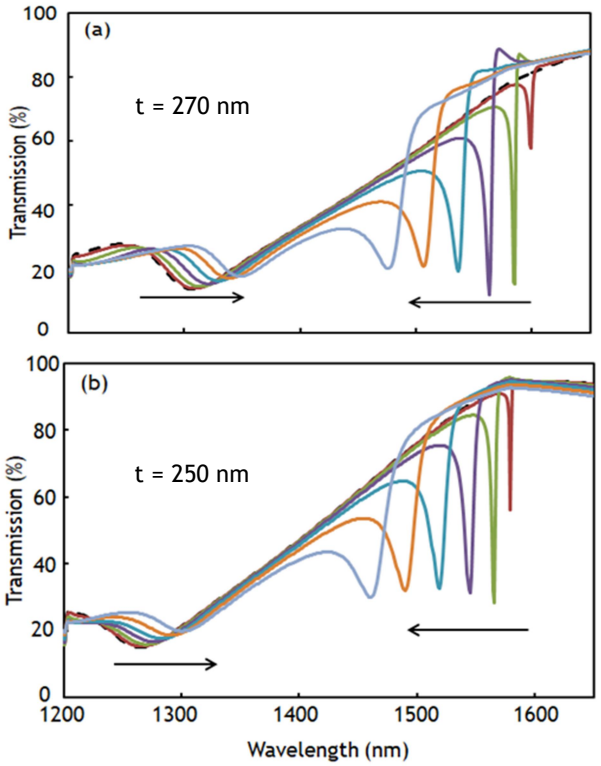


Figure 66 - Transmission spectra for different α when (a) t = 270 nm and (b) = 250 nm; dashed black lines show transmission in a symmetric grating structure; arrows illustrate how the fringes shift when α increases; w = 140 nm.

α = 0.21	**$\lambda_{low\text{-}Q}$ (nm)**	**$\lambda_{high\text{-}Q}$ (nm)**
t = 300 nm	1382	1595
t = 270 nm	1322	1558
t = 250 nm	1278	1542

Table 2 - Spectral location of both low- and high-Q resonances for different GST film thickness; α = 0.21, w = 140 nm.

The main goal of fabricating these structures is introducing high-Q resonances in their optical response. Understanding how the Q-factor evolves as a function of α, for different t, helps characterise these double-period gratings more thoroughly. Given the asymmetric profile of the high-Q resonance, Q-factor is calculated using a different formula

$$\text{Q-factor} = \lambda_1 \lambda_2 / 2 \lambda_0 (\lambda_2 - \lambda_1) \quad (18)$$

where λ_1, λ_2 and λ_0 are obtained as shown in the inset of Figure 67. Figure 67 reveals the maximum Q-factor is higher when thinner GST films are simulated. In addition, Q-factor dependence on α also depends on the value of t under consideration. In thinner GST films (t = 250 m), Q-factor decreases monotonically with α. In the case of thicker films, Q-factor is first enhanced by the introduction of asymmetry in the system and then starts decreasing; maximum Q-factor occurs for a gradually higher degree of asymmetry: α = 0.15 and α = 0.21, when t = 270 nm and 300 nm, respectively. The initial increase of the Q-factor is explained by the strengthening of the Fano mode as slightly higher (but still moderate) asymmetry is introduced. The following downward trend is due to the substantial reduction of the size of the smallest GST block (d_2), which pushes the field out to the GST-air interface, hampering the strength of the Fano mode and consequently bringing down the value of the Q-factor. This is also valid as an explanation for the reduction of the Q-factor when t = 250 nm. The reason why monotonicity is only verified in the case of the thinnest film considered can be understood by noting thicker films imply larger volumes to accommodate the Fano mode. Even when reducing the lateral dimension of the smallest block up to a certain point, by increasing the asymmetry, the resonant mode is still adequately confined inside the GST block. When t = 270 nm or t = 300 nm, asymmetry can be taken up to around 0.15 and 0.21, respectively, and still entail an improved Q-factor, given the gradually larger modal volume available as the film becomes thicker.

As noted before, thinner GST films yield higher maximum Q-factors. Reaching maximum Fano resonance strength can be seen as a balancing act between guaranteeing light does not leak out of the GST block and making sure its intensity within the block is high enough by assigning the appropriate size to the GST grating blocks. Figure 64 illustrates eloquently that light in the smallest GST block is more intense than in the largest one, albeit still reasonably confined to the block. Thinner films can help improve this tight confinement, pending the choice of an asymmetry degree low enough to avoid light escaping from the block into the surrounding environment. This strong light trapping, made easier, for specific asymmetry degrees, by thinner films, leads to higher Q-factors.

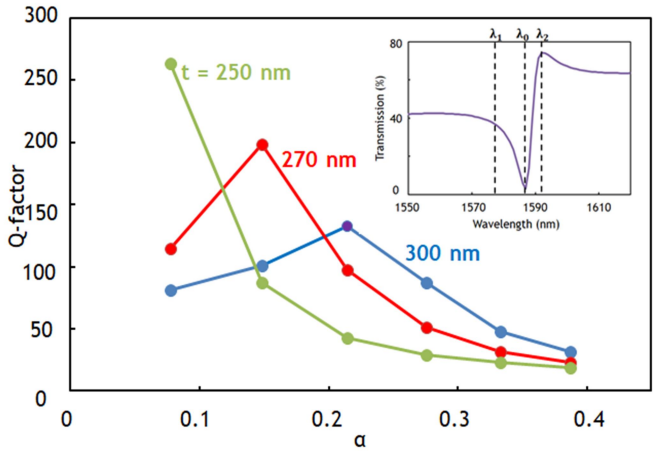


Figure 67 - Q-factor as a function of the asymmetry α for GST films with different thickness (250 nm, 270 nm, 300 nm); inset: transmission in the case of α = 0.21, t = 300 nm, w =140 nm.

Changing w constitutes an alternative route to tailoring the spectral response of these double-period gratings. Figure 68 features the Fano resonance spectral profile for different values of w: as the gap narrows down, while keeping $P = d_1 + d_2 + 2w$ constant, more GST sits on top of the silica substrate, making the effective index of the surrounding environment higher and shifting the resonance to longer wavelengths; narrower gaps also enhance interaction between neighbouring blocks, improving the Q-factor.

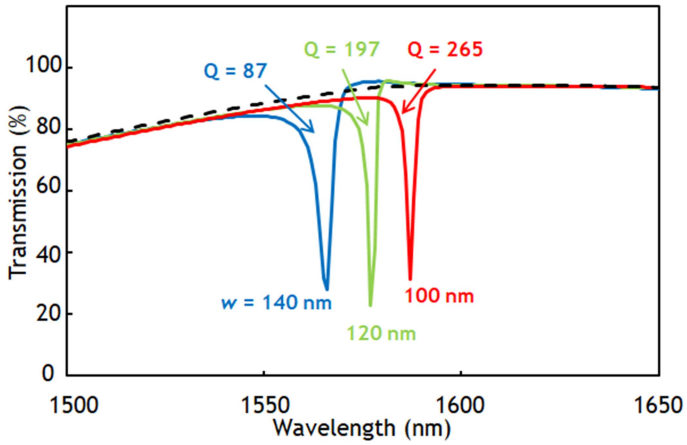


Figure 68 - Transmission spectra as the gap width *w* changes; dashed black line shows transmission in a symmetric grating structure; α = 0.15, t = 250 nm.

Phase modulation accompanies transmission modulation. Figure 69 corroborates this observation: both low- and high-Q phase resonances are introduced, in the same spectral position as the transmission features. The same trends linked to spectral changes brought about by varying α are registered for both phase and transmission.

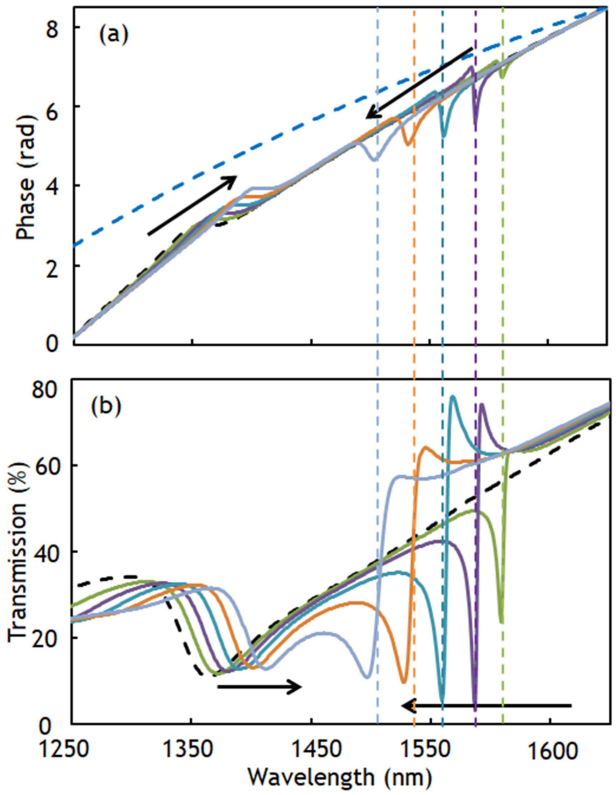


Figure 69 – (a) Phase and (b) transmission spectra as α changes; black dashed lines show phase and transmission in a symmetric grating structure; blue dashed line shows phase in air; arrows illustrate how the fringes shift when α increases; t = 300 nm, w = 140 nm.

Group velocity dispersion (GVD) is calculated for α = 0.21, t = 300 nm and w = 140 nm. Figure 70 shows transmission and GVD spectral profiles for both resonances. These structures make both positive and negative GVD available, thus allowing for normal and anomalous dispersion compensation to be performed. Given the much higher Q-factor of the Fano resonance, maximum GVD associated with this mode is 384[5] times higher than maximum GVD in the vicinity of the low-Q resonance.

5 $\left|\frac{GVD_{high-\ ;max}}{GVD_{low-Q;max}}\right| = \frac{1.5\times10^{-13}}{3.9\times10^{-16}} = 384$

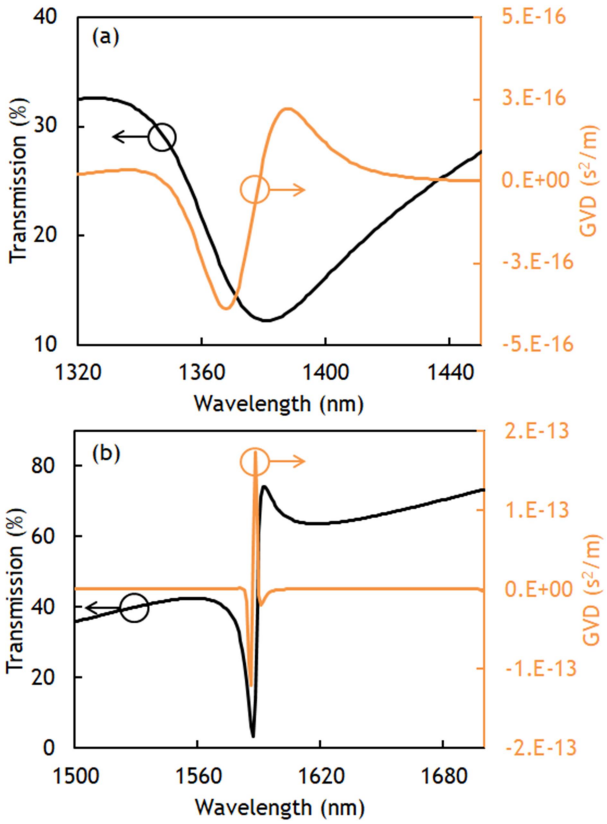


Figure 70 - Dispersion profiles (orange) for the (a) low-Q and (b) high-Q resonances; transmission (black) is also displayed; $\alpha = 0.21$, $t = 300$ nm, $w = 140$ nm.

7.3. Conclusion

The simulation results included in this section validate the hypothesis stated in the introduction, inspired by previously published work: high-Q resonances can be introduced in the spectral response of GST structured media by breaking their underlying symmetry. In the particular case of gratings, the conventional translation symmetry associated with a single unit vector can be broken by simply designing double-period gratings. These structures are made out of a high-index chalcogenide material and, besides fostering the typical low-Q dielectric resonances associated with one-period gratings, also promote strong Fano resonances, typically characterised by very high Q-factors. Spectral tuning of both these resonances can be achieved by changing GST film thickness, degree of asymmetry and the width of the grating lines. Assessing how the Q-factor evolves as a function of the asymmetry for different film thicknesses helps shed some light on the peculiarities of this Fano resonance, revealing that the highest Q-factors are attained for specific degrees of asymmetry which depend on how thick the GST film is. A trend pointing to higher maximum Q-factors as thinner films are considered is identified, at least within the range of thicknesses tested (250 – 300 nm). Phase modulation is also possible resorting to these double-period gratings and dispersion control is shown to include both normal and anomalous cases, near the resonances. Maximum absolute dispersion in the vicinity of the Fano resonance is almost 400 times higher than the value obtained close to the low-Q resonance.

9. Final Remarks

Summing up and judging the merits of one´s own work of four years conjures up a dimension of self-criticism where past shortcomings and insufficiencies are seen in a wider perspective, one framed by the immense privilege of being allowed time to insistently meditate over what could have been done differently, time to repeatedly dwell upon what specific aspects could have been improved, time to attempt answering the dreaded question "was it worthwhile?". Even though this last question is usually the prelude to anguished musing, and by virtue of that a little beyond the scope of what the corollary to a scientific work should be, I still set myself the task, over the next few lines, of addressing the more substantial accomplishments of this project and the work that lies ahead.

The original and preeminent goal of this PhD work concerned the design and fabrication of fibre-coupled devices based on phase-change materials for light modulation. Bearing in mind the constraints associated with thin film deposition and possible subsequent structuring employing an FIB, as well as the inevitable need to bring the light-modulating medium within close proximity to the region of the fibre where light is guided through, cleaved fibre tips and side-polished fibres became the obvious solutions in this pursuit.

Structured GST films integrated with a cleaved fibre tip constituted the first successful shot at trying to implement fibre-based, chalcogenide-supported light modulation. Besides the ability to modulate light intensity, these devices showed good potential when it comes to dispersion compensation in optical fibres, a priceless feature in modern telecommunications. The versatility of the design, allowing control over the spectral position of the resonance via geometrical tuning, ensures the resonant behaviour associated with the periodic structure etched into the GST layer can be located anywhere within the wavelength range of interest in optical fibre communication technology (between 1300 nm and 1650 nm). The Q-factor is also a tunable feature, leading to deeper or shallower modulation depths. Transmission contrast ratios compatible with current requirements in optical switching and data processing networks were obtained.

Merging chalcogenide layers with side-polished fibres entails compelling advantages when compared to fibre tips: reduced losses, owing to the fact light-matter interaction is no longer prompted by intercepting the propagation path of light with the active chalcogenide medium but rather by placing it on top of the polished plane within close proximity to the fibre core (within the decay length of the propagating field outside the core); longer interaction length, potentially several millimetres long, leading to higher modulation ratios. In addition, the particular configuration explored in this instance yields resonant behaviour without the need to structure the GST film, simply by favouring coupling between modes supported by the waveguide as a result of the presence of a high-index thick film, placed very close to the fibre

core. Once more, the characteristics of the resonant feature can be tailored by adjusting the values of the geometrical parameters, enabling device operation across all relevant bands in telecommunications. Technologically-relevant contrast ratios were also obtained.

Expanding this concept of light-modulation resting on phase-change metamaterials to different geometries, other than the one adopted in the case of the fibre-tip device, could prove helpful in unravelling interesting results. Huygens´ metasurfaces made out of GST nanodiscs were considered. The optical response of these structures exhibits the typical traits associated with all-dielectric scatterers of this kind: double-feature resonant behaviour, linked to electric and magnetic dipole modes, whose spectral position is tunable; differing sensitivity of each mode to changes in the geometry of the array and variations of the refractive index of the constitutive material, bringing about spectral mode crossing and considerable suppression of reflection across the entire spectral range under investigation when modes overlap. Promoting structural phase transitions in these metasurfaces also proved a good mechanism of inducing high transmission and reflection contrast ratios.

The previously described architectures produce respectable Q-factors, but narrower features might be of interest for other applications. To this end, double-period GST gratings were proposed. Fano resonances with Q-factors 5-6 times higher than those attained for the other devices were registered. Dispersion control reaches considerably higher values as a result of this.

The innovative character of this approach, combining phase-change media with optical fibre platforms is a valuable achievement on its own, bringing new light-matter interaction configurations to the fore. In addition, it will find a significant impact on a number of practical applications, from fibre-integrated optical memories, dispersion compensation and sensing schemes, as well as notch filters.

A set of important tasks, which could help either clarify the operation limits of our devices or widen the range of configurations based on the fundamental principle of light modulation based on fibre-integrated phase-change media, still evade completion and could constitute the body of pertinent work to be carried out in the future. Such tasks are:

- Induce grey-scale crystallisation. This is attainable using short pulses with controllable duration and peak power, leading to partial crystallisation of the chalcogenide material, which could, in turn, result in finer control over the spectral reconfiguration brought about by this transition.
- Re-amorphise the crystallised layer and cycle between different structural phases. A short laser pulse with high peak intensity should be enough to deliver sufficient

power to instantly melt the crystallised material and revert the structural phase back to amorphous; cycling between these states (between amorphous and crystalline) would determine the amount of transitions our devices could go through without compromising their operation.

- Transfer polarisation-insensitive structures onto a fibre tip. The specific design of the Huygens metasurfaces fabricated in this project, exhibiting cylindrical symmetry, would make the development of polarisation-insensitive in-fibre modulators possible, which represents an important step towards fully functional fiberised components without the need to account for polarisation-dependent processes.
- Structure the GST film on the side-polished fibre. Preliminary work concerning the refinement of the numerical model implemented to study light propagation in a side-polished fibre is required in order to simulate structured films. Alternatively a simplified configuration could be considered, consisting of light shining laterally on the unit cell, essentially disregarding, at an early stage of our investigation, the problem of light coupling from the core mode to the structured region. As was the case of all devices studied in this project, these simulation results will provide a certain degree of confidence in choosing a given geometry, yielding resonances with the desired spectral position and Q-factor. This patterning of the active layer introduces design freedom and paves the way for potentially improved transmission contrast at the signal wavelength and absorption in GST at the signal wavelength.
- Explore more complex phase modulation. Implementing different metasurface designs entails the generation of distinct wave front shapes, which could be made switchable by use of phase-change materials.
- Investigate ENZ behaviour in fibre-coupled GST metadevices. Such an enterprise would require shifting the operation band from the infrared down to the visible region. Fascinating phenomena, already verified in other configurations, such as enhanced transmission (through tapered fibres, for instance) could be harnessed.
- Study other chalcogenide materials in fiberized configurations such as BiTe, BiSbTe and SbTe.
- Widen the scope of metadevices to include hyperbolic metamaterials, for instance, typically relying on layered stacks of thin films which could be easily deposited on the flat substrates provided by a side-polished fibre.

10. Appendices

Appendix A – Transmission of an array of GST blocks on a fibre tip for different angles of incidence

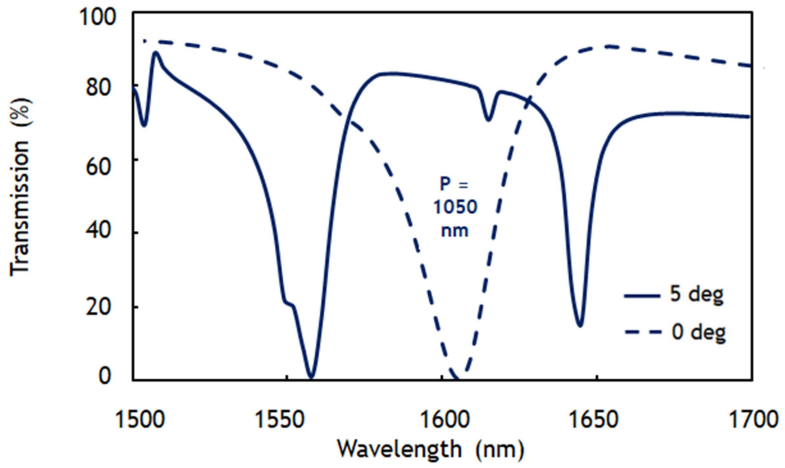


Figure A1 – Simulated transmission spectrum of an array of GST blocks on a fibre tip for different angles of incidence.

Appendix B – FIB-induced crystallisation

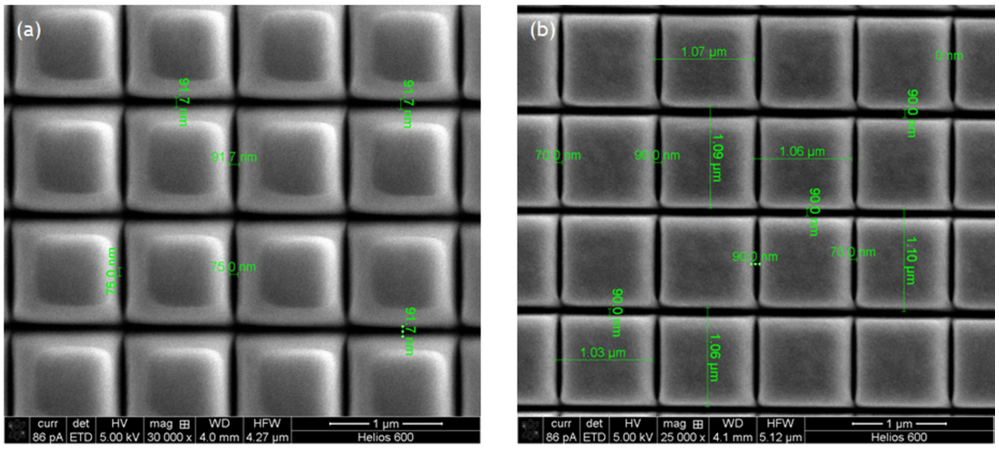


Figure B1 – SEM pictures of arrays of GST blocks fabricated on cleaved fibre tips using an ion beam power of (a) 45 pA and (b) 17 pA.

Appendix C – Transmission normalised to an uncoated fibre tip

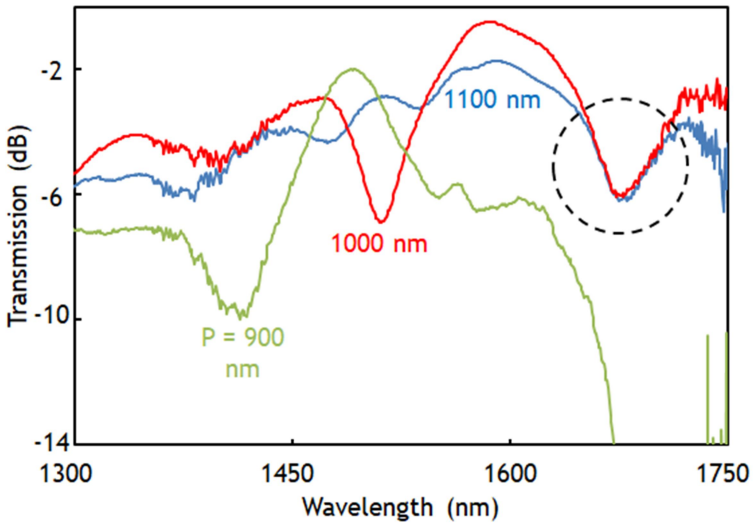


Figure C1 – Transmission spectrum of arrays of GST cubes fabricated on a cleaved fibre-tip, normalised relative to an uncoated fibre tip; P = 900, 1000 and 1100 nm. Dotted circle highlights the spectral feature supported by the unstructured GST film, not attributable to structuring of the chalcogenide layer.

Appendix D – Surveying the adequacy of setting the simulated length of the polished section of a light-modulating device based on a GST-covered side-polished fibre equal to 160 µm

Choosing a polished length l of 160 µm means the model takes into account interaction between light guided through the fibre and the chalcogenide layer over a length close to $120\lambda_{res}$ (λ_{res} = 1336 nm). Simulating polished sections with varying length reveals that a "steady state", where resonant wavelength is independent of l, is only achieved when l = 160 µm (Figures D1 and D2a). The transmission resonance is slightly redshifted upon stretching the polished section from 80 µm up to 160 µm (from 1337 nm to 1348 nm). As expected, the resonance depth becomes more pronounced as a consequence of considering a longer polished section (a cumulative effect takes place; Figure D2b).

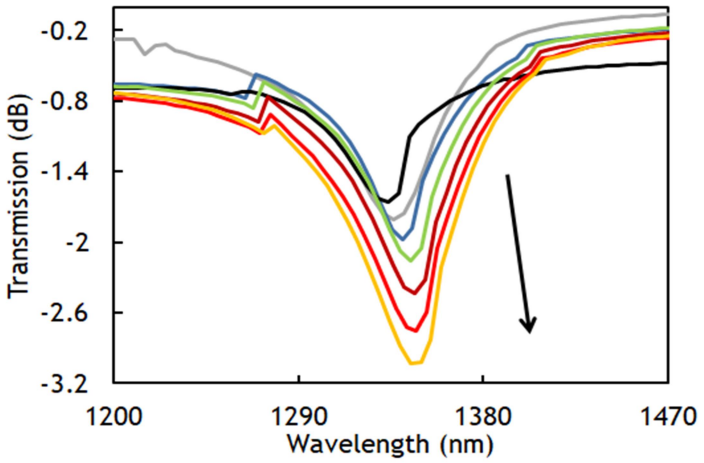


Figure D1 – Simulated transmission spectrum of a GST layer in the amorphous phase for different polished lengths (from 70 μm up to 160 μm); arrow indicates how the resonance evolves as a result of simulating longer polished sections; t = 500 nm; d = 0.5 μm.

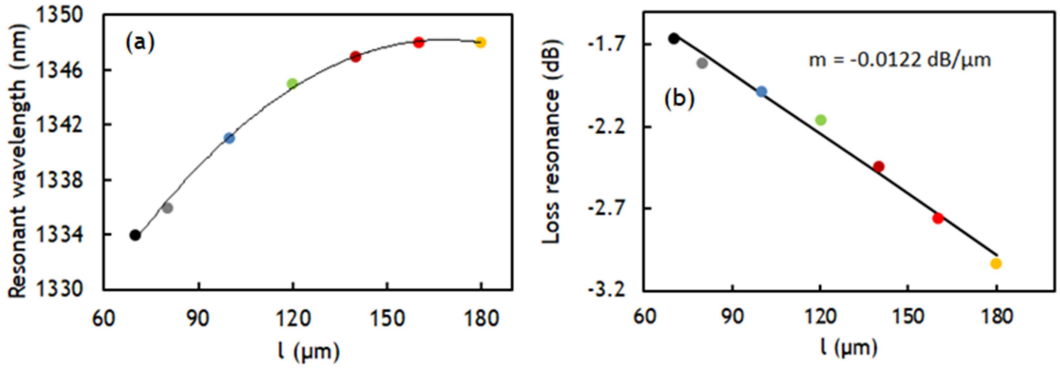


Figure D2 – (a) Resonant wavelength and (b) loss at resonance as functions of the length of the polished section; t = 500 nm; d = 0.5 μm.

The data presented in Figure D2b allow estimating the loss at resonance per unit length of the side-polished section. The value yielded is 0.0122 dB/μm. Establishing a direct correspondence between this simulated value and the experimental scenario would mean an experimental loss at resonance of 0.0122 dB/μm × 5000 μm = 61 dB, which is clearly at odds with the value obtained for the side-polished with the same parameters as those used in the simulations (t = 500 nm; d = 0.5 μm), around 2 dB.

Appendix E – Impact of simulating films with different values of the extinction coefficient κ on the transmission resonance after crystallisation (on a side-polished fibre)

Figure E1 showcases the transmission spectrum of a chalcogenide-based light modulator relying on integration with a side-polished fibre, considering a thick film with RI = 5.85 and variable κ. These simulation results aim at probing the implications of contemplating a scenario in which the specific experimentally induced crystallisation dynamic does not yield a crystallised GST film with the same optical properties as the reference sample (used in the simulations). More concretely, a situation in which the real part of the crystallised GST film is reasonably reproduced in the simulations whilst the extinction coefficient is not is taken into consideration. Simulations reveal that choosing lower κ leads to a transmission resonance with a Q-factor closer to the experimental one.

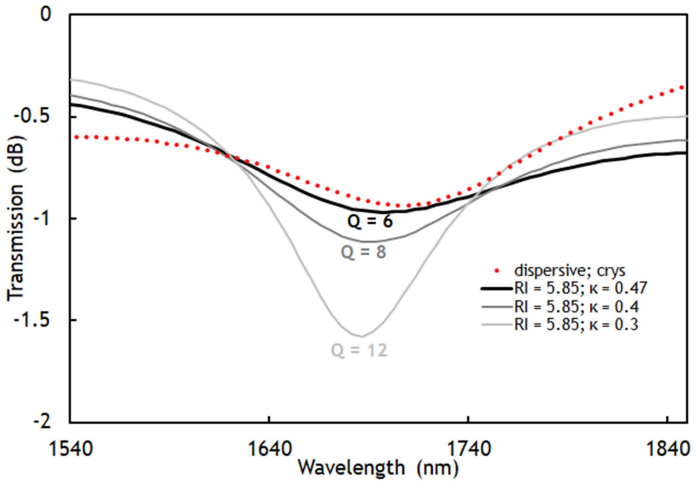


Figure E1 – Simulated transmission spectrum of a non-dispersive GST layer with RI = 5.85 and varying κ; red dotted curve shows transmission of a dispersive GST layer in the crystalline state.

Appendix F – Evanescent field decay length

Light confinement within a fibre core can be characterised by use of a quantity describing light penetration into the cladding layer (penetration depth, d_p), calculated as[186]

$$d_p = \frac{\lambda}{2\pi n_{core}} \left[sin^2\theta_i \frac{n_{core}^2}{n_{clad}^2} - 1 \right]^{-1/2} \quad \text{(F1)}$$

where λ is the operation wavelength, n_{clad} and n_{core} are the refractive indices of the cladding and core materials, and θ_i the angle of incidence at the core/cladding interface. Setting

incidence at very high angles and considering dispersive behaviour for both the refractive indices of the core and cladding materials (as per the inset of Figure F1), d_p exhibits an approximately linear dispersive behaviour in the wavelength range between 1100 nm and 1800 nm. The values of d_p at resonance, in both the amorphous and crystalline states, are 1.74 µm and 2.22 µm.

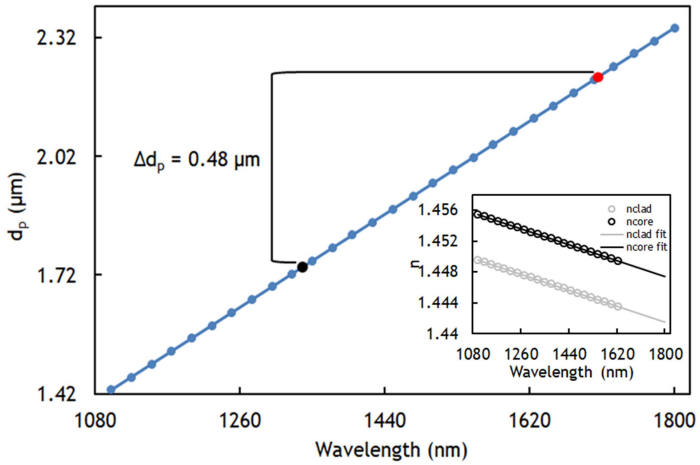


Figure F1 – Dispersive profile of the penetration depth d_p; black and red dots identify the value of d_p, at resonance, in the amorphous and crystalline states; inset: dispersive profile of the refractive indices of the core and cladding materials.

Appendix G – Pseudo-side-polished simulation using high angle of incidence

Given the difficulty of adapting the Lumerical model used to simulate propagation in a side-polished fibre covered with an unstructured thick GST film to study light interaction with a structured active layer, an approximation using a 2D COMSOL model is considered. The modelled geometry features a silica layer on top of which a periodic GST array is placed. Light impinges on the interface between these media at high angles, as Figure G1a shows. The reflection spectrum is taken for different angles of incidence, above the critical angle in a standard optical fibre (~ 85 deg). Reflection in this particular scenario takes into account light reflected back into the silica layer at the silica/GST interface, which would be analogous to taking transmission at the output end of an optical fibre. The limitations of this approach have already been mentioned in the main text (Section 5.4.). Nevertheless, these simulations reveal resonant behaviour can be introduced.

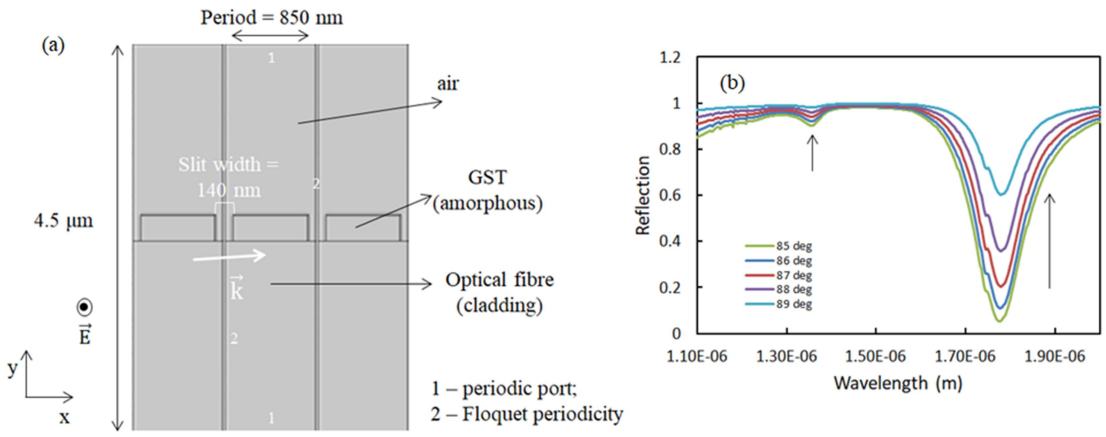


Figure G1 – (a) Schematic diagram of the modelled geometry; (b) reflection spectrum for different angles of incidence.

11. References

1 B. Luk'yanchuk, N. I. Zheludev, S. A. Maier, N. J. Halas, P. Nordlander, H. Giessen, and C. T. Chong, "The Fano resonance in plasmonic nanostructures and metamaterials," Nature Materials **9** (9), 707-715 (2010).

2 M. Wuttig and N. Yamada, "Phase-change materials for rewriteable data storage (vol 6, pg 824, 2007)," Nature Materials **6** (12), 1004-1004 (2007).

3 T. Driscoll, H. T. Kim, B. G. Chae, B. J. Kim, Y. W. Lee, N. M. Jokerst, S. Palit, D. R. Smith, M. Di Ventra, and D. N. Basov, "Memory Metamaterials," Science **325** (5947), 1518-1521 (2009).

4 V. G. Veselago, "Electrodynamics of Substances with Simultaneously Negative Values of Sigma and Mu," Sov Phys Uspekhi **10** (4), 509-& (1968).

5 J. B. Pendry, A. J. Holden, W. J. Stewart, and I. Youngs, "Extremely low frequency plasmons in metallic mesostructures," Physical Review Letters **76** (25), 4773-4776 (1996).

6 J. B. Pendry, A. J. Holden, D. J. Robbins, and W. J. Stewart, "Magnetism from conductors and enhanced nonlinear phenomena," Ieee T Microw Theory **47** (11), 2075-2084 (1999).

7 J. B. Pendry, "Negative refraction makes a perfect lens," Physical Review Letters **85** (18), 3966-3969 (2000).

8 D. R. Smith and N. Kroll, "Negative refractive index in left-handed materials," Physical Review Letters **85** (14), 2933-2936 (2000).

9 W. J. Padilla, M. T. Aronsson, C. Highstrete, M. Lee, A. J. Taylor, and R. D. Averitt, "Electrically resonant terahertz metamaterials: Theoretical and experimental investigations," Phys Rev B **75** (4) (2007).

10 S. Zhang, J. F. Zhou, Y. S. Park, J. Rho, R. Singh, S. Nam, A. K. Azad, H. T. Chen, X. B. Yin, A. J. Taylor, and X. Zhang, "Photoinduced handedness switching in terahertz chiral metamolecules," Nat Commun **3** (2012).

11 M. X. Ren, E. Plum, J. J. Xu, and N. I. Zheludev, "Giant nonlinear optical activity in a plasmonic metamaterial," Nat Commun **3** (2012).

12 S. Zhang, Y. S. Park, J. S. Li, X. C. Lu, W. L. Zhang, and X. Zhang, "Negative Refractive Index in Chiral Metamaterials," Physical Review Letters **102** (2) (2009).

13 E. Plum, J. Zhou, J. Dong, V. A. Fedotov, T. Koschny, C. M. Soukoulis, and N. I. Zheludev, "Metamaterial with negative index due to chirality," Phys Rev B **79** (3) (2009).

14 A. V. Rogacheva, V. A. Fedotov, A. S. Schwanecke, and N. I. Zheludev, "Giant gyrotropy due to electromagnetic-field coupling in a bilayered chiral structure," Physical Review Letters **97** (17) (2006).

15 J. B. Pendry, "A chiral route to negative refraction," Science **306** (5700), 1353-1355 (2004).

16 N. I. Landy, S. Sajuyigbe, J. J. Mock, D. R. Smith, and W. J. Padilla, "Perfect metamaterial absorber," Physical Review Letters **100** (20) (2008).

17 H. Tao, C. M. Bingham, A. C. Strikwerda, D. Pilon, D. Shrekenhamer, N. I. Landy, K. Fan, X. Zhang, W. J. Padilla, and R. D. Averitt, "Highly flexible wide angle of incidence terahertz metamaterial absorber: Design, fabrication, and characterization," Phys Rev B **78** (24) (2008).

18 T. V. Teperik, F. J. G. de Abajo, A. G. Borisov, M. Abdelsalam, P. N. Bartlett, Y. Sugawara, and J. J. Baumberg, "Omnidirectional absorption in nanostructured metal surfaces," Nat Photonics **2** (5), 299-301 (2008).

19 M. Diem, T. Koschny, and C. M. Soukoulis, "Wide-angle perfect absorber/thermal emitter in the terahertz regime," Phys Rev B **79** (3) (2009).

20 C. G. Hu, Z. Y. Zhao, X. N. Chen, and X. G. Luo, "Realizing near-perfect absorption at visible frequencies," Opt Express **17** (13), 11039-11044 (2009).

21 N. Liu, M. Mesch, T. Weiss, M. Hentschel, and H. Giessen, "Infrared Perfect Absorber and Its Application As Plasmonic Sensor," Nano Lett **10** (7), 2342-2348 (2010).

22 X. L. Liu, T. Starr, A. F. Starr, and W. J. Padilla, "Infrared Spatial and Frequency Selective Metamaterial with Near-Unity Absorbance," Physical Review Letters **104** (20) (2010).

23 H. Tao, C. M. Bingham, D. Pilon, K. B. Fan, A. C. Strikwerda, D. Shrekenhamer, W. J. Padilla, X. Zhang, and R. D. Averitt, "A dual band terahertz metamaterial absorber," J Phys D Appl Phys **43** (22) (2010).

24 C. Kurter, P. Tassin, L. Zhang, T. Koschny, A. P. Zhuravel, A. V. Ustinov, S. M. Anlage, and C. M. Soukoulis, "Classical Analogue of Electromagnetically Induced Transparency with a Metal-Superconductor Hybrid Metamaterial," Physical Review Letters **107** (4) (2011).

25 N. Papasimakis, V. A. Fedotov, N. I. Zheludev, and S. L. Prosvirnin, "Metamaterial Analog of Electromagnetically Induced Transparency," Physical Review Letters **101** (25) (2008).

26 P. Tassin, L. Zhang, T. Koschny, E. N. Economou, and C. M. Soukoulis, "Low-Loss Metamaterials Based on Classical Electromagnetically Induced Transparency," Physical Review Letters **102** (5) (2009).

27 S. Zhang, D. A. Genov, Y. Wang, M. Liu, and X. Zhang, "Plasmon-induced transparency in metamaterials," Physical Review Letters **101** (4) (2008).

28 H. T. Chen, W. J. Padilla, J. M. O. Zide, A. C. Gossard, A. J. Taylor, and R. D. Averitt, "Active terahertz metamaterial devices," Nature **444** (7119), 597-600 (2006).

29 W. J. Padilla, A. J. Taylor, C. Highstrete, M. Lee, and R. D. Averitt, "Dynamical electric and magnetic metamaterial response at terahertz frequencies," Physical Review Letters **96** (10) (2006).

30 H. T. Chen, W. J. Padilla, J. M. O. Zide, S. R. Bank, A. C. Gossard, A. J. Taylor, and R. D. Averitt, "Ultrafast optical switching of terahertz metamaterials fabricated on ErAs/GaAs nanoisland superlattices," Opt Lett **32** (12), 1620-1622 (2007).

31 H. T. Chen, J. F. O'Hara, A. K. Azad, A. J. Taylor, R. D. Averitt, D. B. Shrekenhamer, and W. J. Padilla, "Experimental demonstration of frequency-agile terahertz metamaterials," Nat Photonics **2** (5), 295-298 (2008).

32 K. M. Dani, Z. Y. Ku, P. C. Upadhya, R. P. Prasankumar, S. R. J. Brueck, and A. J. Taylor, "Subpicosecond Optical Switching with a Negative Index Metamaterial," Nano Lett **9** (10), 3565-3569 (2009).

33 T. Driscoll, S. Palit, M. M. Qazilbash, M. Brehm, F. Keilmann, B. G. Chae, S. J. Yun, H. T. Kim, S. Y. Cho, N. M. Jokerst, D. R. Smith, and D. N. Basov, "Dynamic tuning of an infrared hybrid-metamaterial resonance using vanadium dioxide," Appl Phys Lett **93** (2) (2008).

34 B. Gholipour, J. F. Zhang, K. F. MacDonald, D. W. Hewak, and N. I. Zheludev, "An All-Optical, Non-volatile, Bidirectional, Phase-Change Meta-Switch," Advanced Materials **25** (22), 3050-3054 (2013).

35 A. Karvounis, B. Gholipour, K. F. MacDonald, and N. I. Zheludev, "All-dielectric phase-change reconfigurable metasurface," Appl Phys Lett **109** (5) (2016).

36 Z. L. Samson, K. F. MacDonald, F. De Angelis, B. Gholipour, K. Knight, C. C. Huang, E. Di Fabrizio, D. W. Hewak, and N. I. Zheludev, "Metamaterial electro-optic switch of nanoscale thickness," Appl Phys Lett **96** (14) (2010).

37 J. F. Zhang, K. F. MacDonald, and N. I. Zheludev, "Controlling light-with-light without nonlinearity," Light-Sci Appl **1** (2012).

38 R. Thijssen, E. Verhagen, T. J. Kippenberg, and A. Polman, "Plasmon Nanomechanical Coupling for Nanoscale Transduction," Nano Lett **13** (7), 3293-3297 (2013).

39 X. Fang, M. L. Tseng, J. Y. Ou, K. F. MacDonald, D. P. Tsai, and N. I. Zheludev, "Ultrafast all-optical switching via coherent modulation of metamaterial absorption," Appl Phys Lett **104** (14) (2014).

40 S. A. Mousavi, E. Plum, J. H. Shi, and N. I. Zheludev, "Coherent control of birefringence and optical activity," Appl Phys Lett **105** (1) (2014).

41 J. H. Shi, X. Fang, E. T. F. Rogers, E. Plum, K. F. MacDonald, and N. I. Zheludev, "Coherent control of Snell's law at metasurfaces," Opt Express **22** (17), 21051-21060 (2014).

42 X. Fang, K. F. MacDonald, E. Plum, and N. I. Zheludev, "Coherent control of light-matter interactions in polarization standing waves," Sci Rep-Uk **6** (2016).

43 V. A. Fedotov, M. Rose, S. L. Prosvirnin, N. Papasimakis, and N. I. Zheludev, "Sharp trapped-mode resonances in planar metamaterials with a broken structural symmetry," Physical Review Letters **99** (14) (2007).

44 M. Silveirinha and N. Engheta, "Tunneling of electromagnetic energy through subwavelength channels and bends using epsilon-near-zero materials," Physical Review Letters **97** (15) (2006).

45 A. Alu, M. G. Silveirinha, A. Salandrino, and N. Engheta, "Epsilon-near-zero metamaterials and electromagnetic sources: Tailoring the radiation phase pattern," Phys Rev B **75** (15) (2007).

46 M. G. Silveirinha and N. Engheta, "Theory of supercoupling, squeezing wave energy, and field confinement in narrow channels and tight bends using epsilon near-zero metamaterials," Phys Rev B **76** (24) (2007).

47 B. Edwards, A. Alu, M. E. Young, M. Silveirinha, and N. Engheta, "Experimental verification of epsilon-near-zero metamaterial coupling and energy squeezing using a microwave waveguide," Physical Review Letters **100** (3) (2008).

48 D. C. Adams, S. Inampudi, T. Ribaudo, D. Slocum, S. Vangala, N. A. Kuhta, W. D. Goodhue, V. A. Podolskiy, and D. Wasserman, "Funneling Light through a Subwavelength Aperture with Epsilon-Near-Zero Materials," Physical Review Letters **107** (13) (2011).

49 C. Argyropoulos, P. Y. Chen, G. D'Aguanno, N. Engheta, and A. Alu, "Boosting optical nonlinearities in epsilon-near-zero plasmonic channels," Phys Rev B **85** (4) (2012).

50 R. Maas, J. Parsons, N. Engheta, and A. Polman, "Experimental realization of an epsilon-near-zero metamaterial at visible wavelengths," Nat Photonics **7** (11), 907-912 (2013).

51 P. Moitra, Y. M. Yang, Z. Anderson, I. I. Kravchenko, D. P. Briggs, and J. Valentine, "Realization of an all-dielectric zero-index optical metamaterial," Nat Photonics **7** (10), 791-795 (2013).

52 E. J. R. Vesseur, T. Coenen, H. Caglayan, N. Engheta, and A. Polman, "Experimental Verification of n=0 Structures for Visible Light," Physical Review Letters **110** (1) (2013).

53 I. Liberal and N. Engheta, "Near-zero refractive index photonics (vol 11, pg 149, 2017)," Nat Photonics **11** (4), 264-264 (2017).

54 D. Piccinotti, B. Gholipour, J. Yao, K. F. MacDonald, B. E. Hayden, and N. I. Zheludev, "Optical Response of Nanohole Arrays Filled with Chalcogenide Low-Epsilon Media," Adv Opt Mater **6** (22) (2018).

55 K. J. Boller, A. Imamoglu, and S. E. Harris, "Observation of Electromagnetically Induced Transparency," Physical Review Letters **66** (20), 2593-2596 (1991).

56 F. Liu, L. Xiao, Y. Ye, M. X. Wang, K. Y. Cui, X. Feng, W. Zhang, and Y. D. Huang, "Integrated Cherenkov radiation emitter eliminating the electron velocity threshold," Nat Photonics **11** (5), 289-+ (2017).

57 A. Poddubny, I. Iorsh, P. Belov, and Y. Kivshar, "Hyperbolic metamaterials," Nat Photonics **7** (12), 948-957 (2013).

58 J. Y. Ou, J. K. So, G. Adamo, A. Sulaev, L. Wang, and N. I. Zheludev, "Ultraviolet and visible range plasmonics in the topological insulator Bi1.5Sb0.5Te1.8Se1.2," Nat Commun **5** (2014).

59 W. S. Whitney, V. W. Brar, Y. Ou, Y. Shao, A. R. Davoyan, D. N. Basov, K. He, Q. K. Xue, and H. A. Atwater, "Gate-Variable Mid-Infrared Optical Transitions in a (Bi1-xSbx)2Te3 Topological Insulator," Nano Lett **17** (1), 255-260 (2017).

60 C. L. Kane and E. J. Mele, "Z(2) topological order and the quantum spin Hall effect," Physical Review Letters **95** (14) (2005).

61 F. Pollmann, E. Berg, A. M. Turner, and M. Oshikawa, "Symmetry protection of topological phases in one-dimensional quantum spin systems," Phys Rev B **85** (7) (2012).

62 J. Zhang, K. F. MacDonald, and N. I. Zheludev, "Optical gecko toe: Optically controlled attractive near-field forces between plasmonic metamaterials and dielectric or metal surfaces," Phys Rev B **85** (20) (2012).

63 V. Ginis, P. Tassin, C. M. Soukoulis, and I. Veretennicoff, "Enhancing Optical Gradient Forces with Metamaterials," Physical Review Letters **110** (5) (2013).

64 J. F. Zhang, K. F. MacDonald, and N. I. Zheludev, "Nonlinear dielectric optomechanical metamaterials," Light-Sci Appl **2** (2013).

65 J. F. Zhang, K. F. MacDonald, and N. I. Zheludev, "Giant optical forces in planar dielectric photonic metamaterials," Opt Lett **39** (16), 4883-4886 (2014).

66 A. Pimenov, A. Loidl, P. Przyslupski, and B. Dabrowski, "Negative refraction in ferromagnet-superconductor superlattices," Physical Review Letters **95** (24) (2005).

67 H. T. Chen, H. Yang, R. Singh, J. F. O'Hara, A. K. Azad, S. A. Trugman, Q. X. Jia, and A. J. Taylor, "Tuning the Resonance in High-Temperature Superconducting Terahertz Metamaterials," Physical Review Letters **105** (24) (2010).

68 V. A. Fedotov, A. Tsiatmas, J. H. Shi, R. Buckingham, P. de Groot, Y. Chen, S. Wang, and N. I. Zheludev, "Temperature control of Fano resonances and transmission in superconducting metamaterials," Opt Express **18** (9), 9015-9019 (2010).

69 V. Savinov, V. A. Fedotov, S. M. Anlage, P. A. J. de Groot, and N. I. Zheludev, "Modulating Sub-THz Radiation with Current in Superconducting Metamaterial," Physical Review Letters **109** (24) (2012).

70 A. E. Nikolaenko, F. De Angelis, S. A. Boden, N. Papasimakis, P. Ashburn, E. Di Fabrizio, and N. I. Zheludev, "Carbon Nanotubes in a Photonic Metamaterial," Physical Review Letters **104** (15) (2010).

71 N. Papasimakis, Z. Q. Luo, Z. X. Shen, F. De Angelis, E. Di Fabrizio, A. E. Nikolaenko, and N. I. Zheludev, "Graphene in a photonic metamaterial," Opt Express **18** (8), 8353-8359 (2010).

72 L. Ju, B. S. Geng, J. Horng, C. Girit, M. Martin, Z. Hao, H. A. Bechtel, X. G. Liang, A. Zettl, Y. R. Shen, and F. Wang, "Graphene plasmonics for tunable terahertz metamaterials," Nat Nanotechnol **6** (10), 630-634 (2011).

73 S. H. Lee, M. Choi, T. T. Kim, S. Lee, M. Liu, X. Yin, H. K. Choi, S. S. Lee, C. G. Choi, S. Y. Choi, X. Zhang, and B. Min, "Switching terahertz waves with gate-controlled active graphene metamaterials," Nature Materials **11** (11), 936-941 (2012).

74 A. E. Nikolaenko, N. Papasimakis, E. Atmatzakis, Z. Q. Luo, Z. X. Shen, F. De Angelis, S. A. Boden, E. Di Fabrizio, and N. I. Zheludev, "Nonlinear graphene metamaterial," Appl Phys Lett **100** (18) (2012).

75 N. K. Emani, T. F. Chung, A. V. Kildishev, V. M. Shalaev, Y. P. Chen, and A. Boltasseva, "Electrical modulation of fano resonance in plasmonic nanostructures using graphene," Nano Lett **14** (1), 78-82 (2014).

76 Y. Yao, R. Shankar, M. A. Kats, Y. Song, J. Kong, M. Loncar, and F. Capasso, "Electrically Tunable Metasurface Perfect Absorbers for Ultrathin Mid-Infrared Optical Modulators," Nano Lett **14** (11), 6526-6532 (2014).

77 O. Buchnev, J. Y. Ou, M. Kaczmarek, N. I. Zheludev, and V. A. Fedotov, "Electro-optical control in a plasmonic metamaterial hybridised with a liquid-crystal cell," Opt Express **21** (2), 1633-1638 (2013).

78 A. N. Grigorenko, M. Polini, and K. S. Novoselov, "Graphene plasmonics," Nat Photonics **6** (11), 749-758 (2012).

79 Y. H. Fu, A. Q. Liu, W. M. Zhu, X. M. Zhang, D. P. Tsai, J. B. Zhang, T. Mei, J. F. Tao, H. C. Guo, X. H. Zhang, J. H. Teng, N. I. Zheludev, G. Q. Lo, and D. L. Kwong, "A Micromachined Reconfigurable Metamaterial via Reconfiguration of Asymmetric Split-Ring Resonators," Adv Funct Mater **21** (18), 3589-3594 (2011).

80 W. M. Zhu, A. Q. Liu, X. M. Zhang, D. P. Tsai, T. Bourouina, J. H. Teng, X. H. Zhang, H. C. Guo, H. Tanoto, T. Mei, G. Q. Lo, and D. L. Kwong, "Switchable Magnetic Metamaterials Using Micromachining Processes," Advanced Materials **23** (15), 1792-+ (2011).

81 J. Y. Ou, E. Plum, J. F. Zhang, and N. I. Zheludev, "An electromechanically reconfigurable plasmonic metamaterial operating in the near-infrared," Nat Nanotechnol **8** (4), 252-255 (2013).

82 M. Lapine, D. Powell, M. Gorkunov, I. Shadrivov, R. Marques, and Y. Kivshar, "Structural tunability in metamaterials," Appl Phys Lett **95** (8) (2009).

83 I. M. Pryce, K. Aydin, Y. A. Kelaita, R. M. Briggs, and H. A. Atwater, "Highly Strained Compliant Optical Metamaterials with Large Frequency Tunability," Nano Lett **10** (10), 4222-4227 (2010).

84 H. Tao, A. C. Strikwerda, K. Fan, W. J. Padilla, X. Zhang, and R. D. Averitt, "Reconfigurable Terahertz Metamaterials," Physical Review Letters **103** (14) (2009).

85 J. Y. Ou, E. Plum, L. Jiang, and N. I. Zheludev, "Reconfigurable Photonic Metamaterials," Nano Lett **11** (5), 2142-2144 (2011).

86 M. Lapine, I. V. Shadrivov, D. A. Powell, and Y. S. Kivshar, "Magnetoelastic metamaterials," Nat Mater **11** (1), 30-33 (2011).

87 J. Valente, J. Y. Ou, E. Plum, I. J. Youngs, and N. I. Zheludev, "A magneto-electro-optical effect in a plasmonic nanowire material," Nat Commun **6**, 7021 (2015).

88 M. K. Wu, J. R. Ashburn, C. J. Torng, P. H. Hor, R. L. Meng, L. Gao, Z. J. Huang, Y. Q. Wang, and C. W. Chu, "Superconductivity at 93-K in a New Mixed-Phase Y-Ba-Cu-O Compound System at Ambient Pressure," Physical Review Letters **58** (9), 908-910 (1987).

89 B. Gholipour, D. Piccinotti, A. Karvounis, K. F. MacDonald, and N. I. Zheludev, "Reconfigurable Ultraviolet and High-Energy Visible Dielectric Metamaterials," Nano Lett **19** (3), 1643-1648 (2019).

90 J. K. So, F. J. G. de Abajo, K. F. MacDonald, and N. I. Zheludev, "Amplification of the Evanescent Field of Free Electrons," Acs Photonics **2** (9), 1236-1240 (2015).

91 V. Savinov and N. I. Zheludev, "High-quality metamaterial dispersive grating on the facet of an optical fiber," Appl Phys Lett **111** (9) (2017).

92 A. Xomalis, I. Demirtzioglou, E. Plum, Y. M. Jung, V. Nalla, C. Lacava, K. F. MacDonald, P. Petropoulos, D. J. Richardson, and N. I. Zheludev, "Fibre-optic metadevice for all-optical signal modulation based on coherent absorption," Nat Commun **9** (2018).

93 Y. F. Zhao, J. R. Zhang, J. Du, and J. Wang, "Meta-facet fiber for twisting ultra-broadband light with high phase purity," Appl Phys Lett **113** (6) (2018).

94 Z. Y. Li, M. H. Kim, C. Wang, Z. H. Han, S. Shrestha, A. C. Overvig, M. Lu, A. Stein, A. M. Agarwal, M. Loncar, and N. F. Yu, "Controlling propagation and coupling of waveguide modes using phase-gradient metasurfaces," Nat Nanotechnol **12** (7), 675-+ (2017).

95 C. Wang, Z. Y. Li, M. H. Kim, X. Xiong, X. F. Ren, G. C. Guo, N. F. Yu, and M. Loncar, "Metasurface-assisted phase-matching-free second harmonic generation in lithium niobate waveguides," Nat Commun **8** (2017).

96 Q. L. Bao, H. Zhang, B. Wang, Z. H. Ni, C. H. Y. X. Lim, Y. Wang, D. Y. Tang, and K. P. Loh, "Broadband graphene polarizer," Nat Photonics **5** (7), 411-415 (2011).

97 H. J. Zhang, N. Healy, L. Shen, C. C. Huang, D. W. Hewak, and A. C. Peacock, "Enhanced all-optical modulation in a graphene-coated fibre with low insertion loss," Sci Rep-Uk **6** (2016).

98 H. J. Zhang, N. Healy, A. F. J. Runge, C. C. Huang, D. W. Hewak, and A. C. Peacock, "Optical-resonance-enhanced nonlinearities in a MoS2-coated single-mode fiber," Opt Lett **43** (13), 3100-3103 (2018).

99 X. Y. He, Z. B. Liu, D. N. Wang, M. W. Yang, C. R. Liao, and X. Zhao, "Passively Mode-Locked Fiber Laser Based on Reduced Graphene Oxide on Microfiber for Ultra-Wide-Band Doublet Pulse Generation," J Lightwave Technol **30** (7), 984-989 (2012).

100 Z. B. Liu, M. Feng, W. S. Jiang, W. Xin, P. Wang, Q. W. Sheng, Y. G. Liu, D. N. Wang, W. Y. Zhou, and J. G. Tian, "Broadband all-optical modulation using a graphene-covered-microfiber," Laser Phys Lett **10** (6) (2013).

101 W. Li, B. G. Chen, C. Meng, W. Fang, Y. Xiao, X. Y. Li, Z. F. Hu, Y. X. Xu, L. M. Tong, H. Q. Wang, W. T. Liu, J. M. Bao, and Y. R. Shen, "Ultrafast All-Optical Graphene Modulator," Nano Lett **14** (2), 955-959 (2014).

102 W. H. P. Pernice and H. Bhaskaran, "Photonic non-volatile memories using phase change materials," Appl Phys Lett **101** (17) (2012).

103 M. Rude, J. Pello, R. E. Simpson, J. Osmond, G. Roelkens, J. J. G. M. van der Tol, and V. Pruneri, "Optical switching at 1.55 mu m in silicon racetrack resonators using phase change materials," Appl Phys Lett **103** (14) (2013).

104 C. Rios, M. Stegmaier, P. Hosseini, D. Wang, T. Scherer, C. D. Wright, H. Bhaskaran, and W. H. P. Pernice, "Integrated all-photonic non-volatile multi-level memory," Nat Photonics **9** (11), 725-+ (2015).

105 M. Rude, R. E. Simpson, R. Quidant, V. Pruneri, and J. Renger, "Active Control of Surface Plasmon Waveguides with a Phase Change Material," Acs Photonics **2** (6), 669-674 (2015).

106 H. Y. Zhang, L. J. Zhou, J. Xu, L. J. Lu, J. P. Chen, and B. M. A. Rahman, "All-optical non-volatile tuning of an AMZI-coupled ring resonator with GST phase-change material," Opt Lett **43** (22), 5539-5542 (2018).

107 S. Reyntjens and R. Puers, "A review of focused ion beam applications in microsystem technology," J Micromech Microeng **11** (4), 287-300 (2001).

108 C. A. Volkert and A. M. Minor, "Focused ion beam microscopy and micromachining," Mrs Bull **32** (5), 389-395 (2007).

109 "https://cemas.osu.edu/fei-helios-nanolabtm-600-dualbeam-fibsem".

110 S. Pilevar, K. Edinger, W. Atia, I. Smolyaninov, and C. Davis, "Focused ion-beam fabrication of fiber probes with well-defined apertures for use in near-field scanning optical microscopy," Appl Phys Lett **72** (24), 3133-3135 (1998).

111 A. Naber, D. Molenda, U. C. Fischer, H. J. Maas, C. Hoppener, N. Lu, and H. Fuchs, "Enhanced light confinement in a near-field optical probe with a triangular aperture," Physical Review Letters **89** (21) (2002).

112 L. Wang and X. F. Xu, "High transmission nanoscale bowtie-shaped aperture probe for near-field optical imaging," Appl Phys Lett **90** (26) (2007).

113 F. Renna, D. Cox, and G. Brambilla, "Efficient sub-wavelength light confinement using surface plasmon polaritons in tapered fibers," Opt Express **17** (9), 7658-7663 (2009).

114 J. N. Farahani, D. W. Pohl, H. J. Eisler, and B. Hecht, "Single quantum dot coupled to a scanning optical antenna: A tunable superemitter," Physical Review Letters **95** (1) (2005).

115 D. Iannuzzi, S. Deladi, V. J. Gadgil, R. G. P. Sanders, H. Schreuders, and M. C. Elwenspoek, "Monolithic fiber-top sensor for critical environments and standard applications," Appl Phys Lett **88** (5) (2006).

116 M. Burresi, D. van Oosten, T. Kampfrath, H. Schoenmaker, R. Heideman, A. Leinse, and L. Kuipers, "Probing the Magnetic Field of Light at Optical Frequencies," Science **326** (5952), 550-553 (2009).

117 F. Wang, W. Yuan, O. Hansen, and O. Bang, "Selective filling of photonic crystal fibers using focused ion beam milled microchannels," Opt Express **19** (18), 17585-17590 (2011).

118 R. M. Andre, S. C. Warren-Smith, M. Becker, J. Dellith, M. Rothhardt, M. I. Zibaii, H. Latifi, M. B. Marques, H. Bartelt, and O. Frazao, "Simultaneous measurement of temperature and refractive index using focused ion beam milled Fabry-Perot cavities in optical fiber micro-tips," Opt Express **24** (13), 14053-14065 (2016).

119 R. Janeiro, R. Flores, P. Dahal, and J. Viegas, "Fabrication of a phase photon sieve on an optical fiber tip by focused ion beam nanomachining for improved fiber to silicon photonics waveguide light coupling," Opt Express **24** (11), 1611-1625 (2016).

120 R. S. R. Ribeiro, P. Dahal, A. Guerreiro, P. Jorge, and J. Viegas, "Optical fibers as beam shapers: from Gaussian beams to optical vortices," Opt Lett **41** (10), 2137-2140 (2016).

121 S. Cabrini, C. Liberale, D. Cojoc, A. Carpentiero, M. Prasciolu, S. Mora, V. Degiorgio, F. De Angelis, and E. Di Fabrizio, "Axicon lens on optical fiber forming optical

tweezers, made by focused ion beam milling," Microelectron Eng **83** (4-9), 804-807 (2006).

122 E. T. F. Rogers, J. Lindberg, T. Roy, S. Savo, J. E. Chad, M. R. Dennis, and N. I. Zheludev, "A super-oscillatory lens optical microscope for subwavelength imaging," Nature Materials **11** (5), 432-435 (2012).

123 P. Sigmund, "Mechanisms and Theory of Physical Sputtering by Particle Impact," Nucl Instrum Meth B **27** (1), 1-20 (1987).

124 M. Ohring, *Materials Science of Thin Films*. (Academic Press, 1992), 2nd ed.

125 "http://jciszek.sites.luc.edu/lab.html".

126 B. Q. Wu, A. Kumar, and S. Pamarthy, "High aspect ratio silicon etch: A review," J Appl Phys **108** (5) (2010).

127 F. Marty, L. Rousseau, B. Saadany, B. Mercier, O. Francais, Y. Mita, and T. Bourouina, "Advanced etching of silicon based on deep reactive ion etching for silicon high aspect ratio microstructures and three-dimensional micro- and nanostructures," Microelectron J **36** (7), 673-677 (2005).

128 P. Mukherjee, A. Bruccoleri, R. K. Heilmann, M. L. Schattenburg, A. F. Kaplan, and L. J. Guo, "Plasma etch fabrication of 60:1 aspect ratio silicon nanogratings with 200 nm pitch," J Vac Sci Technol B **28** (6), C6p70-C76p75 (2010).

129 C. D. Hussey and J. D. Minelly, "Optical Fiber Polishing with a Motor-Driven Polishing Wheel," Electron Lett **24** (13), 805-807 (1988).

130 O. G. Leminger and R. Zengerle, "Determination of Single-Mode Fiber Coupler Design Parameters from Loss Measurements," J Lightwave Technol **3** (4), 864-867 (1985).

131 M. H. Chiu, S. F. Wang, and R. S. Chang, "D-type fiber biosensor based on surface-plasmon resonance technology and heterodyne interferometry," Opt Lett **30** (3), 233-235 (2005).

132 A. Alvarez-Herrero, H. Guerrero, and D. Levy, "High-sensitivity sensor of low relative humidity based on overlay on side-polished fibers," Ieee Sens J **4** (1), 52-56 (2004).

133 D. Flannery, S. W. James, R. P. Tatam, and G. J. Ashwell, "Fiber-optic chemical sensing with langmuir-blodgett overlay waveguides," Appl Opt **38** (36), 7370-7374 (1999).

134 N. N. Luan, R. Wang, W. H. Lv, and J. Q. Yao, "Surface plasmon resonance sensor based on D-shaped microstructured optical fiber with hollow core," Opt Express **23** (7), 8576-8582 (2015).

135 Y. L. Lo, C. H. Chuang, and Z. W. Lin, "Ultrahigh sensitivity polarimetric strain sensor based upon D-shaped optical fiber and surface plasmon resonance technology," Opt Lett **36** (13), 2489-2491 (2011).

136 A. O. Dikovska, P. A. Atanasov, A. T. Andreev, B. S. Zafirova, E. I. Karakoleva, and T. R. Stoyanchov, "ZnO thin film on side polished optical fiber for gas sensing applications," Appl Surf Sci **254** (4), 1087-1090 (2007).

137 A. Alvarez-Herrero, H. Guerrero, T. Belenguer, and D. Levy, "High-sensitivity temperature sensor based on overlay on side-polished fibers," Ieee Photonic Tech L **12** (8), 1043-1045 (2000).

138 "http://www.craictechnologies.com/products/microspectra-121-microspectrophotometer".

139 https://picclick.com/Ando-AQ6315E-Optical-Spectrum-Analyzer-OSA-351640881195.html.

140 M. Chen, K. A. Rubin, and R. W. Barton, "Compound Materials for Reversible, Phase-Change Optical-Data Storage," Appl Phys Lett **49** (9), 502-504 (1986).

141 C. N. Afonso, J. Solis, F. Catalina, and C. Kalpouzos, "Ultrafast Reversible Phase-Change in Gesb Films for Erasable Optical Storage," Appl Phys Lett **60** (25), 3123-3125 (1992).

142 H. Iwasaki, Y. Ide, M. Harigaya, Y. Kageyama, and I. Fujimura, "Completely Erasable Phase-Change Optical Disk," Jpn J Appl Phys 1 **31** (2b), 461-465 (1992).

143 N. Yamada and T. Matsunaga, "Structure of laser-crystallized Ge2Sb2+xTe5 sputtered thin films for use in optical memory," J Appl Phys **88** (12), 7020-7028 (2000).

144 Z. M. Sun, J. Zhou, and R. Ahuja, "Unique melting behavior in phase-change materials for rewritable data storage," Physical Review Letters **98** (5) (2007).

145 S. Raoux, G. W. Burr, M. J. Breitwisch, C. T. Rettner, Y. C. Chen, R. M. Shelby, M. Salinga, D. Krebs, S. H. Chen, H. L. Lung, and C. H. Lam, "Phase-change random access memory: A scalable technology," Ibm J Res Dev **52** (4-5), 465-479 (2008).

146 B. J. Eggleton, B. Luther-Davies, and K. Richardson, "Chalcogenide photonics," Nat Photonics **5** (3), 141-148 (2011).

147 M. Wuttig, H. Bhaskaran, and T. Taubner, "Phase-change materials for non-volatile photonic applications," Nat Photonics **11** (8), 465-476 (2017).

148 T. Cao, L. Zhang, R. E. Simpson, C. W. Wei, and M. J. Cryan, "Strongly tunable circular dichroism in gammadion chiral phase-change metamaterials," Opt Express **21** (23), 27841-27851 (2013).

149 Y. G. Chen, X. Li, Y. Sonnefraud, A. I. Fernandez-Dominguez, X. G. Luo, M. H. Hong, and S. A. Maier, "Engineering the Phase Front of Light with Phase-Change Material Based Planar lenses," Sci Rep-Uk **5** (2015).

150 X. J. He, S. T. Yan, G. J. Lu, Q. F. Zhang, F. M. Wu, and J. X. Jiang, "An ultra-broadband polarization-independent perfect absorber for the solar spectrum," Rsc Adv **5** (76), 61955-61959 (2015).

151 A. Tittl, A. K. U. Michel, M. Schaferling, X. H. Yin, B. Gholipour, L. Cui, M. Wuttig, T. Taubner, F. Neubrech, and H. Giessen, "A Switchable Mid-Infrared Plasmonic Perfect Absorber with Multispectral Thermal Imaging Capability," Advanced Materials **27** (31), 4597-4603 (2015).

152 Q. Wang, E. T. F. Rogers, B. Gholipour, C. M. Wang, G. H. Yuan, J. H. Teng, and N. I. Zheludev, "Optically reconfigurable metasurfaces and photonic devices based on phase change materials," Nat Photonics **10** (1), 60-U75 (2016).

153 X. H. Yin, M. Schaferling, A. K. U. Michel, A. Tittl, M. Wuttig, T. Taubner, and H. Giessen, "Active Chiral Plasmonics," Nano Lett **15** (7), 4255-4260 (2015).

154 M. Wuttig and N. Yamada, "Phase-change materials for rewriteable data storage," Nat Mater **6** (11), 824-832 (2007).

155 I. Friedrich, V. Weidenhof, W. Njoroge, P. Franz, and M. Wuttig, "Structural transformations of Ge2Sb2Te5 films studied by electrical resistance measurements," J Appl Phys **87** (9), 4130-4134 (2000).

156 S. R. Ovshinsky, "Reversible Electrical Switching Phenomena in Disordered Structures," Physical Review Letters **21** (20), 1450-+ (1968).

157 R. Kojima and N. Yamada, "Acceleration of crystallization speed by Sn addition to Ge-Sb-Te phase-change recording material," Jpn J Appl Phys 1 **40** (10), 5930-5937 (2001).

158 W. K. Njoroge, H. W. Woltgens, and M. Wuttig, "Density changes upon crystallization of Ge2Sb2.04Te4.74 films," J Vac Sci Technol A **20** (1), 230-233 (2002).

159 M. Wuttig, D. Lusebrink, D. Wamwangi, W. Welnic, M. Gillessen, and R. Dronskowski, "The role of vacancies and local distortions in the design of new phase-change materials," Nat Mater **6** (2), 122-128 (2007).

160 N. Yamada, E. Ohno, K. Nishiuchi, N. Akahira, and M. Takao, "Rapid-Phase Transitions of Gete-Sb2 Te3 Pseudobinary Amorphous Thin-Films for an Optical Disk Memory," J Appl Phys **69** (5), 2849-2856 (1991).

161 D. Piccinotti, B. Gholipour, J. Yao, K. F. Macdonald, B. E. Hayden, and N. I. Zheludev, "Compositionally controlled plasmonics in amorphous semiconductor metasurfaces," Opt Express **26** (16), 20861-20867 (2018).

162 G. P. Agrawal, *Fibre-optic Communication Systems*. (Wiley, 1992), 3rd ed.

163 R. Magnusson, M. Shokooh-Saremi, and X. Wang, "Dispersion Engineering with Leaky-Mode Resonant Photonic Lattices," Opt Express **18** (1), 108-116 (2010).

164 B. Dastmalchi, P. Tassin, T. Koschny, and C. M. Soukoulis, "Strong group-velocity dispersion compensation with phase-engineered sheet metamaterials," Phys Rev B **89** (11) (2014).

165 R. Boyd, *Nonlinear Optics*. (Academic Press, 1991), 3rd ed.